

A 10-FS MULTICOLOR SOURCE FOR ULTRAFAST  
SPECTROSCOPY AND QUANTUM  
COMMUNICATION

A Dissertation

Presented to the Faculty of the Graduate School

of Cornell University

in Partial Fulfillment of the Requirements for the Degree of

Doctor of Philosophy

by

Dylan Andrew Heberle

December 2021

© 2021 Dylan Andrew Heberle  
ALL RIGHTS RESERVED

# A 10-FS MULTICOLOR SOURCE FOR ULTRAFAST SPECTROSCOPY AND QUANTUM COMMUNICATION

Dylan Andrew Heberle, Ph.D.

Cornell University 2021

Broadband multicolor lasers are able to provide valuable information concerning ultrafast molecular dynamics through time-resolved spectroscopy. Here, I present my work developing a multicolor, 10-fs laser source through the marriage of three key technologies: (1) a high-repetition-rate, 10-fs, energetic NIR front end, (2) NIR pulse shaping, and (3) adiabatic frequency conversion. These technologies provide the means to generate femtosecond pulses in the visible, near-IR, and mid-IR with amplitude and phase control without multiple complex dispersion-management schemes, constituting a toolbox of femtosecond pulses that can be used to probe fleeting molecular dynamics. 100- $\mu$ J, 10-fs pulses are generated from the NIR front end, which are shaped and compressed with NIR 4f pulse shapers and subsequently converted to 10-fs visible (MIR) pulse using dispersion-managed adiabatic sum (difference) frequency generation. Compression of the NIR pulses has been confirmed using SHG FROG. The MIR pulses were measured using a sensitive, phase-matching-free technique called frequency-resolved optical switching. Additionally, various applications are reviewed including quantum frequency homogenization, simultaneously converting visible single photons to the telecom C-band and reducing their spectral distinguishability, and ultrafast time-resolved spectroscopy experiments planned for single-layer graphene, rhodopsin and various mutants, and DNA.

## **BIOGRAPHICAL SKETCH**

Dylan Andrew Heberle received a B.S. in Physics from Rochester Institute of Technology in 2013. He is pursuing a Ph.D. in Applied Physics from Cornell University, where he received a M.S. in 2017. His research interests include the development of new techniques and technologies through nonlinear optics and laser physics. Currently, he is working as a research fellow at Griffiss Insitute in affiliation with the Air Force Research Lab in Rome, NY.

To my wife, whose love and support has been a constant blessing and comfort.

To my family and friends, for their encouragement, guidance, and love.

## ACKNOWLEDGEMENTS

I would like to acknowledge my advisor, Dr. Jeffrey Moses, who has provided invaluable guidance throughout my research as well as the opportunity to work with cutting-edge laser systems and technologies.

Secondly, I would like to acknowledge my labmates—graduate students and post-doctoral fellow—Noah Flemens, Dr. Xiaoyue Ding, and Dr. Wei-Zung Chang who helped in developing and maintaining aspects of the NIR front end laser system. In particular, Noah Flemens designed the dispersion-managed adiabatic frequency conversion devices and greatly aided in the maintenance of the high-average-power Innoslab laser system.

Finally, I would like to acknowledge my coworkers at the Air Force Research Lab, specifically Dr. Michael Fanto, Dr. Chris Tison, and Dr. James Schneeloch who proposed the concept of frequency homogenization for quantum networking and communication.

## TABLE OF CONTENTS

Biographical Sketch . . . . .	iii
Dedication . . . . .	iv
Acknowledgements . . . . .	v
Table of Contents . . . . .	vi
List of Tables . . . . .	viii
List of Figures . . . . .	ix
<b>1 Introduction and Overview</b>	<b>1</b>
1.1 MULTICOLOR, FEMTOSECOND LASER SOURCE . . . . .	3
1.1.1 High-Repetition-Rate, 10-fs, Energetic NIR Front End . . . . .	4
1.1.2 Pulse Shaping . . . . .	6
1.1.3 Adiabatic Frequency Conversion . . . . .	7
1.2 APPLICATIONS AND FUTURE OUTLOOK . . . . .	8
1.2.1 Quantum Frequency Homogenization . . . . .	8
1.2.2 Ultrafast Molecular Dynamics . . . . .	9
<b>2 A High-Repetition-Rate, 10-femtosecond, energetic NIR Front End</b>	<b>10</b>
2.1 INTRODUCTION . . . . .	10
2.2 HIGH-AVERAGE-POWER, PICOSECOND PUMP LASER . . . . .	11
2.3 WHITE LIGHT GENERATION . . . . .	20
2.4 OPTICAL PARAMETRIC AMPLIFICATION . . . . .	25
2.4.1 Basic Principle . . . . .	26
2.4.2 OPCPA Details . . . . .	33
<b>3 Pulse Shaping</b>	<b>41</b>
3.1 BASIC PRINCIPLE . . . . .	43
3.2 PRACTICAL CONSIDERATIONS . . . . .	46
3.2.1 Mapping Optical Frequencies onto the AOM . . . . .	47
3.2.2 Acoustic Waveform Mask . . . . .	49
3.2.3 Dispersion Contributions . . . . .	50
3.3 CORRECTING ABERRATIONS IN 4F PULSE SHAPING . . . . .	55
3.3.1 Angular Dispersion and Bragg Operation . . . . .	56
3.3.2 Aberrations in Reflective 4f Designs . . . . .	59
<b>4 Multicolor, Femtosecond Source Architecture</b>	<b>66</b>
4.1 ARCHITECTURE . . . . .	66
4.2 ADIABATIC FREQUENCY CONVERSION . . . . .	69
4.3 INTRINSIC DISPERSION MANAGEMENT . . . . .	75

<b>5</b>	<b>Experiment to Demonstrate Zero Group Delay Dispersion in an Octave-Spanning Adiabatic Frequency Converter</b>	<b>81</b>
5.1	SETUP AND PHASE CALCULATION . . . . .	82
5.2	NIR PULSE MEASUREMENT . . . . .	85
5.3	MIR PULSE MEASUREMENT . . . . .	87
5.4	RESULTS AND DISCUSSION . . . . .	91
<b>6</b>	<b>Frequency Homogenization</b>	<b>95</b>
6.1	SCHMIDT DECOMPOSITION OF JSA . . . . .	97
6.2	DFG ANALOGY AND COUPLING AMPLITUDE . . . . .	99
6.3	DEVICE CALCULATIONS AND SIMULATIONS . . . . .	102
6.3.1	BBO Free-Space Device . . . . .	103
6.3.2	Rb:KTP Waveguide Device . . . . .	106
<b>7</b>	<b>Conclusions and Future Outlook</b>	<b>111</b>
7.1	SYSTEM REVIEW . . . . .	111
7.2	ULTRAFAST PUMP-PROBE SPECTROSCOPY . . . . .	112
7.3	QUANTUM COMMUNICATION . . . . .	117
<b>A</b>	<b>Phase Matching OPA Processes</b>	<b>119</b>
A.1	GROUP-VELOCITY MATCHING IN NONCOLLINEAR CON- FIGURATION . . . . .	119
<b>B</b>	<b>FROSt Retrieval Algorithm</b>	<b>121</b>
B.1	OVERVIEW . . . . .	121
	<b>Bibliography</b>	<b>125</b>

## LIST OF TABLES

2.1	Start-up procedure for daily operation of the pump laser and NIR front end system to allow for thermalization. . . . .	19
2.2	Average power noise measurements of the amplified signal from the preamplifier OPCPA stage. The percent noise is the standard deviation divided by the mean value. . . . .	38
2.3	Average power noise measurements of the amplified signal from the power OPCPA stage. The percent noise is the standard deviation divided by the mean value. . . . .	39
3.1	Typical calibration coefficients for our pulse shapers with 0.767- $\mu\text{m}$ wavelength aligned to the middle of the AOM aperture using gratings with 830-lines/mm groove density. . . . .	51
3.2	Typical dispersion values imparted by the carrier acoustic frequency evaluated at 0.767 $\mu\text{m}$ . . . . .	52
3.3	Dispersion due to the frequency-dependent optical beam paths evaluated at $\lambda = 0.767 \mu\text{m}$ . . . . .	53
3.4	The total dispersion imparted by the 4f pulse shaper evaluated at $\lambda = 0.767 \mu\text{m}$ including the contribution from the carrier acoustic wave and from the frequency-dependent optical beam paths. The calculations are shown for the positive ( $m = 1$ ) and negative ( $m = -1$ ) AOM diffraction orders. . . . .	55
3.5	Dispersion values for the acoustic phase mask required for Bragg operation evaluated at 0.767 $\mu\text{m}$ with $m = 1$ diffraction from the AOM. . . . .	58
6.1	Crystals, wavelengths, and phase-matching parameters that result in group-velocity matching between the input and pump fields and an output wavelength of 1.55 $\mu\text{m}$ . The input, output, and pump wavelengths are $\lambda_{\text{in}}$ , $\lambda_{\text{out}}$ , and $\lambda_p$ , respectively. The polarization of each field is listed as either e for extraordinary or o for ordinary, where the extraordinary polarization lies in the plane created by the wave vector and the crystal axis for uniaxial crystals or in the principal plane (PP) for biaxial crystals. For uniaxial crystals, the phase-matching angle $\theta$ defines the angle between the crystal axis and the wave vector. For biaxial crystals, the phase-matching angles $\theta$ and $\phi$ define the direction of the wave vector from the crystal Z axis to the XY plane and from the crystal X axis to the crystal Y axis, where the crystal axes are defined such that $n_x < n_y < n_z$ . The phase-matching angle $\phi$ and the principal plane are only listed for biaxial crystals. . . . .	103

## LIST OF FIGURES

1.1	Schematics of the typical ultrafast nonlinear spectroscopy architecture and our new 10-fs multicolor source architecture. . . . .	2
2.1	Ultrafast, energetic NIR front end system diagram. The NIR front end consists of three key components: (blue background) the high-average-power, picosecond pump laser, (green background) stable white light generation, and (red background) broadband, noncollinear optical parametric chirped pulse amplification stages. . . . .	11
2.2	Diagram of the high-average-power, 10-kHz, Yb:YAG Innoslab pump system built by Amphos, GmbH. The system consists of three stages: the 100-W main Innoslab amplifier, the 280-W booster Innoslab amplifier, and the high-power scraper and compressor. The main Innoslab amplifier has two exit ports, one low power and the other high power, ideal for seeding and pumping an ultrafast, energetic NIR front end. . . . .	12
2.3	Beam image of the 1030-nm, high-average-power beam at the gain crystal in the booster Innoslab amplifier taken with the <i>Double-Pass</i> Basler camera. The inset shows the horizontal (x) and vertical (y) line readouts and gaussian fits at the center-of-energy of the beam profile. . . . .	14
2.4	Beam images of the high-average-power pump system. (a) Beam image at the scraper position. Lobes above and below the central beam are visible. (b) Beam image at the position of the frequency doubling stage to generate the 515-nm pump the for OPCPA stages. The side lobes have been blocked, and the transverse beam widths and divergence have been adjusted using pairs of cylindrical lenses. . . . .	15
2.5	Beam profiles from leakage light at strategic points in the booster amplifier (IC: In-Coupling, SP: Single Pass, DP: Double Pass) using Basler cameras. (Top row) Images upon startup of the booster. (Bottom row) Images after 2 hours of thermalization. These images are used to actively monitor the alignment and performance of the booster Innoslab amplifier. . . . .	18
2.6	Power spectral density of the fiber tap in the high-power arm. The inset shows the CW breakthrough. . . . .	19

2.7	WL spectra (top panel) captured every 1 second for 2 minutes. Acquisition is set to capture 1 pulse per frame. Individual measurements are shown as light blue lines, and the average is shown as a black line. The standard deviation (bottom panel) approaches the dark counts of the spectrometer (dashed red line) over most of the WL bandwidth. In both panels, the wavelengths between the vertical dashed black lines are used to seed the OPCPA stages. . . . .	23
2.8	Filament dynamics as the WL crystal is moved through the focus, away from the focusing lens. At the closest distance to the focusing lens, where WL is first generated, the filament forms near the back of the crystal. As the crystal is moved away from the lens, the filament approaches the front of the crystal, reaches the point of closest approach with the front face, and then begins to recede toward the back face of the crystal. The point of closest approach produces the most stable WLG. . . . .	25
2.9	Energy level and wave-vector diagrams for three-wave mixing processes. . . . .	27
2.10	OPA signal gain as a function of normalized propagation distance. (left) Signal gain with perfect phase matching for different values of small-signal gain corresponding to the peak pump intensity (blue), the $1/e$ value of the pump intensity (orange), and the $1/e^2$ value of the pump intensity (green). (right) Signal gain for a small-signal gain of $\Gamma L = 10$ for different values of wave-vector mismatch. . . . .	29
2.11	Wave-vector diagram for a noncollinear OPA. The signal and idler wave vectors make angles $\alpha$ and $\Omega$ respectively with the pump wave vector. The extraordinarily polarized pump wave vector makes an angle, $\theta$ , with the crystal axis, $\bar{c}$ , known as the phase-matching angle. Introducing the noncollinear angle, $\alpha$ , between the signal and pump wave vectors allows group velocity matching. . . . .	32
2.12	Efficiency and output power of the SHG stage with (a) a 2.5-mm and (b) a 4.3-mm BBO crystal. . . . .	34
2.13	Images of the SH beam at various pump powers from a 2.5-mm and 4.3-mm BBO crystal. The percent value represents the percent of the maximum pump power available for the SHG stage. Significant beam distortion produced by conversion-back-conversion cycles is visible with the 4.3-mm BBO crystal. . . . .	35
2.14	Wave-vector mismatch and superfluorescent spectrum of the preamplifier OPCPA stage. . . . .	36
2.15	The output spectrum of the preamplifier OPCPA stage with a pump power of 2.5 W (blue) and 3.0 W (orange). . . . .	37

2.16	Beam images of the amplified signal beam profile at the BBO crystal of the preamplifier OPCPA stage. As the pump power is increased, a hole develops in the center of the beam profile indicating saturation and backconversion. . . . .	37
2.17	The output spectrum of the power amplifier OPCPA stage with a pump power of 19.2 W. . . . .	38
2.18	Beam images of the amplified signal beam profile at the BBO crystal of the power amplifier OPCPA stage. There is a slight flattening of the signal beam profile as the pump power is increased. However, the beam profile is not distorted by oversaturation of the amplifier stage. . . . .	39
3.1	4f pulse shaper schematic. An amplitude and phase mask, $H(\omega)$ , is positioned at the Fourier plane of a 4f telescope created by two lenses (L1 and L2). The telescope is positioned between two gratings (G1 and G2) such that the frequency components of an incident electric field $\tilde{E}_{in}(\omega)$ are spatially separated at the Fourier plane. The mask is applied to the incident field in the frequency domain such that $\tilde{E}_{out}(\omega) = H(\omega)\tilde{E}_{in}(\omega)$ . . . . .	42
3.2	Wave-vector diagrams for positive, first-order diffraction. (left) The electric field is incident at the Bragg angle $\theta_B$ resulting in $\Delta k = 0$ and a diffraction angle of $\theta_B$ . (right) The electric field is incident at an arbitrary angle resulting in a nonzero wave-vector mismatch. . . . .	45
3.3	4f pulse shaper using an acousto-optic modulator. The shaper is aligned such that the frequency centered on the AOM aperture is incident at the Bragg angle, $\theta_B$ . Each frequency is diffracted at an angle $\theta_d(\omega)$ dependent on the applied phase mask. . . . .	47
3.4	Dispersion imparted by the 4f shaper due to the frequency-dependent optical beam paths for (a) the positive-order diffraction and (b) the negative-order diffraction. This calculation accounts for the detuned 4f configuration and for the material dispersion of the AOM crystal. . . . .	54
3.5	Depiction of the diffracted wave vectors from (a) an acoustic waveform composed of only the carrier acoustic frequency and (b) the Bragg acoustic waveform. . . . .	57
3.6	Diffraction angles as a function of wavelength for various phase masks. . . . .	59
3.7	Schematics of (a) the cylindrical-mirror design and (b) the 1-D off-axis parabolic-mirror design [52]. . . . .	60

3.8	Beam profiles and centroids measured and simulated at the input and outputs of the pulse shapers for different frequencies [52]. (Left column) Spatial chirp measured with a CCD camera and several 40-nm bandpass filters, with center wavelengths indicated in the legend in (a). (Right column) Ray tracing simulations showing the beam centers as functions of frequency. . . . .	61
3.9	The horizontal (left) and vertical (middle) far-field divergences, $\Theta_X$ and $\Theta_Y$ respectively, and the horizontal focal position of the parabolic shaper relative to the output plane, $z_{(0,X)}$ , (right) calculated from measurements (markers with error bars) and from ray tracing (lines) as a function of wavelength for the input beam (blue), the cylindrical-design output (orange), and the parabolic-design output (green) [52]. . . . .	63
3.10	Measured horizontal (left) and vertical (right) $1/e^2$ beam radii, $w_x$ and $w_y$ , of spectral ranges from 750 nm to 900 nm as a function of distance from a 50-cm concave mirror for the cylindrical-mirror design (top row) and the parabolic-mirror design (bottom row). The small variation in focal position along the vertical dimension is due to inherent chromatic aberration in the white light source [52]. . . . .	64
4.1	Multicolor source architecture composed of our ultrafast, energetic NIR front end, NIR 4f pulse shapers, and adiabatic frequency conversion stages, each outlined by a dashed box. Shaped visible, NIR, and MIR pulses are produced through adiabatic conversion of shaped NIR pulses. The available spectral bandwidths are shown on the right side of the figure. . . . .	67
4.2	Rabi oscillations in a two-level atomic system. . . . .	72
4.3	Conversion probability of a two-level atomic system using a linear sweep rate of the detuning, $\alpha = \frac{\partial}{\partial t}\Delta$ , for various Rabi frequencies. . . . .	73
4.4	Fractional photon conversion of the aperiodically-poled KTP ASFG stage (left) and the aperiodically-poled lithium niobate ADFG stage (right) calculated from the measured fractional depletion of the NIR power spectrum [51]. . . . .	75
4.5	Group-delay constraint of the engineered dispersion calculated assuming complete propagation as either NIR (blue) or MIR (orange) in a 2-cm lithium niobate grating using Type-0 phase matching. The black, dashed lines indicate the range of group delay within which zero GDD is possible. . . . .	77
4.6	Conversion position functions resulting in constant group delay over the target MIR bandwidth. The conversion positions are restricted to 2 cm, the length of our ADFG lithium niobate grating. . . . .	77
4.7	Poling periods for Type-0 phase matching in lithium niobate. . . . .	79

5.1	Overview of dispersion-managed ADFG. A compressed multi-cycle NIR pulse at angular frequency $\omega_{\text{NIR}}$ is converted to a compressed single-cycle MIR pulse at angular frequency $\omega_{\text{MIR}}$ when combined in the dispersion-managed adiabatic frequency converter with a strong pump field at angular frequency $\omega_p$ . Both absolute bandwidth $\Delta\omega$ and pulse duration $\Delta t$ of the input field are preserved. . . . .	82
5.2	Schematic of our dispersion-managed adiabatic difference frequency generation stage used to convert a transform-limited input NIR pulse to a transform-limited output MIR pulse. Beam routes for pulse measurements are indicated. M–mirror, CM–concave mirror, DM–dichroic mirror, LF–longpass filter . . . . .	83
5.3	Home-built SHG FROG setup using a background-free, dispersion-balanced autocorrelator. The SH signal generated in a thin nonlinear crystal is measured using a visible spectrometer. RR–retroreflector, BS–beam splitter, PM–parabolic mirror . . . . .	86
5.4	Measured (right) and retrieved (left) SHG FROG traces. The retrieved trace error is 0.66%. . . . .	86
5.5	(a) Retrieved pulse intensity (blue) and phase (red) of the NIR pulse using SHG FROG. The measured FWHM pulse duration is 13.5 fs, 1.1 times the transform-limited pulse duration, 12.2 fs. (b) Retrieved spectral intensity (blue) and phase (red). . . . .	87
5.6	FROSt setup. M–mirror, CM–concave mirror, PM–parabolic mirror	88
5.7	(a) Spectrum and (b) pulse intensity of NIR pump used for FROSt. This NIR pulse is compressed using a pair of chirped mirrors instead of the 4f pulse shaper. . . . .	89
5.8	Measured (right) and retrieved (left) FROSt traces with one pass through the longpass filter. The retrieved trace error is 0.69%. . . . .	89
5.9	(a) Retrieved probe pulse intensity (blue) and probe phase (red) of the MIR pulse using FROSt with one pass through the longpass filter. The corresponding switch function is shown in orange. (b) Retrieved spectral intensity (blue) and phase (red). . . . .	90
5.10	Measured (right) and retrieved (left) FROSt traces with two passes through the longpass filter. The retrieved trace error is 0.79%. . . . .	90
5.11	(a) Retrieved pulse intensity (blue) and phase (red) of the MIR pulse using FROSt with two passes through the longpass filter. The retrieved switch function is shown in orange. (b) Retrieved spectral intensity (blue) and phase (red). . . . .	91
5.12	Calculated spectral phase $\phi_D$ imparted by the dispersion-managed adiabatic frequency conversion device. . . . .	92

5.13	Group delay imparted by the dispersion-managed adiabatic frequency conversion device. (a) Comparison with the analytic group delay from the device in Ref. [69]. (b) Zoomed plot showing the group delay from our device. . . . .	92
5.14	Calculated output MIR pulses with phase imparted by the dispersion-managed adiabatic frequency converter. The calculated transform-limited pulse (black) has a FWHM pulse duration of 13.6 fs. . . . .	93
6.1	Schmidt decomposition of an example JSA for SPDC. (a) Pictorial representation of the decomposition. The JSA is constructed from a Gaussian pump spectral amplitude and PMF. The FWHM of the functions are shown as the grey dashed and solid lines respectively. The first three orthogonal modes are shown. (b) Square of the Schmidt coefficients for the first 5 modes. The JSA has a Schmidt number $K = 1.76$ and a purity $P = 0.57$ . . . . .	99
6.2	Absolute value of the coupling amplitude $f$ calculated from the pump spectral amplitude $A_p$ and the PMF. The pump spectral intensity is assumed to have a 100-nm FWHM bandwidth centered at 2192.2 nm. All plots are normalized to the maximum values. The Schmidt number and purity of the coupling amplitude are 1.114 and 0.898 respectively. . . . .	104
6.3	Output spectra from split-step Fourier pulse propagation simulations for the 12.5-mm BBO crystal. The input center wavelength, $\lambda_{in,0}$ , is varied about the group-velocity matched wavelength. . . . .	105
6.4	Normalized spectral overlap integrals between the output spectra generated from the input pulse with a center wavelength of 0.908 $\mu\text{m}$ and the input pulses with center wavelengths, $\lambda_{in,0}$ . The solid lines show the overlap integral calculated from the coupling amplitudes, and the open circles show the overlap integral calculated from the pulse propagation simulations. The calculations are done for a 50-nm pump bandwidth (blue) and a 100-nm pump bandwidth (orange). The black dashed line marks an overlap integral of $S = 0.9$ . For the 50-nm (100-nm) pump, 14 nm (29 nm) of the overlap integrals calculated using the coupling amplitude lie above this threshold. . . . .	106
6.5	Rb:KTP waveguide profile. The waveguide has a 2- $\mu\text{m}$ width and a 5- $\mu\text{m}$ diffusion depth. The waveguide is constructed by diffusing rubidium ions into the KTP crystal along the crystal Z axis and poling the electric susceptibility along the crystal X axis. The composition of different areas and the crystal axes are labelled.	107
6.6	(a) Rb:KTP waveguide fundamental mode profile and (b) effective refractive indices. . . . .	108

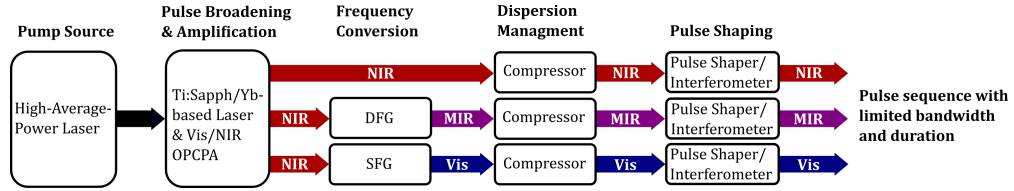
6.7	Absolute value of the coupling amplitude $f$ calculated from the pump spectral amplitude $A_p$ and the PMF. The pump spectral intensity is assumed to have a 100-nm FWHM bandwidth centered at 992 nm. All plots are normalized to the maximum values. The Schmidt number and purity of the coupling amplitude are 1.196 and 0.836 respectively. . . . .	109
6.8	Output spectra calculated from split-step Fourier pulse propagation simulations for the 2-mm Rb:KTP waveguide. The input center wavelength, $\lambda_{in,0}$ , is varied about the group-velocity matched wavelength. . . . .	109
6.9	Normalized spectral overlap integrals between the output spectra generated from the input pulse with a center wavelength of 0.605 $\mu\text{m}$ and the input pulses with center wavelengths, $\lambda_{in,0}$ . The solid lines show the overlap integral calculated from the coupling amplitudes, and the open circles show the overlap integral calculated from the pulse propagation simulations. The calculations are done for a 50-nm pump bandwidth (blue) and a 100-nm pump bandwidth (orange). The black dashed line marks an overlap integral of $S = 0.9$ . For the 50-nm (100-nm) pump, 39.1 nm (40.7 nm) of the overlap integrals calculated using the coupling amplitude lie above this threshold. . . . .	110
B.1	Diagram of FROSt retrieval algorithm. (left) Algorithm overview. (right) Experimental and product projections used in the HIO and ER schemes. . . . .	123

# CHAPTER 1

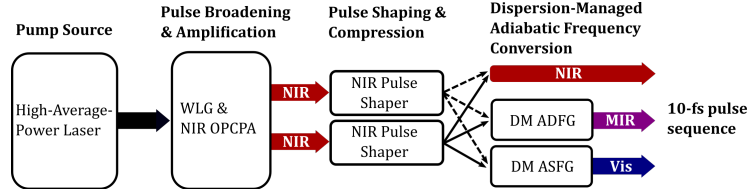
## INTRODUCTION AND OVERVIEW

Driven by the demands of ultrafast spectroscopy and intense light-matter interactions, laser pulse durations and peak intensities have reached the femtosecond and petawatt scales through the development and progress of mode-locked lasers and nonlinear optics [25,80,128]. Novel laser architectures, new materials for gain media and nonlinear interactions, and new techniques for manipulation and control of ultrashort pulses have facilitated the development of ultrafast laser laboratories that aim to investigate physical phenomena that take place in a few hundred femtoseconds or less. Typically, these laboratories rely on well-established technologies like solid-state Ti:Sapphire lasers, Yb-doped crystals, and fiber lasers as well as nonlinear frequency conversion through second- and third-order nonlinear processes to generate broad, tunable ultrafast pulses ranging from ultraviolet (UV) to terahertz [15,80].

The typical ultrafast spectroscopy source architecture is summarized in Fig. 1.1a. It begins with a high-average-power laser source that pumps a Ti:Sapphire-based or Yb-based laser combined with a visible or near-infrared (NIR) optical parametric chirped pulse amplifier (OPCPA). The resulting amplified visible or NIR pulses are converted to other frequencies using nonlinear frequency conversion such as difference frequency generation (DFG), sum frequency generation (SFG), and second harmonic generation (SHG). These conversion processes suffer from an efficiency-bandwidth tradeoff—meaning that they can either efficiently convert a modest bandwidth or convert a broader bandwidth with lower efficiency. Next, the pulses in each spectral range are compressed. This must be done independently, sometimes requiring expensive,



(a) Typical source architecture



(b) Our new 10-fs multicolor source architecture

Figure 1.1: Schematics of the typical ultrafast nonlinear spectroscopy architecture and our new 10-fs multicolor source architecture.

custom-designed dispersion management solutions. Finally, pulse shaping can be implemented, which must also be done separately for each spectral range. Overall, this architecture results in broad spectral coverage but suffers from limited conversion bandwidths resulting in longer pulse durations.

For this work, our goal was to improve the traditional source architecture to facilitate the generation of multicolor femtosecond pulses for ultrafast spectroscopy. We developed a new versatile source architecture with 10-fs pulses in the visible, near-infrared (NIR), and mid-infrared (MIR). To compare with the typical architecture, our architecture is summarized in Fig. 1.1b. Like the typical architecture, our system begins with a high-average-power laser that pumps white light generation (WLG) and a NIR OPCPA. From here, our architecture varies substantially. Instead of using conventional nonlinear frequency conversion, we use a novel frequency conversion technique known as adiabatic frequency conversion [133] with a new dispersion-managed design that we developed. This technique allows efficient one-to-one photon number conversion, imparts a linear transfer of amplitude and phase, and preserves the absolute

bandwidth of the pulse. Additionally, no dispersion is imparted by the frequency conversion device, allowing the conversion of a transform-limited NIR pulse to a transform-limited visible or MIR pulse. Due to these properties, we are able to move the pulse shaping and compression *before* frequency conversion, greatly reducing system complexity. With this design, separate compression stages, pulse shapers, and interferometers are not required for each spectral region—all of this is performed by the NIR pulse shapers, whose output can be sent to any conversion device. This architecture allows us to have a broad spectral coverage with 10-fs pulse sequences. Furthermore, to generate pulses in a new spectral region, three additional stages (frequency conversion, dispersion management, and pulse shaping) are required for the typical architecture, whereas our architecture only requires one additional stage (dispersion-managed adiabatic frequency conversion), resulting in a three-fold decrease in system complexity when adding new beamlines. Ultimately, our system boasts programmable control of broadband NIR pulses that can be efficiently converted to the visible or MIR, creating a toolbox of femtosecond pulses for measuring ultrafast dynamics or developing novel frequency conversion technologies.

## **1.1 MULTICOLOR, FEMTOSECOND LASER SOURCE**

Our multicolor, femtosecond laser source relies on the culmination of several technologies: a high-repetition-rate, 10-femtosecond, energetic NIR front end, broadband NIR pulse shaping, and adiabatic frequency conversion. The development of these technologies has been fueled by a concerted effort from the optics and spectroscopic communities to reach higher peak intensities, greater

pulse energies, and shorter pulse durations to study nonlinear light-matter interactions and to resolve the fastest molecular dynamics. In our system, I have implemented these technologies making improvements to allow robust operation and generation of femtosecond pulses in the visible, NIR, and MIR. My contributions include (1) improving the operation of our commercial, high-average-power, high-repetition-rate pump system by adding beam diagnostics and ensuring adequate beam quality through beam scraping and imaging, (2) designing, building, and optimizing the NIR front end including the white light stage and the NIR optical parametric chirped pulse amplifiers, (3) investigating dispersion and aberrations imparted by 4f pulse shapers for few-cycle pulses, (4) implementing pulse characterization systems for our NIR and MIR pulses, and (5) demonstrating dispersion-managed adiabatic frequency conversion allowing broadband and efficient frequency conversion without complex dispersion. Below, I will discuss these technologies and contributions, specifically how they are integrated into a new type of multicolor, fs-pulsed laser architecture allowing versatile pulse-shaper-assisted control of 10-fs pulses in the visible, NIR, and MIR without the need of separate complex dispersion management for each frequency range [51]. These technologies and contributions are the subjects of Chapters 2, 3, 4, and 5.

### **1.1.1 High-Repetition-Rate, 10-fs, Energetic NIR Front End**

First is the high-repetition-rate, 10-fs, energetic NIR front end. The NIR front end converts several mJ of energy at  $1.03\ \mu\text{m}$  to a few hundred  $\mu\text{J}$  in the NIR spectral region. This is an essential task as energy in the form of laser radiation is readily available through high-average-power, picosecond-pulsed lasers

that operate around  $1.03\ \mu\text{m}$ —several emergent technologies are fiber chirped pulse amplifiers [34, 35, 58, 155], thin-disk lasers [86, 97], and Innoslab amplifiers [112–114, 117]. Moreover, these systems can easily provide a secondary, low-power, sub-picosecond pulse that is trivially synchronized with the high-power pulse. This low-power, sub-picosecond pulse can be used to drive white light generation (WLG) which can be amplified by the frequency-doubled high-power pulse through optical parametric chirped pulse amplification (OPCPA). Collectively, the high-average-power, picosecond pump laser, WLG, and broadband OPCPA form our NIR front end system.

My contributions to the NIR front end include troubleshooting and improving the performance of our commercial, high-average-power, high-repetition-rate pump laser, optimizing the WLG stage, and designing, building, and optimizing the broadband, noncollinear OPCPAs. Initially, the commercial pump system was not suited for rigorous scientific applications being a first-generation product for research laboratories transitioning from a product line for industrial laser machining. Our key improvements include adding beam diagnostics to monitor system performance, installing access points for periodic adjustment of the beam alignment in the booster amplifier and compressor systems, and installing and optimizing scrapers and lenses for beam collimation and quality control. This work was a collaboration between Amphos, Noah Flemens, and myself. Furthermore, Noah and I built and optimized the WLG stage, ensuring stable operation. Finally, I designed, built, and optimized the dual-stage OPCPA system that amplifies a portion of the white light (WL) spectrum to  $\sim 100\ \mu\text{J}$  based on previous work investigating broadband amplification [18, 83, 157].

### 1.1.2 Pulse Shaping

Second is NIR pulse shaping which allows amplitude and phase control of an electric field. Throughout the past few decades, various pulse shaping techniques such as 4f pulse shaping using liquid crystal modulators, deformable mirrors, or acousto-optic modulators and acousto-optic programmable dispersive filters, have matured for visible and NIR pulses [33, 39, 40, 54]. Due to this extensive development and the unique properties of adiabatic frequency conversation, the NIR pulse shapers in our system allow versatile and precise control of a toolbox of femtosecond pulses in different spectral regions for numerous applications without the need of complex dispersion-management schemes for each spectral region.

Here, my contributions include analyzing the aberrations imparted by reflective 4f geometries in 4f pulse shaping devices [52] and investigating and understanding the total dispersion imparted by these devices. For the aberration study, we compared two common 4f geometries: one with 1-D off-axis parabolic mirrors and the other with cylindrical mirrors. For these designs, I found a tradeoff between the amount of spatial chirp and chromatic astigmatism imparted on the beam, which becomes especially significant for broadband pulses. These results determined that the cylindrical-mirror design, while more difficult to align, provides superior beam quality than the parabolic-mirror design, prompting a transition from parabolic-mirror-based 4f pulse shapers to cylindrical-mirror-based 4f pulse shapers in our lab. Regarding the operation of the pulse shapers, I calculated the dispersion imparted to the optical pulse by the carrier acoustic frequency, which cannot be controlled by the user, and determined the phase mask that would result in Bragg operation—uniform

diffraction from the acousto-optic modulator (AOM) for all optical frequencies. Finally, I investigated the dispersion resulting from nonuniform optical beam paths due to the detuned  $4f$  geometry required by  $4f$  AOM pulse shapers.

### 1.1.3 Adiabatic Frequency Conversion

The final cornerstone technology is adiabatic frequency conversion (AFC)—which is used to upconvert or downconvert the shaped NIR pulses to visible or MIR pulses. Adiabatic processes enable robust population transfer between two states via rapid adiabatic passage [81, 124]. In nonlinear optics, rapid adiabatic passage enables highly-efficient and broadband frequency conversion [7,8,133,135] which has been used to generate and amplify femtosecond, few-cycle pulses without the limitation imposed by the efficiency-bandwidth tradeoff [53,69,85,91,102,131,132,132,134].

In our architecture, we implemented dispersion-managed AFC stages that enable broadband and efficient conversion of transform-limited NIR pulses to transform-limited visible or MIR pulses. My contribution includes verifying the net-zero group-delay-dispersion operation of the stages by characterizing the pulses before and after frequency conversion. I characterized the NIR pulses using second harmonic generation frequency-resolved optical gating (SHG FROG) and the MIR pulses using a sensitive, phase-matching-free technique called frequency-resolved optical switching (FROSt) [76,77].

## 1.2 APPLICATIONS AND FUTURE OUTLOOK

The last two chapters discuss applications of our source and additional research endeavors motivated by engineered frequency conversion. First, Chapter 6 discusses frequency homogenization—reducing the spectral distinguishability of single-photon sources through frequency conversion. Lastly, Chapter 7 reviews our multicolor, 10-fs source and describes future spectroscopy experiments planned to investigate the ultrafast dynamics mediated by degeneracies in the electronic potential energy surfaces, known as conical intersections, of specific biomolecules after photoexcitation.

### 1.2.1 Quantum Frequency Homogenization

Developing a robust quantum infrastructure relies on the interconnection of mature quantum technologies such as stable, deterministic, and bright single photon sources, robust quantum memories, and low-loss and long-distance quantum networks. Such a system may rely on solid-state single photon sources such as quantum dots or color centers that operate in the visible spectral region and interact with quantum memories based on trapped ions or atomic ensembles. We have designed a device to convert visible single-photons to the telecom C-band while simultaneously decreasing the spectral distinguishability, which we call *frequency homogenization*. In Chapter 6, we describe this device as well as the specific phase-matching conditions that must be satisfied. A free-space BBO device and a waveguide Rb:KTP device have been designed and will be tested as outlined in Chapter 7.

## 1.2.2 Ultrafast Molecular Dynamics

Coherent light pulses are among the most precise tools developed for measuring and recording events in time. Circa 1878, Eadweard Muybridge used flashes of light to record events much faster than those that can be perceived by the human eye establishing the foundations of time-resolved optical science. Muybridge used multiple cameras and fast shutters to obtain fast acquisition times. With the realization of the laser in 1960, higher time resolution became possible with the much shorter durations of coherent light pulses. From there, the time resolution of transient studies has gradually increased with Ahmed Zewail earning the 1999 Nobel Prize in Chemistry for his work developing femtochemistry [156]. Laser pulse durations are now routinely sub-100 femtoseconds and are used to investigate ultrafast dynamics. For example, some molecular reactions occur in just a few hundred femtoseconds after photoexcitation.

In Chapter 7, I describe several pump-probe and 2D spectroscopy experiments that utilize our multicolor, 10-fs laser source. The first is a study of single-layer graphene, which utilizes our octave-spanning MIR pulses to capture carrier relaxation after photoexcitation as the excited carrier approaches the Dirac point. The other experiments aim to study ultrafast dynamics mediated by conical intersections, degeneracies in the electronic potential energy surfaces where the Born-Oppenheimer approximation fails. These degeneracies result in radiationless decay of the excited molecular wavepacket as it moves from the Franck-Condon state to a local minimum corresponding to the final photoproduct. We plan to study rhodopsin, channelrhodopsin mutants, and DNA to investigate the effects of local energy topography on the molecular dynamics and photoproduct yield.

CHAPTER 2  
A HIGH-REPETITION-RATE, 10-FEMTOSECOND, ENERGETIC NIR  
FRONT END

## 2.1 INTRODUCTION

Our multicolor, femtosecond laser source is built from several key technologies. First is the high-repetition-rate, femtosecond, energetic NIR front end, which consists of a high-average-power solid-state amplifier, stable white light generation (WLG), and broadband optical parametric amplification via noncollinear optical parametric chirped pulse amplification (OPCPA). The development of high-average-power and high-repetition-rate pump lasers has enabled intense, femtosecond pulse generation facilitated by their reservoir of pump energy and high peak intensities. Through highly nonlinear processes like WLG, these lasers—with sub-picosecond to a few picosecond pulse durations—can generate bandwidths large enough to support femtosecond pulses. Finally, additional pump energy can be used to amplify these bandwidths to the 100- $\mu$ J to mJ level at repetition rates in the range of 1–100 kHz using broadband amplification techniques such as noncollinear optical parametric amplification.

In this chapter, I will review the development and details of our NIR front end, with the aim of making a guide for any graduate student with a background in optics to understand, plan, and design critical aspects of a femtosecond,  $\mu$ J-level NIR front end laser. The basic principles and key technical aspects are reviewed for the three components that create our NIR front end: a high-average-power, picosecond-pulsed pump laser, a white light generation stage, and a pair of broadband optical parametric amplification stages. These

components enable the generation of  $>100\text{-}\mu\text{J}$  NIR pulses with spectral power densities that support sub-10-fs pulses. These NIR pulses are used for every application in our laboratory: terahertz generation, octave-spanning mid-infrared pulse generation, adiabatic four-wave mixing, phase-matching-free pulse characterization, and ultrafast nonlinear spectroscopy. A diagram of the high-repetition-rate, 10-fs, energetic NIR front end is shown in Fig. 2.1.

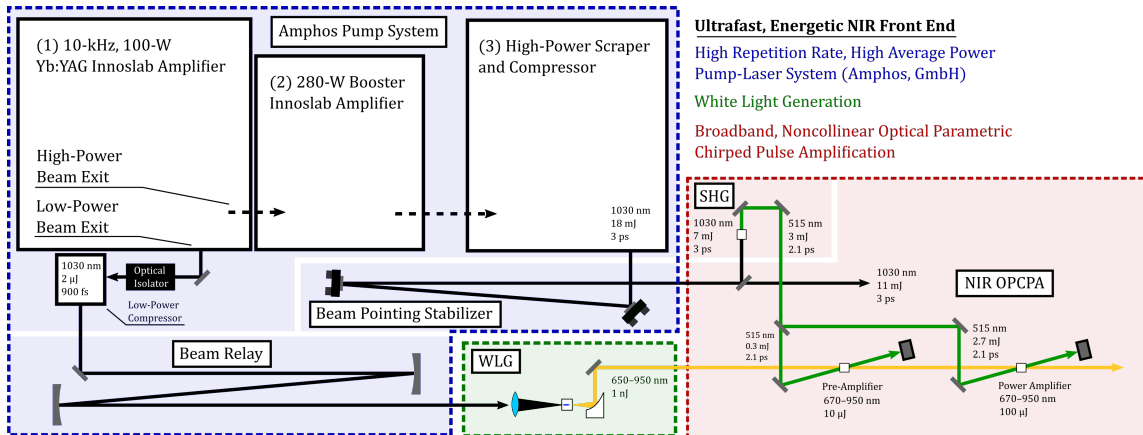


Figure 2.1: Ultrafast, energetic NIR front end system diagram. The NIR front end consists of three key components: (blue background) the high-average-power, picosecond pump laser, (green background) stable white light generation, and (red background) broadband, noncollinear optical parametric chirped pulse amplification stages.

## 2.2 HIGH-AVERAGE-POWER, PICOSECOND PUMP LASER

High-average-power and high-repetition-rate picosecond lasers often used for laser machining are promising pump sources for ultrashort, energetic NIR systems used in ultrafast spectroscopy and nonlinear frequency conversion. Throughout the process of working with our 10-kHz, 280-W pump laser system, we have learned about the short-comings of these systems—specifically those limiting scientific applications—and about the problems that can arise.

With proper engineering controls and design, these systems have proven to be a successful alternative to the Ti:sapphire systems that have pumped ultrashort NIR front end systems.

Our NIR front end is pumped by a commercial high-average-power, Yb:YAG Innoslab amplifier (Amphos, GmbH). The Innoslab amplifier design utilizes multiple passes through a slab crystal allowing high intrinsic efficiency due to the overlap between the amplified beam and the pumped volume, as well as effective heat management due to the dimensions of the slab crystal [112–114]. These characteristics allow subpicosecond pulses to be amplified to several tens of millijoules at repetition rates ranging from 10–100 kHz, providing intense energetic pulses well suited for optical parametric chirped pulse amplification.

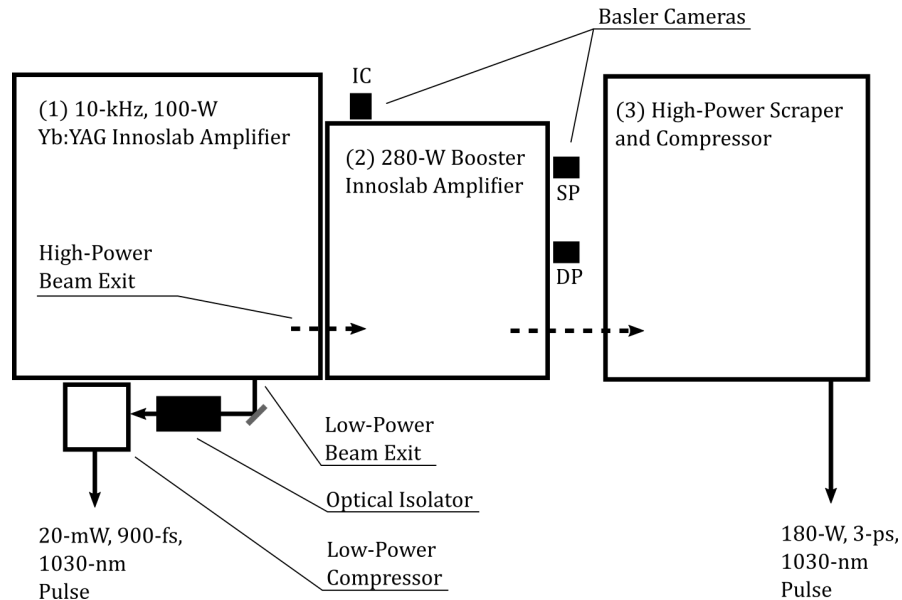


Figure 2.2: Diagram of the high-average-power, 10-kHz, Yb:YAG Innoslab pump system built by Amphos, GmbH. The system consists of three stages: the 100-W main Innoslab amplifier, the 280-W booster Innoslab amplifier, and the high-power scrapper and compressor. The main Innoslab amplifier has two exit ports, one low power and the other high power, ideal for seeding and pumping an ultrafast, energetic NIR front end.

The 10-kHz, multi-stage, Yb:YAG pump laser operating at 1030 nm is shown

in Fig. 2.2. There are three main components of the pump system: (1) a 100-W Yb:YAG laser system with a low- and high-power output, (2) a 280-W booster Innoslab amplifier, and (3) a high-power scraper and compressor. The 100-W Yb:YAG laser system consists of two arms, a low-power arm producing 2- $\mu$ J, 900-fs pulses and a high-power arm that is amplified and compressed in the subsequent components to produce 18-mJ, 3-ps pulses. The low-power arm pumps WLW in a YAG crystal while the high-power arm provides the energy reservoir necessary to pump multiple nonlinear frequency conversion stages simultaneously. Because the arms originate from the same laser oscillator, the laser pulses are guaranteed to be optically synchronized, a great asset for nonlinear frequency conversion stages and pump-probe experiments. To monitor the performance of the system and ensure robust operation, several components including additional optical isolators and Basler cameras have been added to the system.

Here, I will review some critical aspects for applications such as nonlinear frequency conversion and amplification as well as ensuring proper operation of the pump laser. These aspects include maintaining good beam and pulse quality and ensuring proper and repeatable system performance. Furthermore, I will summarize the solutions that we implemented to improve the commercial high-average-power, high-repetition-rate pump system to meet the demands of our applications.

### **Scraping and Double Pulsing**

In nonlinear frequency conversion and amplification, the quality of the pump beam profile and pulse envelope is critical to achieve efficient conversion. A

Gaussian beam profile is desirable for straightforward beam propagation, as a Gaussian beam will remain gaussian throughout propagation under the paraxial approximation [2,68]. Additionally, a Gaussian beam profile results in fairly uniform and efficient nonlinear conversion across the beam's transverse spatial dimensions due to the fewer spatial angular frequencies compared to beam profiles with sharper edges or distinct features. In the case of second-harmonic generation, a conversion efficiency of  $>70\%$  can be theoretically achieved with Gaussian beams, limited by the the wave-vector mismatch of the higher spatial angular frequencies which induce nonuniform conversion-back-conversion cycles across the transverse beam profile [11,67]. Moreover, any distortion to the pulse envelope, including satellite pulses, will reduce the overall performance of any nonlinear stage. For these high-power, energetic amplifier systems, special care must be taken to preserve good beam and pulse quality.

Due to the geometry of the gain crystal in the Innoslab amplifier, the amplified light develops side bands or lobes that cause the spatial profile to deviate from a Gaussian beam profile. A typical beam profile of the amplified light is shown in Fig. 2.3. Note, the beam at the gain crystal is highly elliptical

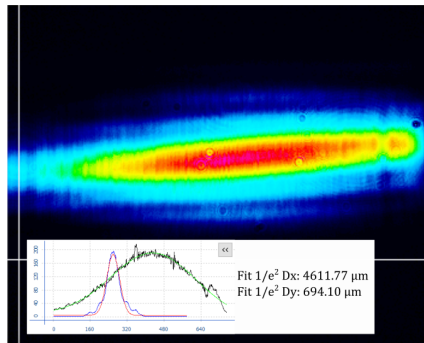


Figure 2.3: Beam image of the 1030-nm, high-average-power beam at the gain crystal in the booster Innoslab amplifier taken with the *Double-Pass* Basler camera. The inset shows the horizontal (x) and vertical (y) line readouts and gaussian fits at the center-of-energy of the beam profile.

to optimize the overlap with the gain region and to reduce the peak intensity which could result in laser-induced damage. To recover a uniform Gaussian-like beam profile and prevent clipping of these lobes on down-stream optics in our system, we implemented beam imaging and scraping in collaboration with Amphos. The transverse beam axes are independently imaged using combinations of cylindrical lenses, and the lobes are carefully blocked after the final amplification stage, well before the exit aperture of the pump laser system to allow sufficient time for the resulting diffraction pattern to propagate out of the main beam. Water-cooled ceramic razors and highly-reflective pick-off mirrors are used to block the lobes—these components are collectively called the beam scraper. The beam at the scraper position is shown in Fig. 2.4a. Ideally, the

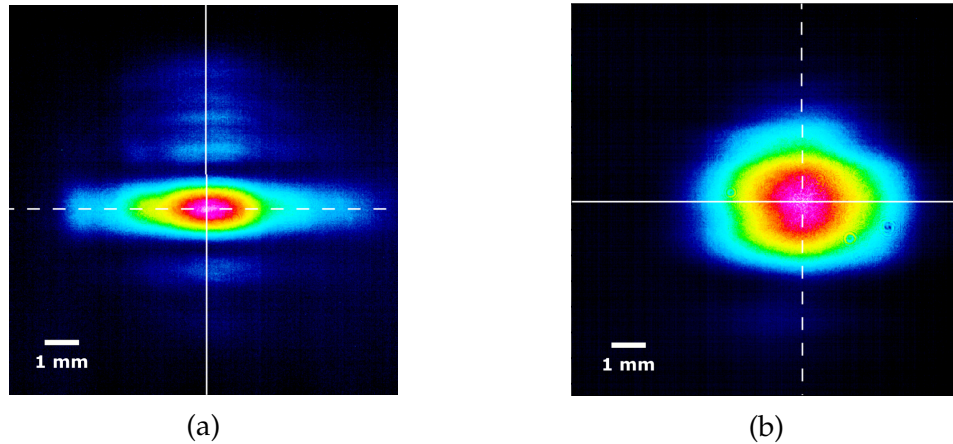


Figure 2.4: Beam images of the high-average-power pump system. (a) Beam image at the scraper position. Lobes above and below the central beam are visible. (b) Beam image at the position of the frequency doubling stage to generate the 515-nm pump the for OPCPA stages. The side lobes have been blocked, and the transverse beam widths and divergence have been adjusted using pairs of cylindrical lenses.

beam at the gain crystal is carefully imaged to the scraper position to minimize beam drift from pointing deviations during thermalization of the system. The beam profile at the first nonlinear stage is shown in Fig. 2.4b, showing the recovered Gaussian-like beam profile. Additional steps could be taken to improve

the quality, including the addition of a high-power spatial filter using a water-cooled diamond pinhole.

In addition to the beam profile, the quality of the electric field envelope must be considered. Specifically, care should be taken to ensure a clean pulse train consisting of one pulse per round trip in the laser oscillator cavity and that the pulse train does not become distorted during amplification. If driven with excessive pump power, semiconductor saturable absorber mirror (SESAM)-based laser oscillators can enter multipulse regimes with side pulses and/or double pulses. Multipulse dynamics have been studied in passively modelocked vertical external-cavity surface-emitting lasers with an intracavity SESAM [144]. If over-pumped, a side pulse forms at a quarter-round-trip time of the laser cavity away from the main pulse. This has been observed in our laser oscillator which operates at 18 MHz, corresponding to a quarter-round-trip time of 13.9 ns. If this side pulse lies within the gated time window of the AOM pulse pickers and the gain window of the amplifiers, the side pulse will persist in the amplified pulse.

### **Robust Operation**

To build a reliable femtosecond-pulsed, energetic NIR front end, the pump laser system must have robust, repeatable performance over an extended period of time. Furthermore, the system must be adequately designed to mitigate potential damage such as back reflections that could initiate CW breakthrough in the seed laser or preamplifiers. Such considerations are essential for building a robust, pump laser source that is able to meet the requirements for driving white light generation and amplifying that light in a consistent and repeatable way

throughout the course of a year.

To ensure consistent performance of our pump laser and NIR front end, the laboratory space has been carefully designed to maintain clean and consistent laboratory conditions. Water-cooled radiant panels act as a heat bath to damp out fluctuations in room temperature, and an in-line humidification unit ensures that the room humidity stays above a specified threshold during dry climate. A consistent positive air pressure is maintained in the laboratory space to prevent unconditioned air and dust from entering the room. Even with these preventative measures, the system performance varies on a seasonal basis, corresponding to the increase in humidity during the summer months. To mitigate the variation, dehumidifier units are used to prevent excessive humidity. Nevertheless, the system must be carefully monitored during the transitional months circa October and March, when there are the greatest changes in outside climate, and the humidifier and dehumidifier must be routinely checked for proper operation. If there is a significant change in the overall power or beam quality, realignment of the booster Innoslab amplifier, scraper, and compressor may be necessary.

We have developed a method to ensure day-to-day reliable operation of the laser. The booster alignment is monitored with basler cameras at three strategic positions shown in Fig. 2.2: the *In-Coupling* (IC) beam into the Innoslab amplifier crystal, the output beam after a *Single Pass* (SP) through the amplifier, and the output beam after its second pass or *Double Pass* (DP) through the amplifier. Typical beam images upon start up and after thermalization are shown in Fig. 2.5. The beam centroids and output power are monitored throughout the thermalization procedure to determine how long each stage requires to reach steady

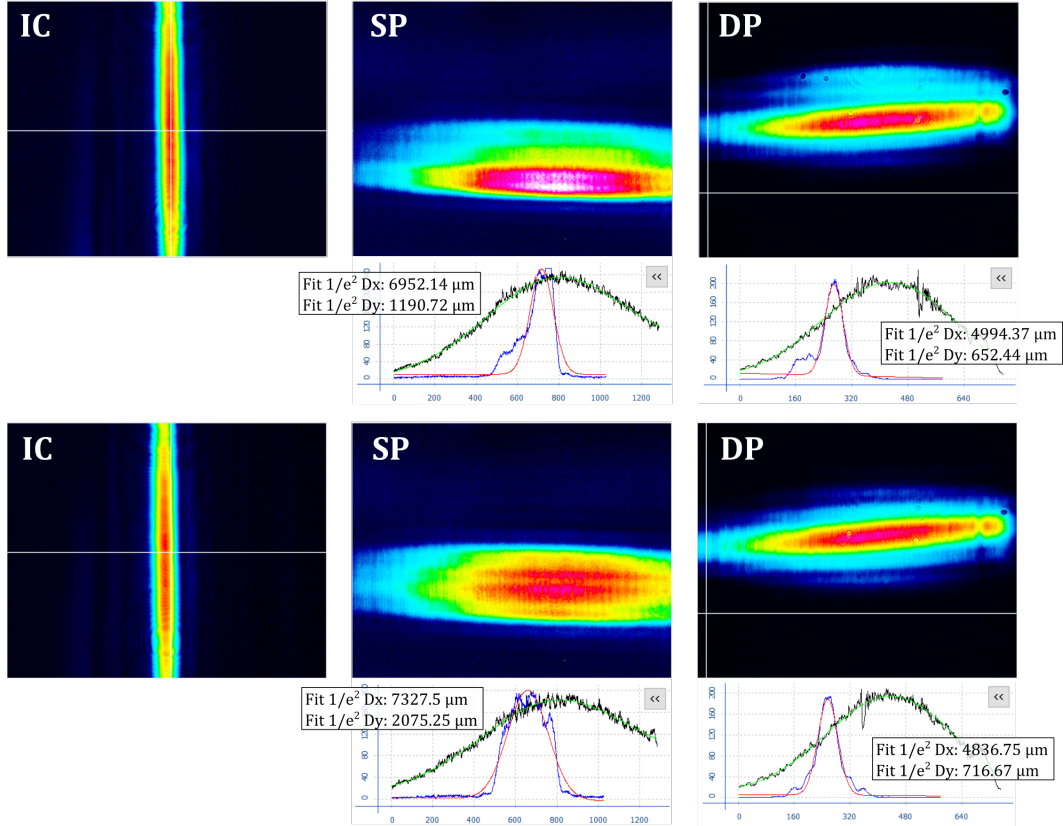


Figure 2.5: Beam profiles from leakage light at strategic points in the booster amplifier (IC: In-Coupling, SP: Single Pass, DP: Double Pass) using Basler cameras. (Top row) Images upon startup of the booster. (Bottom row) Images after 2 hours of thermalization. These images are used to actively monitor the alignment and performance of the booster Innoslab amplifier.

state and if multiple components can be thermalized simultaneously. The optimal thermalization procedure is summarized in Table 2.1. First, the 100-W Innoslab amplifier requires 30 minutes to thermalize. After which, the booster Innoslab amplifier and the high-power scraper and compressor can be started. These stages require 120 minutes to reach a state that is sufficiently stable for operating the beam pointing stabilizers. After the beam pointing stabilizers are started, the system including the second-harmonic stage and NIR OPCPA stages require approximately 120 minutes to reach a state with similar operation as the previous day due to heating of the nonlinear stages and additional beam drift

Order	Component	Time (min)
1	100-W Yb:YAG Innoslab Amplifier	30
2	280-W Booster Innoslab Amplifier	120
	High-Power Scraper and Compressor	
3	Beam-Pointing Stabilizer and NIR Front End	120
–	–	<b>270</b>

Table 2.1: Start-up procedure for daily operation of the pump laser and NIR front end system to allow for thermalization.

through the booster Innoslab amplifier, scraper, and compressor.<sup>1</sup>

Finally, the pump system must have enough optical isolation to prevent continuous-wave (CW) breakthrough and damage from back-reflected light. Additional free-space optical isolation was added to the low-power arm (shown in Fig. 2.2), and a fiber-coupled optical isolator was added in the early stages of the high-power arm. An example of CW breakthrough in the spectrum of a fiber amplifier in the high-power arm is shown in Fig. 2.6. If there is insufficient op-

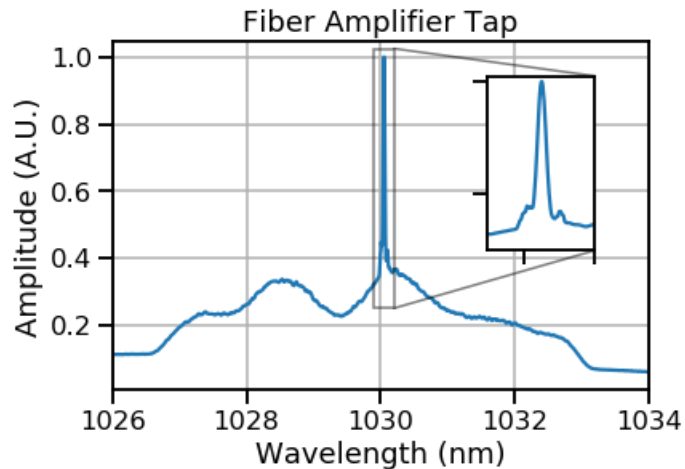


Figure 2.6: Power spectral density of the fiber tap in the high-power arm. The inset shows the CW breakthrough.

<sup>1</sup>The system is cooled by one chiller unit. As additional stages are started, they add feedback through the chiller, increasing the warm-up time. Additional chiller units could be added to uncouple the system and reduce this warm-up time.

tical isolation or a strong back reflection due to misalignment or burn damage, CW breakthrough can occur. The CW breakthrough competes with the pulse throughout the amplification stages increasing intensity noise and endangering other components in the system including the laser oscillator.

### **2.3 WHITE LIGHT GENERATION**

White light generation (WLG) is a versatile technique to generate stable, ultra-broadband laser radiation, resulting from highly-nonlinear wave mixing in wide-bandgap dielectric materials [16,32]. Physically, the process can be understood as an interplay between many optical processes including self-focusing, self-phase modulation, self-steepening, free-electron plasma formation, and chromatic dispersion which produce, sustain, and eventually disperse a column of intense laser filamentation. The self-focusing decreases the beam size in the material, increasing the peak intensity which induces free-electron plasma via multiphoton absorption and avalanche photoionization. The plasma-induced change in refractive index counteracts the effects of self-focusing preventing catastrophic collapse of the beam and forming the long filament. Due to the high optical intensities sustained in the filament, the driving pulse undergoes significant pulse broadening from self-phase modulation and other nonlinear processes. As the pulse propagates through the material, energy is absorbed by the free electrons, and chromatic dispersion stretches the pulse reducing the optical intensity, which in turn reduces the effect of self-focusing and leads to the breakup of the filament.

The catalyst of filament formation is self-focusing, a lensing effect produced

by an intensity-dependent change to the refractive index,  $n = n_0 + n_2 I$ , where  $n_0$  is the linear refractive index,  $n_2$  is the nonlinear refractive index, and  $I$  is the intensity of the optical field. Thus, the driving pulse must have a peak power above the critical power for self-focusing—the power required such that self-focusing balances diffraction—to initiate WLG. For a uniform Gaussian beam, the critical power is

$$P_{cr} = \frac{1.9\lambda^2}{4\pi n_0 n_2}, \quad (2.1)$$

where  $\lambda$  is the wavelength of the driving field [16,32]. Empirically, the ratio of peak power to critical power is used to determine the operating point and is typically 1–5 for WLG in bulk materials.

In addition to the peak power, the numerical aperture (NA) of the external optics and the pulse duration of the driving field play a significant role. If the NA is too high, the field intensity surpasses the damage threshold of the material without the pulse having enough energy to surpass the critical power for self-focusing [5, 16, 94]. If the NA is too low, multiple filaments can form as a result of divergence and refocusing of the beam [29, 79, 150]. Empirically, a NA of  $<0.05$  with a peak power several times the critical power for self-focusing is a good operating point. Furthermore, stable WLG is typically achieved with femtosecond pulses [5, 30, 94] but has recently been demonstrated with picosecond pulses [20, 44]. With femtosecond pulses, defocusing dynamics are governed by multiphoton absorption—whereas, with picosecond pulses, these dynamics are governed by avalanche ionization [16, 44]. Due to the different mechanisms, stable WLG using picosecond pulses requires longer crystal lengths [16]. Additionally, Grazuleviciute et al. [20] noted that WLG with picosecond pulses can lead to permanent material modification after consecutive laser shots when operating in the multifilament regime. However, when operating under conditions

that produce a single filament and stable WLG, no material modification is observed [20]. Thus, through appropriate choice of experimental parameters (i.e. numerical aperture, pulse energy and duration, and crystal length), stable white light (WL) can be generated using picosecond pulses from high-average-power systems. Ultimately, the optimum parameters depend on the exact experimental conditions, and a thorough review of the practical considerations for stable WLG can be found in Dubietis et al. [32].

For our WLG setup, the 900-fs, 2- $\mu$ J pulse from the low-power exit of the pump system is focused into 13-mm YAG crystal using a 75-mm focal length lens.<sup>2</sup> The  $1/e^2$  beam diameter at the lens is 2 mm corresponding to a NA of 0.013 and a confocal parameter of 3.7 mm. A typical WL spectrum is shown in the top panel of Fig. 2.7 where the sharp edge is from a 1- $\mu$ m shortpass filter used to filter the strong residual pump beam. To determine noise characteristics, the WL spectrum was recorded every 1 second over a period of 2 minutes with one pulse per measurement. The top panel in Fig. 2.7 shows the spectral measurements (light blue) and the average (black). The bottom panel in Fig. 2.7 shows the standard deviation of the data set as a function of wavelength (black). The noise across much of the spectrum is dominated by the dark noise of the detector shown as the red dashed line. Integrating the power spectrum over wavelength, the percent standard deviation of the spectral energy is 1.5%. The vertical dashed curves indicate the cut-on and cut-off wavelengths of the longpass and shortpass filters used to select the bandwidth seeding the OPCPA preamplifier.

Optimal performance of the WLG stage is achieved when a single filament

---

<sup>2</sup>Note, we use a 13-mm YAG crystal with our near-picosecond pulse. For a pulse with a few hundred femtosecond pulse duration, a shorter crystal could be used to achieve stable, single-filament WLG.

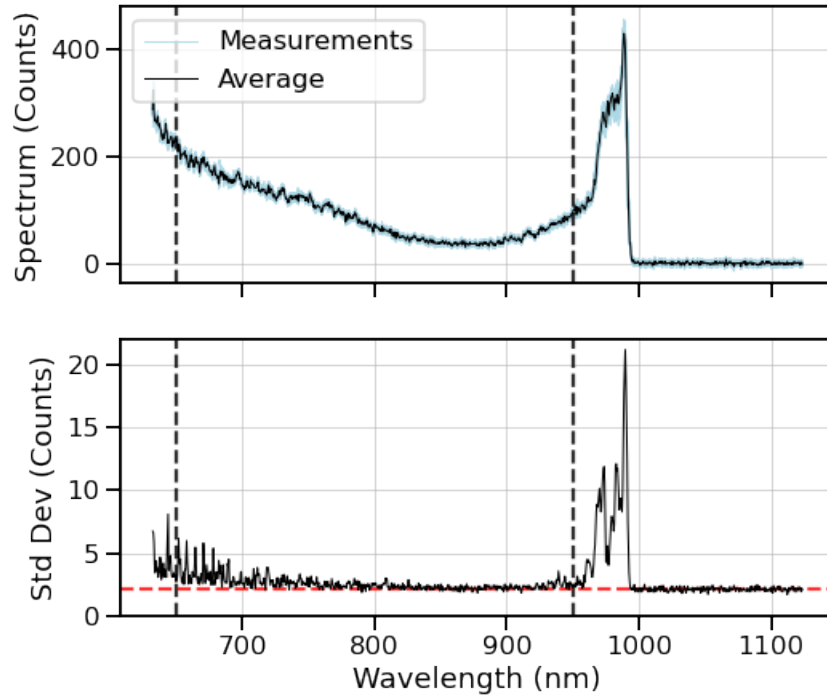


Figure 2.7: WL spectra (top panel) captured every 1 second for 2 minutes. Acquisition is set to capture 1 pulse per frame. Individual measurements are shown as light blue lines, and the average is shown as a black line. The standard deviation (bottom panel) approaches the dark counts of the spectrometer (dashed red line) over most of the WL bandwidth. In both panels, the wavelengths between the vertical dashed black lines are used to seed the OPCPA stages.

forms closest to the front face of the crystal using a transform-limited pulse [16]. If the NA or pump energy is too high, a filament will form, break apart, and reform, producing multiple filaments that have complex phase profiles. If a chirped pump pulse is used, the most stable WL spectrum will not coincide with the filament being produced closest to the front face of the crystal nor will it be as stable as the WL spectrum produced with a transform-limited pulse. The steps below indicate how the optimal white light spectrum can be achieved.

1. Measure the pulse duration of the pump pulse and adjust the grating com-

pressor until the pulse is transform-limited. If an autocorrelator measurement is not practical, steps 3–4 can be repeated iteratively adjusting the separation of the gratings in the low-power compressor until optimal stability is achieved.

2. Position the WL crystal a focal length away from the lens and unblock the pump beam.
3. If a filament is observed, scan the crystal position until it is closest to the front face as possible. The panels below in Fig. 2.8 demonstrate the filament dynamics that should be observed [16]. If no filament is observed, increase the NA or the pump power.
4. Once a filament is formed and WL is visible, a spectrometer can be used to monitor the stability. Acquisition should be set to have on average 1 pulse per acquisition window. With this setting, no fluctuations should be visible when the optimal WL performance has been achieved.
5. If the fluctuations in the power spectrum are minimized at a position where the filament is not closest to the front face of the crystal, the pulse duration should be optimized. Repeat steps 3–4 after slightly adjusting the grating separation until optimal performance is achieved when the filament is closest to the front face of the crystal.
6. If fluctuations persist, increase the pump power or the NA and repeat steps 2–5. Care should be taken to avoid a multifilament regime which can be identified by distinct rings around the main WL beam in the far-field profile [32].

Stable WLG can be achieved using the several- $\mu\text{J}$ , sub-picosecond pump pulses available from our pump system. Moreover, these pulses are readily

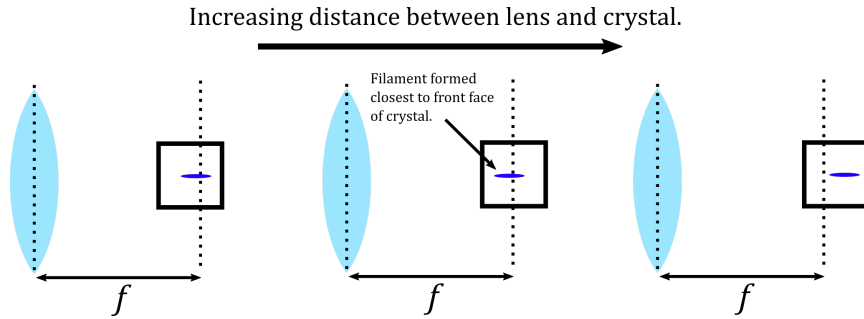


Figure 2.8: Filament dynamics as the WL crystal is moved through the focus, away from the focusing lens. At the closest distance to the focusing lens, where WL is first generated, the filament forms near the back of the crystal. As the crystal is moved away from the lens, the filament approaches the front of the crystal, reaches the point of closest approach with the front face, and then begins to recede toward the back face of the crystal. The point of closest approach produces the most stable WL.

available from pre-amplifier stages in commercial multi-stage, high-average-power, picosecond-pulsed amplifier systems, creating a valuable source of stable, broadband NIR pulses that can be readily amplified in parametric amplifiers driven by the high-average-power output of the pump system.

## 2.4 OPTICAL PARAMETRIC AMPLIFICATION

Optical parametric amplification (OPA) has become an essential part of the ultrafast optics laboratory, enabling the transfer of energy from fixed pump frequencies to tunable, broadband frequency ranges. Below, I will present an overview of OPA and the properties that make it ideal for amplification of femtosecond pulses.

## 2.4.1 Basic Principle

Parametric amplification is a three-wave mixing process that occurs in non-centrosymmetric materials as a result of the induced nonlinear polarization. To begin exploring OPA dynamics, consider the propagation of a plane wave  $\bar{E}(z, t)$  in a nonlinear medium. The field  $\bar{E}(z, t)$  induces a polarization  $\bar{P}(z, t)$  in the material, which can be expressed as the sum of two terms:  $\bar{P}(z, t) = \bar{P}^L(z, t) + \bar{P}^{NL}(z, t)$ .  $\bar{P}^L$  is the linear polarization that depends directly on  $\bar{E}$ , and  $\bar{P}^{NL}$  is the nonlinear polarization that depends on terms of  $\bar{E}^2 + O(\bar{E}^3)$ . The dynamics are described by the wave equation

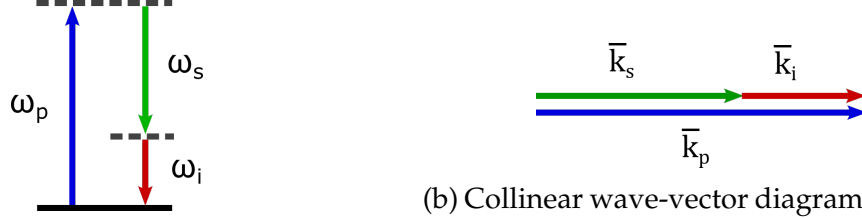
$$\frac{\partial^2 \bar{E}(z, t)}{\partial z^2} - \mu_0 \frac{\partial^2 \bar{D}(z, t)}{\partial t^2} = \mu_0 \frac{\partial^2 \bar{P}^{NL}(z, t)}{\partial t^2} \quad (2.2)$$

where  $\mu_0$  is the magnetic permeability of free space and  $\bar{D}(z, t) = \epsilon_0 \bar{E}(z, t) + \bar{P}^L(z, t)$  is the displacement field. A derivation of Eq. 2.2 from Maxwell's equations can be found in Ref. [12].

Now, consider three monochromatic fields co-propagating in the  $z$  direction with angular frequencies  $\omega_p$ ,  $\omega_s$ , and  $\omega_i$  where  $\omega_p > \omega_s > \omega_i$ . These fields are known as the pump, signal, and idler respectively. To satisfy energy conservation, the pump angular frequency must equal the sum of the signal and idler angular frequencies,  $\omega_p = \omega_i + \omega_s$ , as shown in Fig. 2.9a. Furthermore, for an efficient nonlinear process, momentum conservation must be satisfied such that the pump wave vector equals the sum of the signal and idler wave vectors,  $\bar{k}_p = \bar{k}_s + \bar{k}_i$ , as shown in Fig. 2.9b. The total field can be described by a complex field amplitude

$$\bar{E}(z, t) = \frac{1}{2} \left( \bar{A}_s(z) e^{j(\omega_s t - k_s z)} + \bar{A}_i(z) e^{j(\omega_i t - k_i z)} + \bar{A}_p(z) e^{j(\omega_p t - k_p z)} + c.c. \right) \quad (2.3)$$

where the wave vectors  $\bar{k}$  are reduced to a single scalar value along the  $z$  di-



(a) Parametric energy level diagram. The pump angular frequency  $\omega_p$  must be equal to the sum of the signal and idler angular frequencies,  $\omega_s + \omega_i$ , to satisfy energy conservation.

(b) Collinear wave-vector diagram. For efficient nonlinear conversion, momentum conservation must be satisfied such that the pump wave vector equals the sum of the signal and idler wave vectors,  $\bar{k}_p = \bar{k}_s + \bar{k}_i$ .

Figure 2.9: Energy level and wave-vector diagrams for three-wave mixing processes.

rection. As the field propagates through the material, it induces a nonlinear polarization

$$P_i^{NL} = \epsilon_0 \chi_{ijk}^{(2)} E_j E_k + O(E^3) \quad (2.4)$$

where  $\epsilon_0$  is the electric permittivity of free space,  $\chi^{(2)}$  is the second-order dielectric tensor, the subscripts  $i$ ,  $j$ , and  $k$  denote the three cartesian coordinates, and Einstein summation notation is used. For a three-wave mixing process, the terms of  $O(E^3)$  can be dropped.

Substituting Eqs. 2.3 and 2.4 into Eq. 2.2, separating the terms according to frequency, and making the slowly-varying envelope approximation yields the following set of coupled wave equations describing the evolution of the fields:

$$\frac{dA_i}{dz} = -j \frac{\omega_i d_{\text{eff}}}{n_i c_0} A_s^* A_p e^{-j\Delta k z} \quad (2.5a)$$

$$\frac{dA_s}{dz} = -j \frac{\omega_s d_{\text{eff}}}{n_s c_0} A_i^* A_p e^{-j\Delta k z} \quad (2.5b)$$

$$\frac{dA_p}{dz} = -j \frac{\omega_p d_{\text{eff}}}{n_p c_0} A_i A_s e^{j\Delta k z}, \quad (2.5c)$$

where  $n$  is the refractive index,  $c_0$  is the speed of light in vacuum,  $d_{\text{eff}}$  is the effective nonlinear coefficient, and  $\Delta k = k_p - k_s - k_i$  is the wave-vector mismatch. Equations 2.5 describe a general three-wave mixing process—whether that pro-

cess is difference frequency generation, optical parametric amplification, or another process depends on the initial conditions.

For OPA, the initial pump intensity at  $\omega_p$  is much greater than the initial signal intensity at  $\omega_s$ , allowing the transfer of energy from the pump field to the signal and idler fields. To simplify the analysis, we can assume that the pump is undepleted throughout the interaction such that  $A_p(z) = A_p$ . This approximation does not hold for efficient OPAs where the majority of the pump energy is transferred to the signal and idler fields, but the resulting solution can still provide insight into the dynamics. The initial signal amplitude is assumed to be  $A_s(0)$ , and the initial idler amplitude is assumed to be zero,  $A_i(0) = 0$ . With these initial conditions and the undepleted-pump approximation, Eqs. 2.5 can be solved:

$$I_s(L) = I_s(0) \left( 1 + \left[ \frac{\Gamma}{g} \sinh(gL) \right]^2 \right) \quad (2.6a)$$

$$I_i(L) = I_s(0) \frac{\omega_i}{\omega_s} \left( 1 + \left[ \frac{\Gamma}{g} \sinh(gL) \right]^2 \right) \quad (2.6b)$$

$$\text{with } \Gamma^2 = \frac{2d_{\text{eff}}^2 \omega_s \omega_i}{c_0^3 \epsilon_0 n_s n_i n_p} I_p$$

where  $I_j = \frac{1}{2} n_j \epsilon_0 c_0 |A_j|^2$  is the field intensity of the pump, signal, or idler ( $j = p, s, i$ ) and  $g = \sqrt{\Gamma^2 - (\Delta k/2)^2}$  is the small-signal gain.

Let us consider the behavior of these equations. The signal gain  $I_s(z)/I_s(0)$  as a function of propagation distance, normalized by a characteristic length  $L$ , is plotted in Fig. 2.10. The plot on the left shows the case of perfect phase matching,  $\Delta k = 0$ , for different values of small-signal gain. Note, when  $\Delta k = 0$ ,  $g = \sqrt{\Gamma^2 - (\Delta k/2)^2} \rightarrow \Gamma$  which is proportional to  $\sqrt{I_p}$ . The blue curve shows the evolution of the signal intensity for a small-signal gain of  $\Gamma L = 10$ . If this gain is taken to be the value experienced by the signal at the peak of the pump inten-

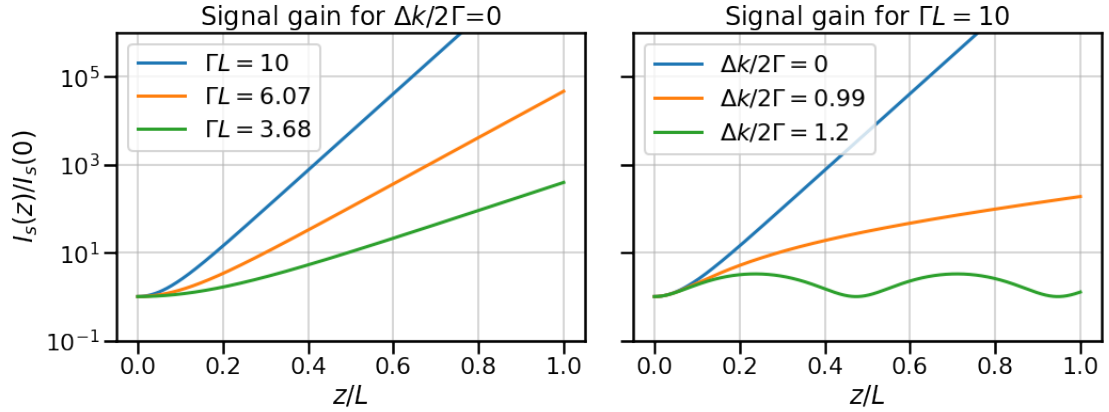


Figure 2.10: OPA signal gain as a function of normalized propagation distance. (left) Signal gain with perfect phase matching for different values of small-signal gain corresponding to the peak pump intensity (blue), the  $1/e$  value of the pump intensity (orange), and the  $1/e^2$  value of the pump intensity (green). (right) Signal gain for a small-signal gain of  $\Gamma L = 10$  for different values of wave-vector mismatch.

sity, the orange and green curves represent the gain experienced by the signal at the  $1/e$  and  $1/e^2$  points of the pump intensity. The plot on the right shows the effect of wave-vector mismatch. The blue curve in this plot corresponds to the blue curve in the left plot with  $\Gamma L = 10$  and  $\Delta k = 0$ . For increasing wave-vector mismatch, the maximum signal gain decreases, and the period of oscillation increases as the phase slip between the existing signal photons and the generated signal photons becomes faster.

Using monochromatic fields and assuming an undepleted pump, the plots in Fig. 2.10 demonstrate the upper limit of the signal gain. For light pulses, the gain is limited by the initial energy in the pump and signal fields, the spatio-temporal overlap of the beams, and parasitic processes. Moreover, the wave-vector mismatch will not be zero for all frequencies involved, which becomes especially limiting for ultrashort pulses consisting of many frequency components. Nevertheless, these plots demonstrate two important properties of OPA:

1. The gain depends strongly on the spatio-temporal pump intensity profile. For broadband pulses, the gain will have a spatio-temporal dependence.
2. The gain depends strongly on the wave-vector mismatch, which is frequency dependent. This determines the phase-matching bandwidth of the OPA.

Considering these properties, the amplification of broadband, femtosecond pulses becomes troublesome. As the gain depends strongly on the pump intensity and wave-vector mismatch, each part of the signal intensity profile and each frequency component within the signal spectrum will experience different gain dynamics resulting in nonuniform amplification—with some components undergoing conversion and backconversion cycles, limiting the overall efficiency. Fortunately, there are techniques to mitigate these effects improving OPA performance for broadband pulses.

OPA efficiency and amplification bandwidth can be optimized through the signal and pump temporal profiles and overlap. By stretching the broadband signal pulse to overlap well with the pump pulse, OPA efficiency can be improved—this is known as optical parametric chirped pulse amplification (OPCPA) and is routine for amplification of femtosecond pulses [31]. As the signal pulse duration is stretched toward the longer pump pulse duration, the efficiency increases as more energy can be extracted from the pump pulse. However, as the signal pulse duration approaches and surpasses the pump pulse duration, the amplification bandwidth decreases as portions of the signal bandwidth lie outside the effective gain region. References [110,111] have explored the tradeoff between OPA efficiency and amplification bandwidth for different signal pulse chirps with Ref. [110] determining that a signal-to-pump pulse du-

ration ratio of 0.57 optimizes the efficiency and amplification bandwidth nearly simultaneously for Gaussian signal and pump pulses. Additionally, the signal and pump pulse shapes can be engineered to improve OPA performance, known as conformal profile theory [89, 90].

To maximize the phase-matching bandwidth, let us consider the wave-vector mismatch for collinear interaction,  $\Delta k = k_p - k_s - k_i$  where  $k_j = 2\pi n(\omega_j)/c$ . The phase-matching bandwidth is maximized when  $|\partial\Delta k/\partial\omega_s|$  is minimized. Assuming a quasi-monochromatic pump field and invoking energy conservation,

$$\left| \frac{\partial\Delta k}{\partial\omega_s} \right| = \left| -\frac{\partial k_s}{\partial\omega_s} + \frac{\partial k_i}{\partial\omega_i} \right|, \quad (2.7)$$

where  $(\partial k_j/\partial\omega_j)^{-1}$  is the group velocity  $v_{g,j}$  of the wave at angular frequency  $\omega_j$ . Thus, the broadest phase-matching bandwidth is realized when the signal and idler group velocities are equal. However, this requirement depends strongly on the dispersion of the nonlinear crystal and is not always possible for the frequencies involved.

Fortunately, by introducing a noncollinear angle,  $\alpha$ , between the signal and pump, group-velocity matching (GVM) can be achieved along the direction of the signal wave vector. This technique is called noncollinear optical parametric amplification (NOPA) [18, 157]. For NOPA, the wave-vector mismatch is a vector equation  $\Delta\vec{k} = \vec{k}_p - \vec{k}_s - \vec{k}_i$ . A schematic of NOPA in a uniaxial birefringent crystal is shown in Fig. 2.11. The pump wave vector,  $\vec{k}_p$ , makes an angle  $\theta$  with the crystal axis  $\vec{c}$  and an angle  $\alpha$  with the signal wave vector,  $\vec{k}_s$ . The idler wave vector is generated at an angle  $\Omega$  with respect to the pump and an angle  $\beta$  with respect to the signal to satisfy the phase-matching condition. Note,  $\Omega$  and  $\beta$  are frequency dependent as the varying magnitudes of  $\vec{k}_s$  and  $\vec{k}_i$  yield different angles, resulting in an angularly dispersed idler. The wave-vector mismatch

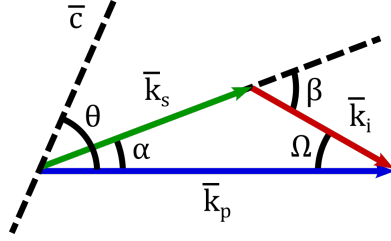


Figure 2.11: Wave-vector diagram for a noncollinear OPA. The signal and idler wave vectors make angles  $\alpha$  and  $\Omega$  respectively with the pump wave vector. The extraordinarily polarized pump wave vector makes an angle,  $\theta$ , with the crystal axis,  $\bar{c}$ , known as the phase-matching angle. Introducing the noncollinear angle,  $\alpha$ , between the signal and pump wave vectors allows group velocity matching.

can be broken into components that are parallel and perpendicular to the signal wave vector such that

$$\Delta k_{\parallel} = k_p \cos(\alpha) - k_s - k_i \cos(\beta) \quad (2.8a)$$

$$\Delta k_{\perp} = k_p \sin(\alpha) - k_i \sin(\beta). \quad (2.8b)$$

Assuming perfect phase matching,  $\Delta k_{\parallel} = 0$  and  $\Delta k_{\perp} = 0$ , and taking the derivative of Eqs. 2.8 with respect to the signal angular frequency, the relationship between the signal and idler group velocities is determined to be

$$v_{g,s} = v_{g,i} \cos(\beta). \quad (2.9)$$

Thus, the projection of the idler group velocity along the signal direction can be matched with the signal group velocity by using a noncollinear configuration, expanding the phase-matching bandwidth. The full derivation of Eq. 2.9 is included in Appendix A.1.

Enabling few-cycle pulses with terawatts of peak power, these techniques are a cornerstone to our 10-fs multicolor source architecture. Through non-collinear OPCPA, a broad, near-IR bandwidth of white light is amplified to the  $\mu\text{J}$ -level, providing a high-energy femtosecond pulse that can be readily shaped

and converted to other regions of the electromagnetic spectrum. In the following section, I will describe the OPCPA system that I designed, built, and optimized in our NIR front end system.

## 2.4.2 OPCPA Details

In our NIR front end, a two-stage OPCPA system amplifies a portion of the WL spectrum to  $>100 \mu\text{J}$ . Details about the performance of the OPCPA system are reviewed below.

### Frequency Doubling of the Pump

The OPCPA stages are pumped by frequency-doubled light from the high-power output of our pump system. 6.1-mJ of the 1030-nm pulse are used to drive second harmonic generation (SHG) in a 2.5-mm BBO crystal. The crystal length is chosen to optimize the SHG efficiency given the beam width and pulse duration of the high-power, 1030-nm beam. The conversion efficiencies of the second harmonic stage with a 2.5-mm crystal and a 4.3-mm crystal are shown in Fig. 2.12. The SHG process reaches saturation at the highest powers in the 2.5-mm crystal, where the efficiency approaches its maximum value. In the 4.3-mm crystal, conversion-back-conversion cycles are clearly visible. The SH beam profiles shown in Fig. 2.13 demonstrate the distortions that occur if a nonlinear stage is pushed beyond saturation. The percent of pump energy used of the total available for the second harmonic stage is listed in each panel. To record these beam images, the SH beam was imaged to a wide-area CCD camera (DataRay-LCM) using a 25-cm lens placed 120.5 cm from the second harmonic

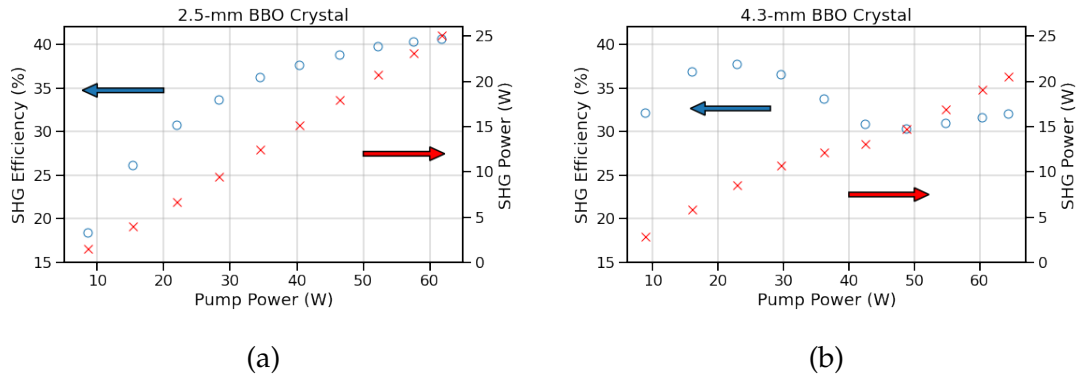


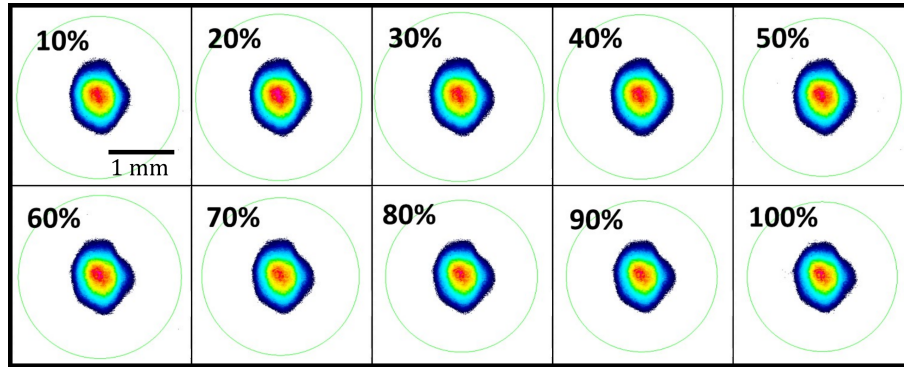
Figure 2.12: Efficiency and output power of the SHG stage with (a) a 2.5-mm and (b) a 4.3-mm BBO crystal.

stage. This produced an image 31.5 cm after the lens with a magnification of 0.26. Notably, the beam profile using the 2.5-mm crystal remains constant as the pump power is increased, unlike the beam profile using the 4.3-mm crystal which develops a hole in the center of the beam.

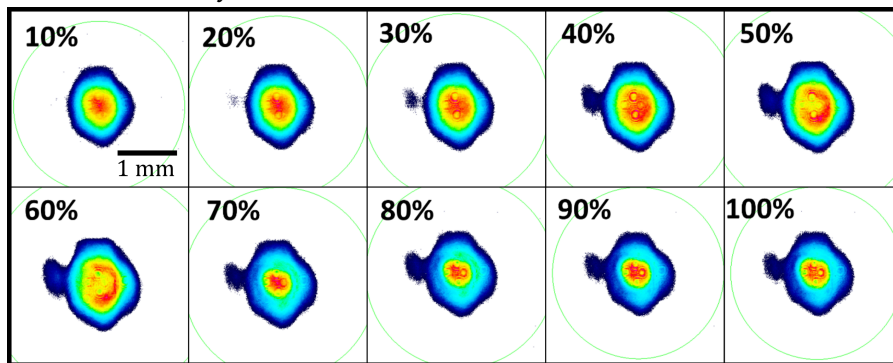
The second harmonic power produced from the SHG stage is 25 W with 41% conversion efficiency. The SHG power is split between the two OPCPA stages with 3 W going to the preamplifier and 22 W going to the power amplifier. The amount of power used for each stage is dictated by the amplifier noise characteristics and saturation dynamics.

### Preamplifier OPCPA

The preamplifier OPCPA stage is designed to maximize the amplified bandwidth with a gain of >40 dB. The stage is seeded with approximately 1 nJ of the white light that is spectrally filtered to 650–950 nm with a series of shortpass and longpass filters. The WL beam is collimated to 2.3-mm  $1/e^2$  beam diameter using a 2-inch off-axis parabolic mirror. The 3-W pump beam is reduced to



(a) SH beam profiles produced by imaging the beam at the SHG stage using a 2.5-mm BBO crystal. No conversion-back-conversion cycles are observed.



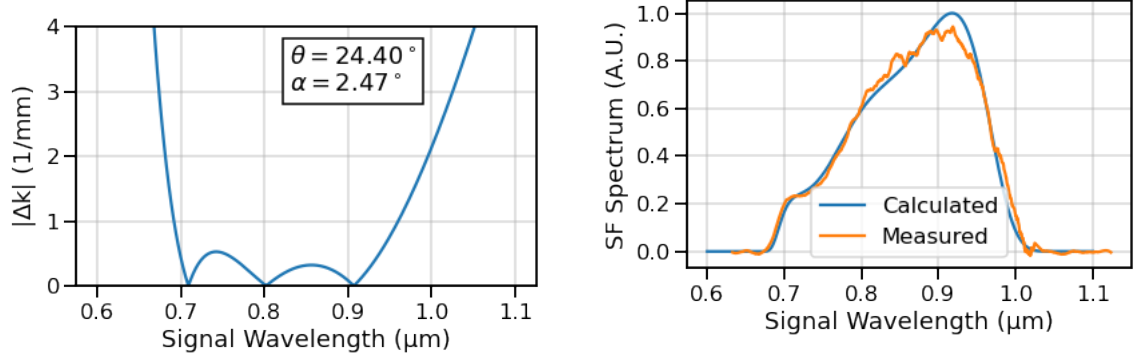
(b) SH beam profiles produced by imaging the beam at the SHG stage using a 4.3-mm BBO crystal. Conversion-back-conversion cycles are observed resulting in significant beam distortion.

Figure 2.13: Images of the SH beam at various pump powers from a 2.5-mm and 4.3-mm BBO crystal. The percent value represents the percent of the maximum pump power available for the SHG stage. Significant beam distortion produced by conversion-back-conversion cycles is visible with the 4.3-mm BBO crystal.

a 1.2-mm  $1/e^2$  beam diameter to achieve a target peak pump intensity of 14.9 GW/cm<sup>2</sup>.

The noncollinear angle,  $\alpha$ , and phase-matching angle,  $\theta$ , are chosen to minimize the wave-vector mismatch over as much WL bandwidth as possible given the central wavelengths of the pump and signal and the Sellmeier equations for the extraordinary and ordinary refractive indices of BBO [64]. The phase-matching angle and noncollinear angle for the preamplifier OPCPA stage are

chosen to be  $24.29^\circ$  and  $2.4^\circ$  respectively. The wave-vector mismatch,  $\Delta k$ , is calculated using Eqs. 2.8 and 2.9 where  $|\Delta k| = \sqrt{\Delta k_{\parallel}^2 + \Delta k_{\perp}^2}$ . Once  $|\Delta k|$  is known, the small-signal gain,  $g = \sqrt{\Gamma^2 - (\Delta k/2)^2}$ , is calculated assuming the target peak pump intensity. See Eq. 2.6 for the definition of  $\Gamma$ . Finally, the superflourescent (SF) spectrum is calculated from the small-signal gain according to  $I_{SF} = \frac{1}{4} \exp(2gz)$  [89]. The wave-vector mismatch,  $|\Delta k|$ , is shown in Fig. 2.14a, and the resulting super-flourescent spectrum using a peak pump intensity of  $14.9 \text{ GW/cm}^2$  is shown in Fig. 2.14b.



(a) Absolute value of the wave-vector mismatch of the preamplifier OPCPA stage. The phase-matching angle,  $\theta$ , is  $24.4^\circ$ , and the noncollinear angle,  $\alpha$ , is  $2.47^\circ$ .

(b) The calculated (blue) and measured (orange) superflourescent spectrum from the preamplifier OPCPA stage with 3.0 W of pump power corresponding to a peak pump intensity of  $14.9 \text{ GW/cm}^2$ .

Figure 2.14: Wave-vector mismatch and superflourescent spectrum of the preamplifier OPCPA stage.

The amplified signal spectrum is shown in Fig. 2.15 with 2.5 W and 3.0 W of pump power corresponding to  $5.8 \mu\text{J}$  and  $9.6 \mu\text{J}$  of output signal energy respectively. Ultimately, the final operating pump power and output signal energy are determined by the saturation and noise characteristics of the amplified light. To determine the saturation dynamics, the signal beam was imaged after the OPCPA crystal. The beam images are shown in Fig. 2.16. At the lowest

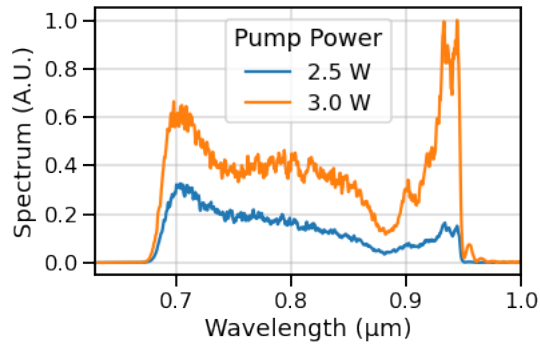


Figure 2.15: The output spectrum of the preamplifier OPCPA stage with a pump power of 2.5 W (blue) and 3.0 W (orange).

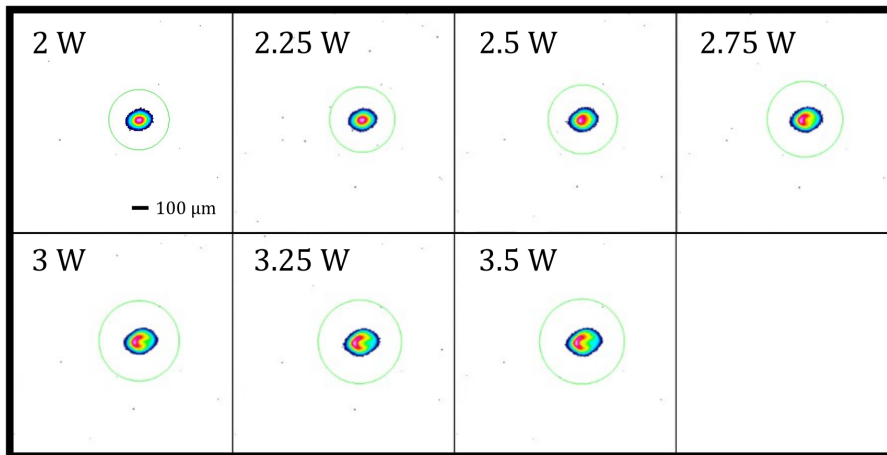


Figure 2.16: Beam images of the amplified signal beam profile at the BBO crystal of the preamplifier OPCPA stage. As the pump power is increased, a hole develops in the center of the beam profile indicating saturation and backconversion.

pump power, the signal is singly peaked. As the pump power is increased, the peak becomes flatter until a hole forms at 2.75 W. At even-greater pump powers, the hole continues to grow. Short-term noise measurements of the average power were conducted as a function of pump power, shown in Table 2.2. From these measurements, a pump power of 3.25 W is optimal with 1.27% noise in the signal average power—however, the stage is operated at 2.5 W to preserve the beam and pulse quality without oversaturating the high-gain preamplifier.

Pump Power (W)	Signal Noise (%)
2.5	3.14
3.0	1.38
3.25	1.27
3.5	1.93

Table 2.2: Average power noise measurements of the amplified signal from the preamplifier OPCPA stage. The percent noise is the standard deviation divided by the mean value.

### Power Amplifier OPCPA

After the preamplifier stage, the signal beam is further amplified in the power amplifier OPCPA, which is designed for approximately 10-dB gain. The pump power and beam size are determined by the saturation and noise dynamics of the amplifier. The phase-matching angle and noncollinear angle are similar to the values in the preamplifier stage with slight variations to accommodate specific experimental needs.

The amplified signal spectrum is shown in Fig. 2.17. This spectrum cor-

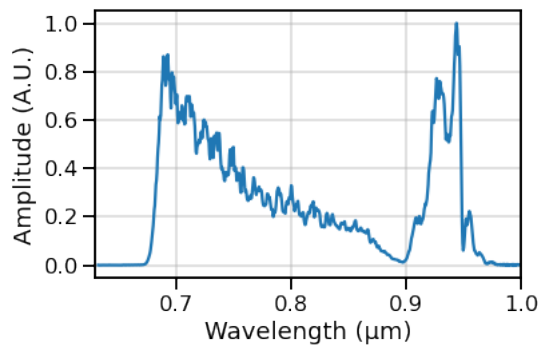


Figure 2.17: The output spectrum of the power amplifier OPCPA stage with a pump power of 19.2 W.

responds to a pump power of 19.2 W. The amplified signal beam images are shown in Fig. 2.18, confirming that there is no distortion to the amplified beam

image due to oversaturation. The corresponding noise in the average power

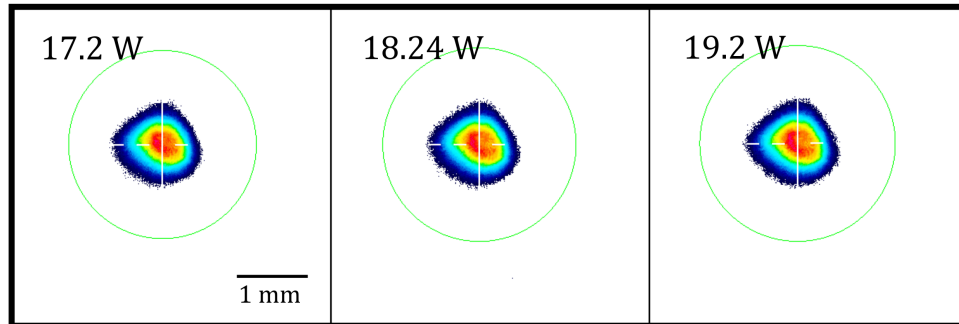


Figure 2.18: Beam images of the amplified signal beam profile at the BBO crystal of the power amplifier OPCPA stage. There is a slight flattening of the signal beam profile as the pump power is increased. However, the beam profile is not distorted by oversaturation of the amplifier stage.

of the amplified signal is shown in Table 2.3. The pump power is set to 18.24 W to minimize the noise of the amplified signal producing 130  $\mu$ J of NIR pulse energy.

Pump Power (W)	Signal Noise (%)
17.17	2.11
17.83	1.74
18.08	1.37
18.24	1.32
18.4	1.47
18.56	1.77
19.2	2.52

Table 2.3: Average power noise measurements of the amplified signal from the power OPCPA stage. The percent noise is the standard deviation divided by the mean value.

Through the marriage of high-average-power, picosecond Yb:YAG Innoslab amplifier technology, WLG, and noncollinear OPCPA, our NIR front end pro-

vides  $>100\text{-}\mu\text{J}$  pulses with a bandwidth spanning 670–950 nm with an average-power noise of 1.32%. The NIR pulse from the front end system is used in every application in our laboratory ranging from terahertz pulsed-light generation for probing phonon dynamics, seeding adiabatic four-wave mixing, and generating femtosecond MIR pulses through dispersion-managed adiabatic difference frequency generation. To facilitate these applications, the NIR pulse is split into several beam paths. Two paths are directed into 4f acousto-optic pulse shapers that enable amplitude and phase control of the NIR pulses—creating a powerful tool for ultrafast nonlinear spectroscopy when combined with adiabatic sum and difference frequency generation.

## CHAPTER 3

### PULSE SHAPING

Pulse shaping is a powerful technique that allows control of the amplitude and phase of an electric field by applying a linear, time-invariant filter. Throughout the past few decades, pulse shaping techniques with 4f configurations using liquid crystal modulators, deformable mirrors, or acousto-optic modulators and acousto-optic programmable dispersive filters have matured in the visible and NIR regions of the electromagnetic spectrum [33,39,40,54]. Recently, these techniques have begun to expand to the mid-infrared region, as demand for controllable MIR pulses increases [120–122]. Due to their extensive development in the visible and NIR and the unique properties of the proceeding adiabatic frequency conversion stages that I will discuss in Sec. 4.2, the NIR pulse shapers in our system allow versatile and precise control of a toolbox of femtosecond pulses in different spectral regions for our spectroscopic applications. In the following paragraphs, I will summarize the basic operating principles of 4f pulse shapers and review considerations for shaping ultrashort pulses. These considerations include the fixed dispersion imparted by the carrier acoustic wave and varying optical beam paths within a 4f acousto-optic pulse shaper, the angular dispersion resulting from nonuniform diffraction from a chirped acoustic wave, and the degree of spatial chirp and chromatic astigmatism inherent to reflective 4f pulse shaping geometries used for few-cycle pulses. I analyzed these characteristics for the pulse shapers in our lab, leading to a new understanding of the tradeoff between ultrafast 4f pulse shaping designs [52]. For a complete review of pulse shaping principles, there are a number of review articles and books published on the topic [88,99,147–149].

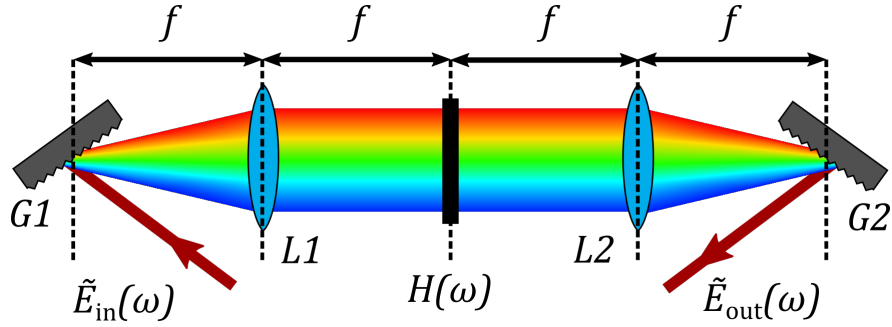


Figure 3.1: 4f pulse shaper schematic. An amplitude and phase mask,  $H(\omega)$ , is positioned at the Fourier plane of a 4f telescope created by two lenses (L1 and L2). The telescope is positioned between two gratings (G1 and G2) such that the frequency components of an incident electric field  $\tilde{E}_{in}(\omega)$  are spatially separated at the Fourier plane. The mask is applied to the incident field in the frequency domain such that  $\tilde{E}_{out}(\omega) = H(\omega)\tilde{E}_{in}(\omega)$ .

A basic pulse shaping apparatus with a pulse shaping mask at the Fourier plane of a 4f configuration is shown in Fig. 3.1. The first half of the pulse shaper is comprised of a grating positioned at the front focal plane of a lens or curved mirror. The grating angularly disperses the spectral components of the beam while the focusing optic transfers these angular components to spatial coordinates and focuses them to diffraction-limited spots at its Fourier plane. The second half of the shaper is the reverse of the first half with the focusing optic collimating each spectral component and transferring the spatial coordinates to angular components which are then recombined by the second grating. If no mask is placed at the Fourier plane, this setup is dispersion free, and the input pulse remains unaffected, neglecting aberrations from the focusing optics and the frequency response of the gratings. With a mask at the Fourier plane, the amplitude and/or phase of the input field can be controlled depending on the type of mask used. As discussed below, the use of 10-fs pulses with this technology poses new challenges.

### 3.1 BASIC PRINCIPLE

Mathematically, the shaper operation can be described as a linear filter where the output electric field is the product of a transfer function and the input electric field in the frequency domain such that

$$\tilde{E}_{\text{out}}(\omega) = H(\omega)\tilde{E}_{\text{in}}(\omega), \quad (3.1)$$

where the tilde above the electric field indicates frequency domain. The precise nature of the transfer function  $H(\omega)$  depends on the configuration of the shaper and is calculated in detail in other works [33, 88, 146, 149].

Here, I will review of the basic theory and operation of a 4f pulse shaper using an AOM [19]. The acousto-optic (AO) interaction results from the elasto-optic effect—in which a pressure wave traveling through a material creates a strain tensor  $\bar{\bar{S}}$  that changes the material properties [12, 19, 143]. Pockel's phenomenological theory states that the change in the impermeability of the material  $\Delta\bar{\bar{\eta}}$  is proportional to  $\bar{\bar{S}}$  such that

$$\Delta\eta_{ij} = p_{ijkl}S_{kl}, \quad (3.2)$$

where  $p_{ijkl}$  is the electro-optic tensor. Thus, the change in the relative electric susceptibility  $\Delta\bar{\bar{\epsilon}}$  is related to the strain tensor through its inverse relationship with the impermeability such that

$$\Delta\epsilon_{ij} = \chi_{ijkl}S_{kl}, \quad (3.3)$$

where  $\chi_{ijkl} = n_i^2 n_j^2 p_{ijkl}$  is the elasto-optic susceptibility tensor, and the displacement field in the material can be written as

$$\begin{aligned} \bar{D} &= \epsilon_0 (\bar{\bar{\epsilon}} + \Delta\bar{\bar{\epsilon}}) \bar{E} \\ &= \epsilon_0 \bar{\bar{\epsilon}} \bar{E} + \bar{P}, \end{aligned} \quad (3.4)$$

where  $\bar{P}$  is the acoustically induced polarization.<sup>1</sup> Substituting  $\bar{D}$  into the wave equation yields

$$\nabla \times \nabla \times \bar{E} + \mu_0 \frac{\partial^2}{\partial t^2} \left[ \epsilon_0 \bar{\epsilon} \bar{E} \right] = -\mu_0 \frac{\partial^2}{\partial t^2} \bar{P}, \quad (3.5)$$

which is analogous to the wave equation for three-wave mixing where  $\bar{P}$  would be the optically induced nonlinear polarization.

Thus, the AO interaction can be framed as a parametric process in which an incident electric field mixes with an acoustic wave to generate polarization waves—which, in turn, generate electric fields corresponding to the different diffraction orders. As with other parametric processes, the interaction must satisfy energy and momentum conservation. The incident electric field of angular frequency  $\omega_i$  and wave vector  $\bar{k}_i$  interacts with the acoustic wave of angular frequency  $\omega_{ac}$  and wave vector  $\bar{k}_{ac}$  producing diffracted electric fields of angular frequencies  $\omega_d = \omega_i + m\omega_{ac}$  and wave vectors  $\bar{k}_d = \bar{k}_i + m\bar{k}_{ac}$  where  $m$  is the diffraction order. For Bragg diffraction, only the first-order diffracted electric field is significant, and the total electric field can be written as

$$\bar{E}(r, t) = \frac{1}{2} \left( \bar{A}_i(z) e^{j(\omega_i t - \bar{k}_i \cdot \bar{r})} + \bar{A}_d(z) e^{j(\omega_d t - \bar{k}_d \cdot \bar{r})} + c.c. \right) \quad (3.6)$$

where  $m = 1$  and  $\bar{A}_i(z)$  and  $\bar{A}_d(z)$  are the slowly-varying amplitudes of the incident and diffracted fields respectively. The polarization can be written in terms of the strain induced by the acoustic wave via Eq. 3.3 such that

$$\bar{P}(r, t) = \epsilon_0 \bar{\chi} \bar{S}(r, t) \bar{E}(r, t). \quad (3.7)$$

The strain from the acoustic wave can be written as

$$\bar{S}(r, t) = \frac{1}{2} \left( \hat{s} S e^{j(\omega_{ac} t - \bar{k}_{ac} \cdot \bar{r})} + c.c. \right), \quad (3.8)$$

---

<sup>1</sup>This analysis assumes  $\bar{\epsilon} = \bar{\epsilon}^{(1)}$  ignoring the higher-order nonlinear dielectric tensors. Consider  $\bar{D} = \epsilon_0 \bar{\epsilon} \bar{E}$  expanded to  $\bar{D} = \epsilon_0 \left( \bar{\epsilon}^{(1)} \bar{E} + \bar{\epsilon}^{(2)} \bar{E} \bar{E} + O(\bar{E}^3) \right)$ . The acoustic wave would perturb all orders of the dielectric tensor such that the total polarization would be  $\bar{P} = \Delta \bar{\epsilon}^{(1)} \bar{E} + \bar{\epsilon}^{(2)} \bar{E} \bar{E} + \Delta \bar{\epsilon}^{(2)} \bar{E} \bar{E} + O(\bar{E}^3)$ . This may be a way to achieve tunable modulation of the nonlinear susceptibility—an interesting avenue for future research.

where  $\hat{s}$  is the unit stress tensor and  $S$  is the amplitude of the acoustic wave. Substituting Eqs. 3.6, 3.7, and 3.8 into Eq. 3.5 and using the slowly-varying envelope approximation yield the coupled wave equations for Bragg diffraction

$$\frac{dA_i}{dz} = -j \frac{\chi \omega_i^2}{4k_{i,z} c_0^2} S^* A_d e^{-j(\Delta k z)} \quad (3.9a)$$

$$\frac{dA_d}{dz} = -j \frac{\chi \omega_d^2}{4k_{d,z} c_0^2} S A_i e^{j(\Delta k z)}, \quad (3.9b)$$

where  $\Delta k = |\bar{k}_d - \bar{k}_i - \bar{k}_{ac}|$  is the magnitude of the wave-vector mismatch. The coefficients on the right-hand side of Eqs. 3.9 can be simplified after noting that  $\omega_{ac} \ll \omega_i$  and  $k_{ac} \ll k_i$  such that  $\omega_i \simeq \omega_d = \omega$  and  $k_{i,z} \simeq k_{d,z} = k_z$ . Thus, a coefficient  $\kappa = \frac{\chi \omega^2}{4k_z c_0^2} S^*$  can be defined giving

$$\frac{dA_i}{dz} = -j \kappa A_d e^{-j(\Delta k z)} \quad (3.10a)$$

$$\frac{dA_d}{dz} = -j \kappa^* A_i e^{j(\Delta k z)}. \quad (3.10b)$$

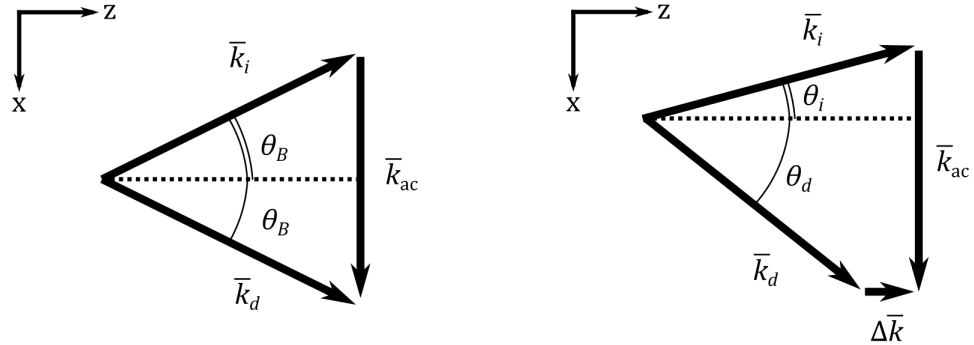


Figure 3.2: Wave-vector diagrams for positive, first-order diffraction. (left) The electric field is incident at the Bragg angle  $\theta_B$  resulting in  $\Delta k = 0$  and a diffraction angle of  $\theta_B$ . (right) The electric field is incident at an arbitrary angle resulting in a nonzero wave-vector mismatch.

If the optical wave is incident at the Bragg angle as shown in Fig. 3.2, the

wave-vector mismatch is zero, and Eqs. 3.10 can be easily solved giving

$$A_i(z) = A_i(0) \cos (|\kappa|z) \quad (3.11a)$$

$$A_d(z) = \frac{j\kappa^*}{|\kappa|} A_i(0) \sin (|\kappa|z). \quad (3.11b)$$

Note, because  $A_d(z)$  is proportional to  $\kappa^*$ , the amplitude of the diffracted wave is proportional to that of the acoustic wave. Moreover, the phase of the acoustic wave is imparted to the diffracted wave. These properties allow direct control of the amplitude and phase of the diffracted wave through the amplitude and phase of the acoustic wave.

## 3.2 PRACTICAL CONSIDERATIONS

Here, I will review aspects of using a 4f AOM pulse shaper including how to map the acoustic wave to the optical wave, imparting the desired phase function, and practical limitations of the setup. These topics are discussed in Refs. [59, 60, 88, 95, 148, 149]. I summarize important details in these works and expand the calculations to develop analytic expressions for the phase imparted by the user-defined waveform and by the carrier acoustic frequency using the empirical calibration coefficients. Additionally, I calculate the dispersion resulting from the detuned 4f geometry of the pulse shapers by modeling the frequency-dependent optical beam paths using a commercial raytracing software (FRED Optical Engineering Software, Photon Engineering, LLC). Figure 3.3 shows a schematic of a 4f AOM pulse shaper using the positive, first-order diffraction from the AOM.

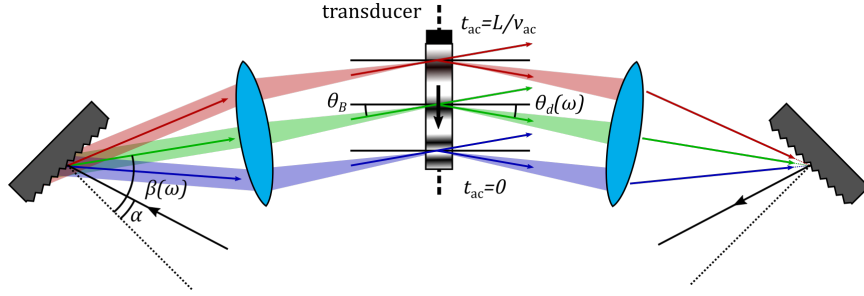


Figure 3.3: 4f pulse shaper using an acousto-optic modulator. The shaper is aligned such that the frequency centered on the AOM aperture is incident at the Bragg angle,  $\theta_B$ . Each frequency is diffracted at an angle  $\theta_d(\omega)$  dependent on the applied phase mask.

### 3.2.1 Mapping Optical Frequencies onto the AOM

First, let us review how the angular frequencies of the optical field are mapped to those of the acoustic wave. The incident optical field, shown by the black arrow on the left side of Fig. 3.3, makes an angle  $\alpha$  with the normal vector of the grating, and each angular frequency  $\omega$  is diffracted at an angle  $\beta$  according to the diffraction equation

$$\sin(\beta) + \sin(\alpha) = \frac{2\pi c_0 m}{\omega d}, \quad (3.12)$$

where  $c_0$  is the speed of light in vacuum,  $m$  is the diffraction order, and  $d$  is the groove spacing of the grating. The lens or curved mirror positioned a focal length  $f$  away, maps the spread of angles  $\Delta\beta(\omega) = \beta(\omega) - \beta(\omega_0)$  to transverse positions along the aperture of the AOM positioned at the Fourier plane. The AOM is slightly tilted such that the optical frequency centered on the AOM aperture satisfies the Bragg condition,  $\lambda_{i,0} = 2\lambda_{ac,0} \sin(\theta_B)$ , with the carrier frequency of the acoustic wave. Thus, an optical frequency is mapped to a position along the AOM according to

$$x(\omega) = L/2 - f \tan(\Delta\beta(\omega)) \cos(\theta_B), \quad (3.13)$$

where  $L$  is the length of the AOM aperture. Finally, the position,  $x$ , along the AOM must be mapped to the relative acoustic time,  $t_{ac}$ —this is the time relative to the acoustic waveform (i.e. the front of the waveform is generated by the transducer at  $t_{ac} = 0$ ). This is done using the acoustic velocity,  $v_{ac}$ , such that

$$x = v_{ac}t_{ac}. \quad (3.14)$$

By combining Eqs. 3.13 and 3.14, the optical angular frequency can be mapped to the relative acoustic time.

Empirically, the optical frequencies are mapped to the relative acoustic time using a polynomial function [59,60]. The coefficients are determined by measuring the optical spectrum of the diffracted wave using two specific amplitude-modulated acoustic waveforms. The first is a multi-peaked waveform with constant spacing in relative acoustic time, and the second is a single-peaked waveform that determines the relative offset. By measuring the two diffracted spectra, the optical frequencies can be mapped to the relative acoustic time such that

$$\omega(t_{ac}) = p_0 + p_1t_{ac} + p_2t_{ac}^2 + \mathcal{O}(t_{ac}^3). \quad (3.15)$$

Typically, this polynomial is truncated after the second-order term, which can then be solved for  $t_{ac}(\omega)$  giving

$$t_{ac}(\omega) = \frac{-p_1 \pm [p_1^2 - 4p_2(p_0 - \omega)]^{1/2}}{2p_2}, \quad (3.16)$$

where the choice of sign is determined by whether the highest or lowest optical frequency is closest to the transducer.

### 3.2.2 Acoustic Waveform Mask

Following the derivations in Refs. [59, 60, 95], the acoustic waveform mask can be mathematically described as

$$M(t_{\text{ac}}) = \mathcal{A}(t_{\text{ac}}) \sin(\omega_{\text{ac},0} t_{\text{ac}} + \Psi(t_{\text{ac}})), \quad (3.17)$$

where  $\mathcal{A}(t_{\text{ac}})$  is a variable amplitude modulation,  $\Psi(t_{\text{ac}})$  is a variable phase modulation, and  $\omega_{\text{ac},0}$  is the carrier angular frequency of the acoustic wave. This is similar to the strain function Eq. 3.8 in the derivation of the coupled amplitude equations for AO interaction—however, Eq. 3.8 is monochromatic whereas Eq. 3.17 is a chirped acoustic waveform. As discussed in Sec. 3.1, the phase of the acoustic waveform directly controls the phase  $\Phi$  imparted to the diffracted optical wave such that

$$\Phi(\omega) = m [\omega_{\text{ac},0} t_{\text{ac}}(\omega) + \psi(t_{\text{ac}}(\omega))] \quad (3.18a)$$

$$= m [\psi_0 + \psi(t_{\text{ac}}(\omega))] \quad (3.18b)$$

$$= m\Psi(t_{\text{ac}}(\omega)), \quad (3.18c)$$

where  $m$  is the diffraction order of the AOM<sup>2</sup> and  $t_{\text{ac}}$  depends explicitly on  $\omega$  through Eq. 3.16. In Eq. 3.18c, the acoustic phase terms are collected into a total acoustic phase term,  $\Psi(t_{\text{ac}}) = \psi_0 + \psi(t_{\text{ac}})$ . Equations 3.18 show that the acoustic phase modulation makes two contributions to the optical phase:  $m\psi_0$ , a constant phase corresponding to sinusoidal modulation with a single frequency component at the carrier frequency of the acoustic wave, and  $m\psi(t_{\text{ac}})$ , a user-defined variable phase.

Expanding on the derivations in Refs. [59, 60, 95], I will calculate the appropriate waveform to impart  $m\psi(t_{\text{ac}})$ . A function,  $\omega_{\text{ac}}(\omega)$ , that imparts the desired

---

<sup>2</sup>This can be +1 or -1 for Bragg diffraction depending on the specific design of the 4f AOM pulse shaper.

optical phase must be determined. Let us consider an acoustic waveform that varies in frequency along the AOM as  $\omega_{ac}(t_{ac}) = \omega_{ac,0} + \Delta\omega_{ac}(t_{ac})$ . The phase of this waveform is determined by

$$\Psi(t_{ac}) = \int_0^{t_{ac}} (\omega_{ac,0} + \Delta\omega_{ac}(\tau)) d\tau, \quad (3.19)$$

where  $\tau$  is the integration variable for the relative acoustic time. The first term in this integral is the phase from the carrier acoustic frequency,  $\psi_0 = \omega_{ac,0}t_{ac}$ . The remaining term is the variable phase  $\psi(t_{ac}) = \int_0^{t_{ac}} \Delta\omega_{ac}(\tau)d\tau$ . After performing a change of variables,  $\tau \rightarrow \omega'$ , where  $\omega'$  is the integration variable for optical angular frequency, the variable phase term becomes

$$\psi(\omega) = \int_{\omega(0)}^{\omega(t_{ac})} \Delta\omega_{ac}(\omega') \frac{d\tau}{d\omega'} d\omega'. \quad (3.20)$$

Using the first fundamental theorem of calculus, Eq. 3.20 can be rearranged as

$$\Delta\omega_{ac}(\omega) = \frac{d\psi(\omega)/d\omega}{dt_{ac}/d\omega}. \quad (3.21)$$

There are two things to note about Eq. 3.21. First,  $\Delta\omega_{ac}(\omega)$  is related to the user-defined optical phase,  $\phi(\omega) = m\psi(t_{ac}(\omega))$ , by a factor of the diffraction order,  $m$ , such that

$$\Delta\omega_{ac}(\omega) = \frac{d\phi(\omega)/d\omega}{m dt_{ac}/d\omega}. \quad (3.22)$$

Second, Eq. 3.21 can be easily related to the higher-order dispersion of the acoustic waveform by taking consecutive derivatives with respect to  $\omega$ ,

$$\frac{d^n}{d\omega^n} \psi(\omega) = \frac{d^{n-1}}{d\omega^{n-1}} \left( \Delta\omega_{ac}(\omega) \frac{dt_{ac}}{d\omega} \right). \quad (3.23)$$

### 3.2.3 Dispersion Contributions

In addition to the user-defined phase, the 4f AOM pulse shaper imparts dispersion from the constant phase sinusoid produced by the carrier acoustic

frequency and from the frequency-dependent optical beam paths (OBP). The source of the phase from the carrier acoustic frequency is the variation of optical frequency across the AOM aperture. Because  $t_{\text{ac}}(\omega)$  is a nonlinear function of  $\omega$ , the phase is nontrivial and imparts higher-order dispersion [59,60]. Following Refs. [59,60], the amount of dispersion can be calculated by taking derivatives of  $\phi_0(\omega) = m\psi_0(t_{\text{ac}})$  with respect to  $\omega$  such that

$$\frac{d^n}{d\omega^n}\phi_0 = m\frac{d^n}{d\omega^n}\psi_0(t_{\text{ac}}) = m\omega_{\text{ac},0}\frac{d^n}{d\omega^n}t_{\text{ac}}(\omega). \quad (3.24)$$

Expanding on this work, the derivatives of  $t_{\text{ac}}$  can be evaluated in terms of the calibration coefficients of the pulse shaper using Eq. 3.16,

$$\frac{d^n}{d\omega^n}t_{\text{ac}}(\omega) = \frac{(-1)^n}{\sqrt{\pi}} \left(\frac{2n-3}{2}\right)! (4p_2)^{n-1} (p_1^2 - 4p_2(p_0 - \omega))^{(2n-1)/2}, \quad (3.25)$$

giving an analytic equation to determine the dispersion imparted by the carrier acoustic frequency,

$$\frac{d^n}{d\omega^n}\phi_0(\omega) = m\omega_{\text{ac},0}\frac{(-1)^n}{\sqrt{\pi}} \left(\frac{2n-3}{2}\right)! (4p_2)^{n-1} (p_1^2 - 4p_2(p_0 - \omega))^{(2n-1)/2}. \quad (3.26)$$

To calculate the expected amount of dispersion from the carrier acoustic frequency, some typical values for the calibration coefficients of the pulse shapers in our lab are shown in Table 3.1. Using these calibration coefficients with  $m = 1$ ,  $\omega_{\text{ac},0} = 2\pi(200 \text{ MHz})$ , and  $\omega = 2\pi c_0/(0.767 \text{ }\mu\text{m})$ , Eq. 3.26 can be evaluated. The resulting terms are shown in Table 3.2.

Coefficient	Value
$p_0$	2.7357 PHz
$p_1$	-94285.5 PHz/s
$p_2$	2.58974E-6 PHz/s <sup>2</sup>

Table 3.1: Typical calibration coefficients for our pulse shapers with 0.767- $\mu\text{m}$  wavelength aligned to the middle of the AOM aperture using gratings with 830-lines/mm groove density.

Due to the tilt of the AOM in the Fourier plane of the 4f configuration and the material dispersion of the AOM, the length of the OBP as a function of optical frequency varies through the 4f AOM pulse shaper, constituting a dispersion. This can be seen in Fig. 3.3 as the OBP for the frequency at the top of the AOM is clearly longer than that at the bottom of the AOM. This dispersion depends on specific physical parameters of the pulse shaper including the grating groove density and incident angle, focal length of the focusing element (in our case, cylindrical mirrors), and the wavelength aligned to the center of the AOM aperture. Due to this intricate dependence, I used modeling to determine the variation in the OBPs for each frequency. Below, I will review the method used to determine the dispersion from the detuned 4f geometry of the AOM pulse shaper.

The 4f AOM shaper configuration using 20-cm focal length cylindrical mirrors and 830-lines/mm gratings is modelled with a commercial ray-tracing software (FRED Optical Engineering Software, Photon Engineering, LLC). The incident ray passes over the top of the first cylindrical mirror and is incident on the first grating oriented in Littrow configuration for  $0.767 \mu\text{m}$  with a slight vertical tilt to direct the beam toward the first cylindrical mirror. After the cylindrical mirror the rays are directed toward the AOM with flat turning mirrors. The de-

Dispersion Order	$n$	Value ( $\text{fs}^n$ )
GD	1	-16235.3
GDD	2	14036.1
TOD	3	-36404.3
FOD	4	157365
5OD	5	-952341

Table 3.2: Typical dispersion values imparted by the carrier acoustic frequency evaluated at  $0.767 \mu\text{m}$ .

sign is mirrored across the plane of symmetry created by the AOM. To satisfy the Bragg condition, the turning mirror must be rotated by a small amount, such that the configuration is no longer dispersion free.

To determine the dispersion from the detuned 4f configuration, the length of the OBP for each optical frequency, denoted as  $\ell(\omega)$ , is recorded in the first half of the 4f AOM pulse shaper, from the first diffraction grating to the plane-of-symmetry in the middle of the AOM. From  $\ell(\omega)$ , the phase is calculated using  $\omega/c_0\ell(\omega)$ . Then, the dispersion is calculated by taking consecutive numerical derivatives of the phase with respect to  $\omega$ . Finally, the dispersion values are doubled to account for propagation in the second half. These values are plotted in Fig. 3.4. The values evaluated at  $\lambda = 0.767 \mu\text{m}$  are shown in Table 3.3. Note, doubling the dispersion is not exact because the propagation is not symmetric, unless Bragg operation is used as discussed in Sec. 3.3.1, due to the frequency-dependent diffraction angles from the AOM. In the FRED model, the diffraction grating is oriented such that the highest optical frequency is farthest from the transducer, as required by the control software for the pulse shaper.

Dispersion Order	$n$	+1 order (fs <sup><math>n</math></sup> )	-1 order (fs <sup><math>n</math></sup> )
GDD	2	7162.2	4144.8
TOD	3	-210.3	6175.6
FOD	4	-2306.8	-19191.3
5OD	5	69500.5	123594.9

Table 3.3: Dispersion due to the frequency-dependent optical beam paths evaluated at  $\lambda = 0.767 \mu\text{m}$ .

The total dispersion contributions from the 4f AOM pulse shaper configuration are tabulated in Table 3.4.

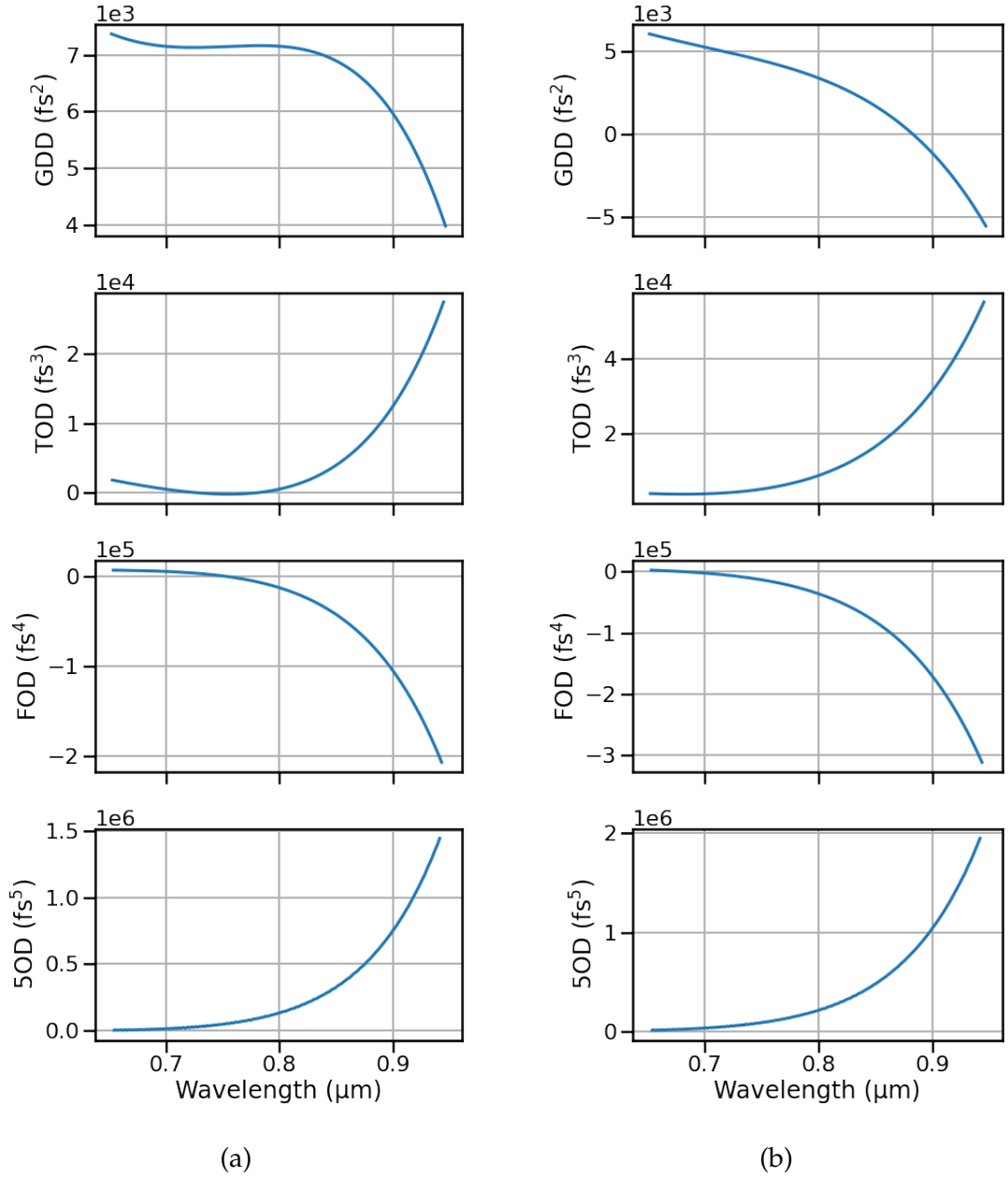


Figure 3.4: Dispersion imparted by the 4f shaper due to the frequency-dependent optical beam paths for (a) the positive-order diffraction and (b) the negative-order diffraction. This calculation accounts for the detuned 4f configuration and for the material dispersion of the AOM crystal.

$m$	Dispersion Order	$n$	Carrier Acoustic Wave (fs <sup><math>n</math></sup> )	Frequency-Dependent OBP (fs <sup><math>n</math></sup> )	Total (fs <sup><math>n</math></sup> )
+1	GDD	2	14036.1	7162.2	21198.3
	TOD	3	-36404.3	-210.3	-36614.6
	FOD	4	157365	-2306.8	155058
	5OD	5	-952341	69500.5	-882841
-1	GDD	2	-14036.1	4144.8	-9891.3
	TOD	3	36404.3	6175.6	42579.9
	FOD	4	-157365	-19191.3	-176556
	5OD	5	952341	123594.9	1.07594E6

Table 3.4: The total dispersion imparted by the 4f pulse shaper evaluated at  $\lambda = 0.767 \mu\text{m}$  including the contribution from the carrier acoustic wave and from the frequency-dependent optical beam paths. The calculations are shown for the positive ( $m = 1$ ) and negative ( $m = -1$ ) AOM diffraction orders.

### 3.3 CORRECTING ABERRATIONS IN 4F PULSE SHAPING

The optical aberrations imparted by a 4f pulse shaper—especially when using a significant fraction of an octave of bandwidth—can be severe and highly dependent on 4f geometry, causing residual angular dispersion, frequency-dependent or chromatic astigmatism, and spatial chirp that can greatly impede applications. In the following section, I discuss the angular dispersion imparted by a 4f AOM pulse shaper as well as techniques to mitigate it [60, 95]. I also discuss aberrations from reflective designs of the 4f configuration, which are employed with broadband pulses to avoid chromatic aberration from lenses. In Ref. [52], we investigated these aberrations which depend on the specific orientation of the gratings and the reflective optics used, finding a tradeoff between spatial chirp and chromatic astigmatism imparted to the beam for designs using cylindrical mirrors and 1-D off-axis parabolic mirrors.

### 3.3.1 Angular Dispersion and Bragg Operation

For efficient diffraction from an AOM, the incident electric field must satisfy momentum conservation as shown in the left panel of Fig. 3.2. When momentum conservation is fulfilled, the incident angle is equal to the diffraction angle, and the diffraction equation for light from an acoustic wave of wavelength  $\lambda_{ac}$  becomes

$$2 \sin(\theta_B) = \frac{m\lambda}{\lambda_{ac}}, \quad (3.27)$$

where  $\theta_B$  is the Bragg angle [12]. In practice, the pulse shaper is aligned such that this condition is satisfied by the wavelength centered on the AOM aperture,  $\lambda_0$ , with the acoustic carrier wavelength,  $\lambda_{ac,0}$ . Thus, the incident angle is  $\theta_i = \theta_B(\lambda_0, \lambda_{ac,0}) = \sin^{-1}\left(\frac{m\lambda_0}{2\lambda_{ac,0}}\right)$ . All other wavelegnthns have the same incident angle but do not satisfy momentum conservation with the carrier acoustic wave nor are guarenteed to satisfy mometum conservation with the acoustic frequency required to impart the desired phase profile. The diffraction from an acoustic waveform consisting of only the carrier acoustic frequency is shown in Fig. 3.5a, where  $\theta_d(\lambda) = \sin^{-1}\left[\frac{m\lambda}{\lambda_{ac,0}} - \sin(\theta_B(\lambda_0, \lambda_{ac,0}))\right]$ .

However, an acoustic waveform can be devised such that momentum conservation is satisfied for every optical frequency [60,95]<sup>3</sup>, as shown in Fig. 3.5b. This is called the Bragg acoustic waveform. In the following section, I reproduce the derivations in Refs. [60,95] while accounting for the refraction at the interfaces of the AOM crystal, resulting in a correction to the final equation for the Bragg acoustic waveform. Consider the diffraction of the incident electric field from the AOM. First, all frequencies are incident on the AOM interface at

---

<sup>3</sup>These references calculate the acoustic waveform,  $\omega_{ac}(\omega)$ , required for Bragg operation but include extra refractive index terms as a result of neglecting refraction at the interfaces of the AOM.

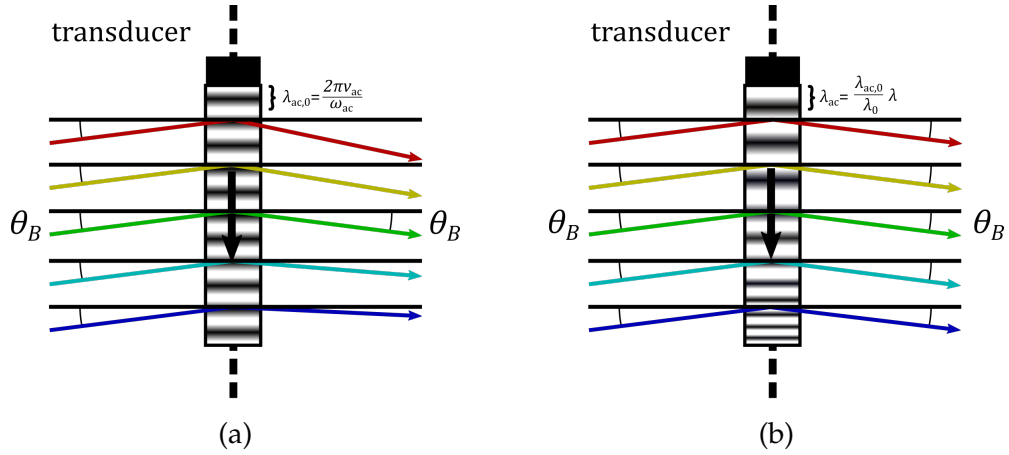


Figure 3.5: Depiction of the diffracted wave vectors from (a) an acoustic waveform composed of only the carrier acoustic frequency and (b) the Bragg acoustic waveform.

the same angle,  $\theta_1$ , and refract according to Snell's Law,

$$\sin(\theta_1) = n' \sin(\theta'_1), \quad (3.28)$$

where  $n'$  is the refractive index of the AOM material and  $\theta'_1$  is the refraction angle. Then, the beams are diffracted according to the diffraction equation

$$\sin(\theta'_1) + \sin(\theta'_2) = \frac{m\lambda}{\lambda_{ac}n'}. \quad (3.29)$$

After which, they refract again as they exit the AOM,

$$n' \sin(\theta'_2) = \sin(\theta_2). \quad (3.30)$$

Combining Eqs. 3.28, 3.29, and 3.30 and enforcing that all optical frequencies satisfy the Bragg condition,  $\theta'_1 = \theta'_2$ , yields

$$\sin(\theta_2) = \frac{m\lambda}{2\lambda_{ac}}. \quad (3.31)$$

From Eq. 3.31, the requirement for Bragg operation is clear:  $\lambda$  must be directly proportional to  $\lambda_{ac}$  such that  $\lambda/\lambda_{ac}$  is constant. This constant is  $\lambda_0/\lambda_{ac,0}$  as the wavelength centered on the AOM is aligned to meet the Bragg condition with

the carrier acoustic frequency. Thus,

$$\lambda_{ac} = \frac{\lambda_0}{\lambda_{ac,0}} \lambda \quad (3.32)$$

is the condition that must be satisfied for all wavelengths to exit the AOM without angular dispersion.

The phase mask that satisfies Eq. 3.32 can be calculated by solving the integral in Eq. 3.20 after casting Eq. 3.32 in terms of angular frequencies and solving for a change about the carrier acoustic frequency,

$$\omega_{ac} = \frac{\omega_{ac,0}}{\omega_0} \omega \quad (3.33a)$$

$$\omega_{ac,0} + \Delta\omega_{ac} = \frac{\omega_{ac,0}}{\omega_0} \omega \quad (3.33b)$$

$$\Delta\omega_{ac} = \omega_{ac,0} \left( \frac{\omega}{\omega_0} - 1 \right). \quad (3.33c)$$

The resulting orders of dispersion for  $m = 1$  are shown in Table 3.5.

Dispersion Order	$n$	Value (fs <sup><math>n</math></sup> )
GD	1	0
GDD	2	-6610.8
TOD	3	11430.6
FOD	4	-44470.2
5OD	5	256309.0

Table 3.5: Dispersion values for the acoustic phase mask required for Bragg operation evaluated at 0.767  $\mu\text{m}$  with  $m = 1$  diffraction from the AOM.

Diffraction using various phase masks is shown in Fig. 3.6. The Bragg mask results in uniform diffraction from the AOM at the Bragg angle of the centered wavelength while other masks impart an angular dispersion at the Fourier plane, leading to spatial chirp and residual angular dispersion at the output of the pulse shaper. In order to have efficient, near-uniform diffraction for all opti-

cal frequencies from the AOM, the pulse shaper should be operated close to the Bragg mask.

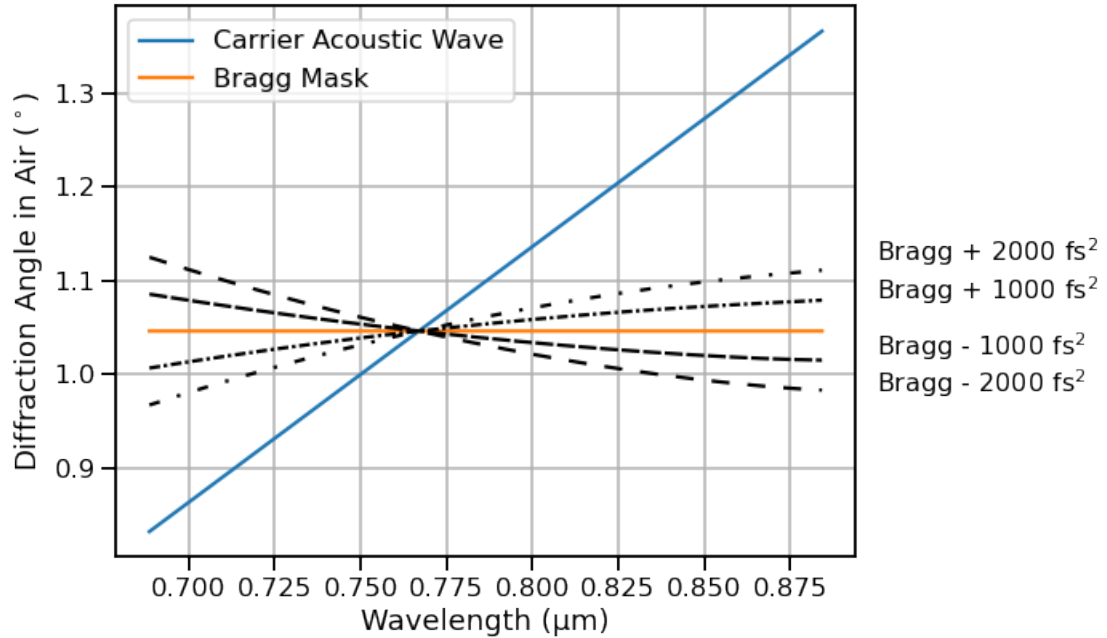
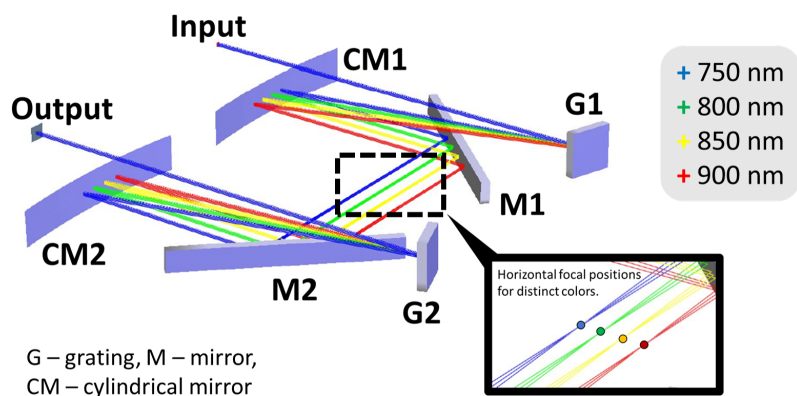


Figure 3.6: Diffraction angles as a function of wavelength for various phase masks.

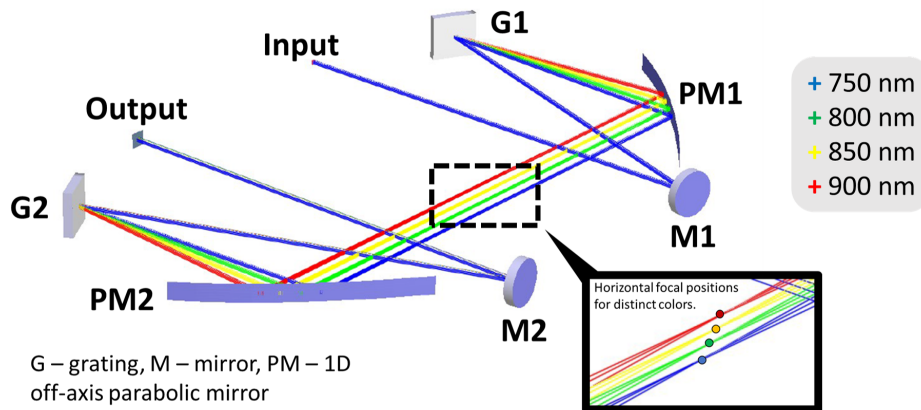
### 3.3.2 Aberrations in Reflective 4f Designs

Here, I compare the aberrations imparted onto a half-octave, NIR pulse by two reflective 4f geometries (Fig. 3.7) that are widely used in Fourier-plane pulse shaping: a cylindrical-mirror design and a parabolic-mirror design (both supplied by PhaseTech Spectroscopy, Inc.). We have published this work in Ref. [52]. The parabolic-mirror design has been found to greatly simplify alignment, especially of infrared beams [46], and has been particularly beneficial for 2D IR and 2D visible spectroscopy [55, 130] and 2D microscopy [100]. The cylindrical-mirror design avoids parabolic optics but has the additional complexity of a

vertical displacement and closely overlapping beam paths. We calculated the amount of spatial chirp and chromatic astigmatism on the output of each design using measured data and compared the results to calculations from a commercially available ray-tracing software (FRED, Photon Engineering, LLC), finding strong agreement. Understanding the tradeoffs of these designs, summarized below, is essential for applications utilizing ultrabroad femtosecond pulses.



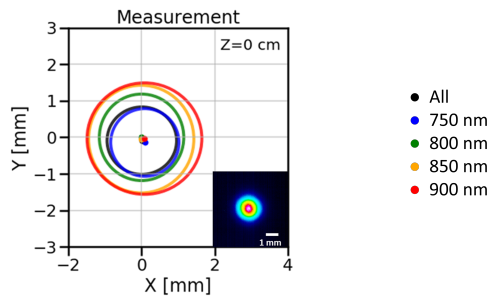
(a) Cylindrical-mirror design.



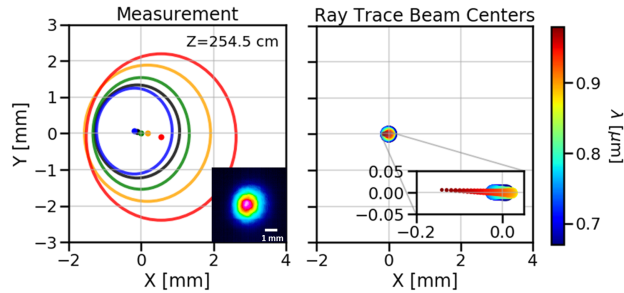
(b) 1-D off-axis parabolic-mirror design.

Figure 3.7: Schematics of (a) the cylindrical-mirror design and (b) the 1-D off-axis parabolic-mirror design [52].

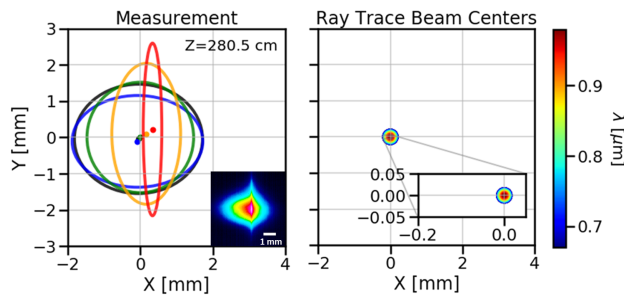
To determine the chromatic aberrations, such as spatial chirp and chromatic astigmatism, we measured beam properties of white light continuum spanning 650–950 nm with a CCD camera at various positions relative to the shaper out-



(a) White light beam at the input of the pulse shapers.



(b) Cylindrical-mirror design output.



(c) 1-D off-axis parabolic-mirror design output.

Figure 3.8: Beam profiles and centroids measured and simulated at the input and outputs of the pulse shapers for different frequencies [52]. (Left column) Spatial chirp measured with a CCD camera and several 40-nm bandpass filters, with center wavelengths indicated in the legend in (a). (Right column) Ray tracing simulations showing the beam centers as functions of frequency.

put for 4 spectral regions selected using 40-nm bandpass filters centered at 750 nm, 800 nm, 850 nm, and 900 nm. Fig. 3.8 illustrates a dramatic difference in beam quality at the output planes of a cylindrical-mirror design (Fig. 3.8b) and a 1-D off-axis parabolic-mirror design (Fig. 3.8c). These are compared to the beam at the input plane (Fig. 3.8a). Both design outputs exhibit signs of spatial chirp (as seen by the transverse spread of beam centroids) and of a frequency-dependent beam shape (as seen by the spread of iso-intensity beam ellipses). The horizontal spatial chirp (spread in X-axis) is stronger for the cylindrical shaper than for the parabolic shaper, while the beam shape variation and distortion are dramatically worse for the parabolic shaper, indicating stronger chromatic astigmatism. To corroborate these measurements, we evaluated each design with ray tracing, covering a half-octave of bandwidth.

We found chromatic astigmatism to be inherent to the parabolic-mirror design. To determine the degree of this effect, we incrementally measured the  $1/e^2$  beam radius as a function of camera position for each spectral region. The data was fit with the equation for Gaussian beam propagation parameterized by the far-field divergence and focal plane position relative to the design output. For comparison, the far-field divergence was calculated from the ray-tracing analysis using the output direction of rays placed at the  $1/e^2$  values of the input beam. The focal plane position was calculated by finding the intersection of rays corresponding to opposite sides of the input beam. Fig. 3.9 shows the horizontal and vertical far-field divergences,  $\Theta_x$  and  $\Theta_y$  respectively, as a function of wavelength determined from experimental measurements (markers with error bars) and from ray tracing (lines). There are several observations of significance. First, the vertical divergence is predicted to be unchanged by either of the 4f systems. This is expected because both designs utilize 1-D curved mirrors.

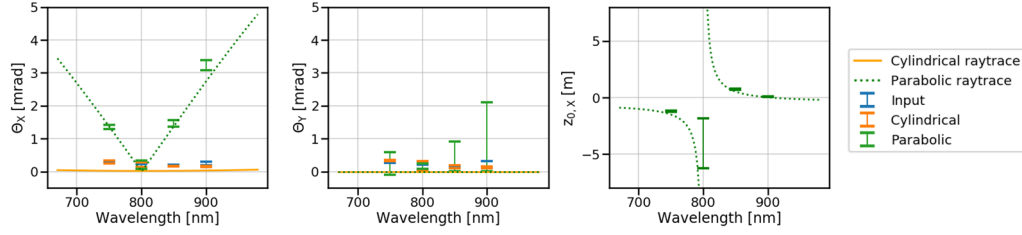


Figure 3.9: The horizontal (left) and vertical (middle) far-field divergences,  $\Theta_X$  and  $\Theta_Y$  respectively, and the horizontal focal position of the parabolic shaper relative to the output plane,  $z_{(0,X)}$ , (right) calculated from measurements (markers with error bars) and from ray tracing (lines) as a function of wavelength for the input beam (blue), the cylindrical-design output (orange), and the parabolic-design output (green) [52].

Second, the parabolic-mirror design is found to dramatically affect the horizontal divergence. The far-field divergences calculated from measurements and ray tracing match closely. To further investigate the chromatic astigmatism from the parabolic design, we calculated the color-dependent horizontal focal plane position relative to the parabolic design output plane,  $z_{0,X}$ , from experimental and ray-tracing data (right-hand panel of Fig. 3.9), which show close agreement.

The chromatic aberrations in the parabolic-mirror design arise from a frequency-dependent displacement of the beam’s focus from the center plane of the  $4f$  geometry. The focus for wavelengths larger (smaller) than the wavelength centered on the parabolic mirror, 800-nm for our case, is behind (before) the center plane and closer (farther) from the second parabolic mirror. Therefore, the only wavelength that is well collimated at the output of the parabolic-mirror design is the centered wavelength with the smaller wavelengths diverging and the larger wavelengths converging. Ultimately, this chromatic astigmatism severely affects the quality of the beam’s focus. Fig. 3.10 shows the measured horizontal and vertical  $1/e^2$  beam radii,  $w_X$  and  $w_Y$ , for each spectral region as a function of distance from a 50-cm concave mirror for the cylindrical-mirror design (top row)

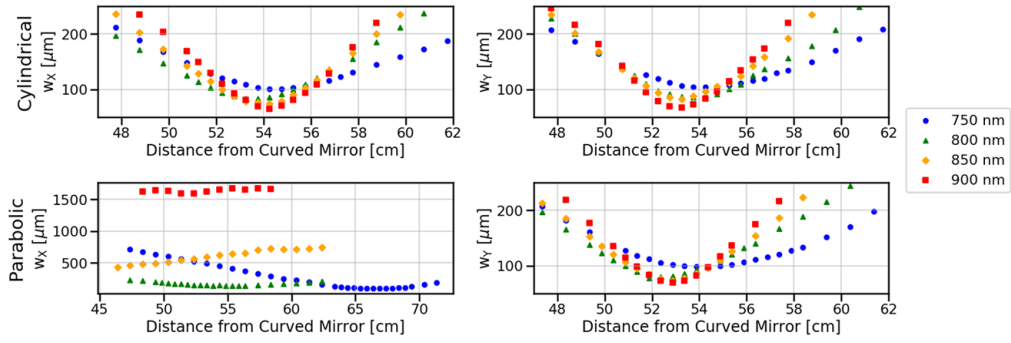


Figure 3.10: Measured horizontal (left) and vertical (right)  $1/e^2$  beam radii,  $w_x$  and  $w_y$ , of spectral ranges from 750 nm to 900 nm as a function of distance from a 50-cm concave mirror for the cylindrical-mirror design (top row) and the parabolic-mirror design (bottom row). The small variation in focal position along the vertical dimension is due to inherent chromatic aberration in the white light source [52].

and the parabolic-mirror design (bottom row). Comparing the two designs, the larger degree of chromatic astigmatism imparted by the parabolic-mirror design is evident from the variation in the horizontal focal position for each color. A shorter focal length optic, as would typically be used in pump-probe or multidimensional spectroscopy, would bring the focal planes closer together but cannot eliminate the chromatic variation in divergence angle.

In Fig. 3.8, we show the ray-tracing calculations for the deviations of beam centers along horizontal and vertical axes relative to the 800-nm ray (right column). The ray tracing predicts that the cylindrical-mirror design imparts a spatial chirp of more than 100  $\mu\text{m}$  in the horizontal dimension—mostly on the long wavelength end of the spectrum—and a small amount in the vertical dimension over the half-octave of bandwidth, while the parabolic-mirror design exhibits no spatial chirp.

In summary, we found a tradeoff between the amount of spatial chirp and chromatic astigmatism imparted by two 4f pulse shaping designs, a cylindrical-

mirror design and a 1-D off-axis parabolic-mirror design. On one hand, the cylindrical-mirror design suffers from larger spatial chirp, and, on the other, the parabolic-mirror design suffers from severe chromatic astigmatism. These results show that the cylindrical-mirror design, while more difficult to align, provides superior beam quality than the parabolic-mirror design for applications such as nonlinear frequency conversion. While the chromatic astigmatism may not be a large factor in the shaping of narrower-bandwidth pulses (e.g., from standard many-cycle-pulse OPAs), its consideration becomes essential when shaping ultrabroadband pulses from few-cycle sources. Based on this study, we implemented two cylindrical-mirror 4f pulse shapers (PhaseTech Spectroscopy, Inc.) for dispersion management and amplitude and phase control of the pulses from our NIR front end.

## CHAPTER 4

### MULTICOLOR, FEMTOSECOND SOURCE ARCHITECTURE

In this chapter, I will review how our multicolor, 10-fs laser source is realized using adiabatic frequency conversion combined with our energetic, 10-fs NIR front end and NIR 4f pulse shapers. Adiabatic frequency conversion was recently shown to allow arbitrarily shapeable microjoule pulses with single-cycle duration in the MIR, facilitated by a linear spectral phase and amplitude transfer [69], thus greatly simplifying the technical requirements of arbitrary pulse shaping across a hyperspectral platform. The advancements in broadband parametric amplification, pulse shaping, and adiabatic frequency conversion have coalesced to enable a uniquely suited, flexible spectroscopy source, allowing the combination and arbitrary shaping of microjoule-energy, 10-fs pulse sequences covering several octaves at UV/visible, NIR, and MIR wavelengths. Note, some of the content of this chapter was published in Ref. [51].

#### 4.1 ARCHITECTURE

The architecture of the multicolor, 10-fs source is shown in Fig. 4.1. We chose three distinct bands for simultaneous operation, at visible (0.45–0.51  $\mu\text{m}$ ), MIR (1.9–4.3  $\mu\text{m}$ ), and NIR (0.67–0.95  $\mu\text{m}$ ) frequency ranges, each with transform-limited duration  $\sim 10$  fs. We note that upconversion, downconversion, and OPCPA stages can be added to cover additional spectral ranges.

The design utilizes our energetic NIR front end based on a high-average-power (180-W) 10-kHz Yb:YAG amplifier (Amphos GmbH) operating at 1030 nm, WLG, and noncollinear OPCPA combined with dual NIR pulse shapers.

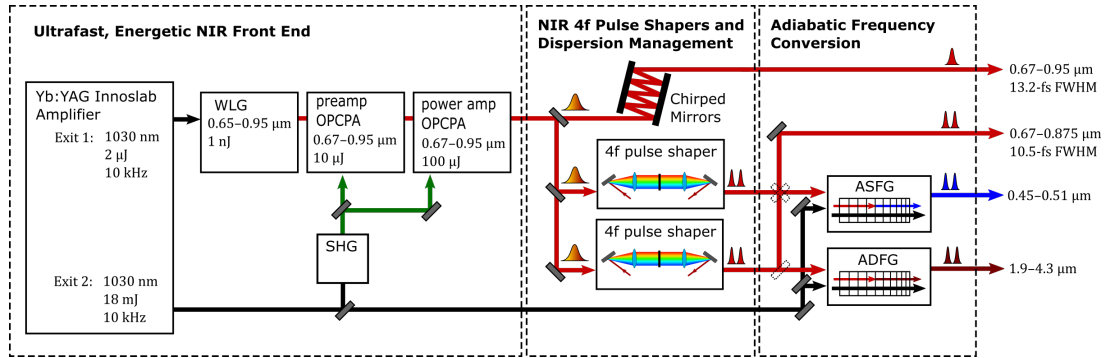


Figure 4.1: Multicolor source architecture composed of our ultrafast, energetic NIR front end, NIR 4f pulse shapers, and adiabatic frequency conversion stages, each outlined by a dashed box. Shaped visible, NIR, and MIR pulses are produced through adiabatic conversion of shaped NIR pulses. The available spectral bandwidths are shown on the right side of the figure.

The Yb:YAG amplifier has two exit ports that share a common preamplifier, ensuring optical synchronization. From the first exit port, 900-fs pulses pump WLG in bulk YAG to generate a visible/NIR continuum. The second exit port generates 3-ps pulses that are frequency doubled to pump a two-stage non-collinear OPCPA to generate amplified NIR pulses with  $>100\text{-}\mu\text{J}$  energy. More details on the NIR front end can be found in Chapter 2.

Pre-conversion dispersion management and arbitrary pulse shaping is achieved with a pair of NIR 4f pulse shapers (PhaseTech Spectroscopy, Inc.). These shapers admit an optical bandwidth of 170 nm (tunable by choice of diffraction gratings) and have an update rate up to 25 kHz. The shaped NIR pulses from the front end are then directed to the various adiabatic conversion stages, where they mix in aperiodically-poled quasi-phase-matched gratings with a strong (up to  $200\text{-}\mu\text{J}$  energy) 1030-nm pump pulse from the Yb:YAG amplifier. Visible and MIR pulses are generated through adiabatic sum frequency generation (ASFG) in KTP (Raicol Crystals) and adiabatic difference frequency generation (ADFG) in lithium niobate (HC Photonics), respectively. Impor-

tantly, adiabatic frequency conversion enables a linear transfer of spectral amplitude through near-one-to-one photon number conversion—nearly every NIR photon is converted to the targeted range—as well as a linear transfer of spectral phase [69]. Thus, our source architecture is designed to allow dispersion management and pulse shaping for each spectral range through a NIR pulse shaper prior to the conversion stage, eliminating a need for separate post-conversion shaping devices for each spectral range. Moreover, the aperiodically-poled adiabatic conversion gratings are designed to employ intrinsic pulse shaping—the use of wavelength dependent longitudinal conversion positions—to achieve simultaneous adiabatic phase matching and cancellation of the complex material group delay dispersion (GDD) through the device [43]. The result is a device with zero net GDD, eliminating the need for post-conversion dispersion management.

We note several more advantages of our source architecture for hyperspectral and ultrafast nonlinear spectroscopy. With programmable pulse shaping entirely carried out within the fixed NIR front end, the rapid control of pulse sequences afforded by pulse-shaper-assisted multidimensional spectroscopy in a “pump-probe” geometry [123], such as the use of phase-cycling, pi-shifting for background subtraction, and interferometrically stable control of pulse pair delay, can be extended over multiple octaves of bandwidth. The 180-W average power of the pump laser allows operation at a 10-kHz repetition rate while maintaining microjoule pulse energies, which enables fast acquisition of multidimensional spectra when combined with the rapid update rate of the pulse shapers and 10-kHz acquisition rate of modern MCT array detectors. Finally, the use of orientation patterned semiconductors [118] as adiabatic conversion stages could potentially extend the hyperspectral range to the molecular finger-

print region of the mid-IR.

## 4.2 ADIABATIC FREQUENCY CONVERSION

The concept of adiabatic frequency conversion is critical to the operation of our multicolor, femtosecond spectroscopy source. Here, the principle of adiabatic frequency conversion is reviewed in analogy to the well-known phenomenon of rapid adiabatic passage in two-level atomic systems. Additionally, the aperiodically-poled crystals used in adiabatic frequency conversion can be engineered to control the phase of the output pulse, enabling a uniquely-suited tool for broadband frequency conversion and phase control or dispersion management.

Adiabatic difference frequency generation (ADFG) and adiabatic sum frequency generation (ASFG) are used to downconvert and upconvert the shaped, broadband, and energetic NIR front end pulses to the MIR or visible spectral regions, respectively. Adiabatic processes have been thoroughly studied through the context of two-level systems [81, 124], in which robust population transfer between the two states is realized through rapid adiabatic passage. Within the field of nonlinear optics, the use of rapid adiabatic passage was first proposed for highly-efficient second harmonic generation [7, 8] and later extended to sum frequency generation (SFG) and difference frequency generation (DFG) [133, 135]. Within the past decade, various research groups have developed and advanced this technique for efficient, broadband nonlinear frequency conversion or amplification [53, 85, 91, 102, 131, 132, 134], overcoming the efficiency-bandwidth tradeoff problem that limits the performance of traditional three-

wave mixing processes. ADFG was implemented for frequency conversion of ultrashort pulses [69, 132], demonstrating the generation of greater-than-octave spanning MIR pulses.

First, let us review the concept of rapid adiabatic passage in the context of coherent excitation of a two-level atomic system [17, 81, 124, 142]. Consider a two-level atomic system composed of a ground state,  $g$ , and an excited state,  $e$ , that is either (1) suddenly exposed to a driving field or (2) slowly perturbed as the driving field is quasistatically swept through resonance. In the first case, the probability of the atom existing in the ground or excited state,  $\mathcal{P}_g$  and  $\mathcal{P}_e$  respectively, varies sinusoidally as the system undergoes Majorana or Rabi oscillations [105]. For an ensemble of atoms that exhibit inhomogeneous spectral broadening of the resonant frequency, each atom will experience nonuniform Rabi oscillations as those with resonant frequencies closest to that of driving field will have longer oscillation cycles compared to those with resonant frequencies farther from that of driving field. In the second case, as the driving frequency is slowly swept through the resonant frequency, the atomic state changes monotonically from the ground state to the excited state—this is known as *rapid* adiabatic passage since the interaction takes place on a timescale much less than the radiative lifetime. For the ensemble of atoms with inhomogeneous spectral broadening, each atom is driven to the excited state as the frequency of the driving field is swept through the inhomogeneous resonance of the ensemble, enabling robust and efficient population transfer.

Mathematically, the dynamics of the two-level atomic system driven by coherent laser excitation are described by the time-dependent Schrödinger equa-

tion

$$j\hbar \frac{d}{dt} C(t) = \mathcal{H}(t)C(t), \quad (4.1)$$

where  $\hbar$  is Planck's constant,  $C$  is a column vector containing the probability amplitudes of the ground and excited states, and  $\mathcal{H}$  is the system Hamiltonian. The diagonal elements of  $\mathcal{H}$  are the energies of the ground and excited states, and the off-diagonal elements are the coupling parameters between the atom-laser interaction. Under the rotating-wave approximation, the Hamiltonian can be expressed as

$$\mathcal{H}(t) = \hbar \begin{bmatrix} 0 & \frac{1}{2}\Omega(t) \\ \frac{1}{2}\Omega(t) & \Delta(t) \end{bmatrix}, \quad (4.2)$$

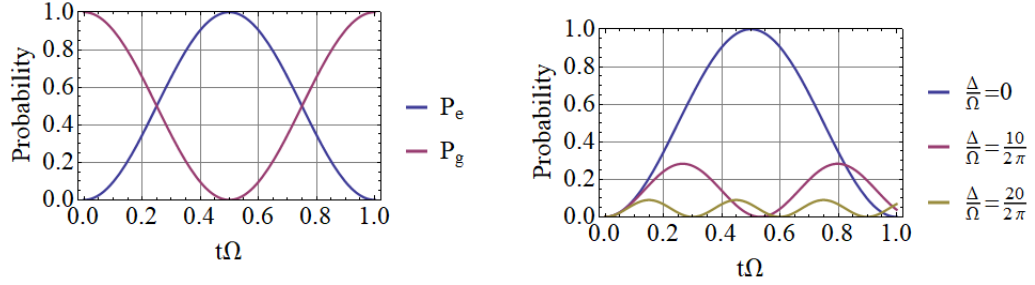
where  $\Omega(t)$  is the Rabi frequency and  $\Delta(t)$  is the detuning<sup>1</sup> with the ground state used as the reference energy level. Combining Eqs. 4.1 and 4.2 gives the equation of motion for the two-level atomic system,

$$j \frac{d}{dt} \begin{pmatrix} C_g \\ C_e \end{pmatrix} = \begin{pmatrix} 0 & \frac{1}{2}\Omega(t) \\ \frac{1}{2}\Omega(t) & \Delta(t) \end{pmatrix} \begin{pmatrix} C_g \\ C_e \end{pmatrix}. \quad (4.3)$$

If  $\Omega$  and  $\Delta$  do not depend on time, the solution to this set of equations are the familiar Rabi oscillations, shown in Fig. 4.2. The left panel (a) shows a single Rabi cycle demonstrating full conversion from the ground state to the excited state when the laser excitation frequency is equal to the Bohr Frequency,  $\Delta = 0$ . The right panel (b) shows the excited state probability for various values of detuning. Now, if  $\Omega$  and  $\Delta$  depend on time, more complex and interesting dynamics can occur. Specifically, if  $\Delta$  is swept from a very negative to a very positive value such that the change in  $\mathcal{H}$  occurs sufficiently slowly, full conversion from the ground state to the excited state can be achieved [124]. This is

---

<sup>1</sup>In this system, the detuning is the difference between the Bohr transition frequency and the laser carrier frequency.



(a) Rabi oscillations in the occupation probability of the ground and excited state ( $\mathcal{P}_g$  and  $\mathcal{P}_e$  respectively) of a two-level atomic system. The detuning,  $\Delta$ , is set to zero resulting in full probability conversion to the excited state.

(b) Occupation probability of the excited state of a two-level atomic system for various values of  $\Delta/\Omega$ , the ratio between the detuning and the Rabi frequency.

Figure 4.2: Rabi oscillations in a two-level atomic system.

known as rapid adiabatic passage and is achieved when

$$|\dot{\tilde{\Omega}}(t)\Delta(t) - \Omega(t)\dot{\Delta}(t)| \ll 2|\tilde{\Omega}(t)|^3 \quad (4.4)$$

where  $\tilde{\Omega} \equiv \sqrt{\Omega(t)^2 + \Delta(t)^2}$  is the generalized Rabi frequency. Equation 4.4 is known as the adiabatic condition.

When the detuning is a linear function of time ( $\frac{\partial}{\partial t}\Delta = \alpha$ ) and the Rabi frequency is kept fixed, the resulting dynamics follow the Landau-Zener Theory of rapid adiabatic passage [73, 154], which states that the probability of transition between the two states is given by

$$\mathcal{P}_e = \exp\left[-2\pi\left(\frac{\Omega^2}{4|\alpha|}\right)\right]. \quad (4.5)$$

Equation 4.5 is plotted in Fig. 4.3 and illustrates how full conversion can be achieved with a sufficient rate of detuning for a given Rabi frequency.

Rapid adiabatic passage can be achieved in three-wave mixing. The set of coupled wave equations for three-wave mixing shown in Eq. 2.5 can be simplified to a system of two coupled equations by assuming that the pump field

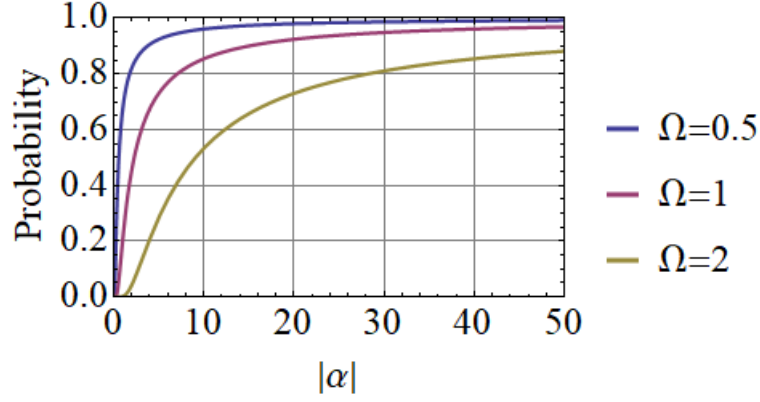


Figure 4.3: Conversion probability of a two-level atomic system using a linear sweep rate of the detuning,  $\alpha = \frac{\partial}{\partial t}\Delta$ , for various Rabi frequencies.

is much stronger than the other two—for DFG  $I_s \gg I_i, I_p$ —and performing the change of variables,  $\tilde{A}_p \equiv \frac{\sqrt{k_p}}{\omega_p A_s} A_p$  and  $\tilde{A}_i \equiv \frac{\sqrt{k_i}}{\omega_i A_s} A_i$ , such that

$$\frac{d\tilde{A}_p}{dz} = -jk\tilde{A}_i e^{j\Delta kz} \quad (4.6a)$$

$$\frac{d\tilde{A}_i}{dz} = -jk^* \tilde{A}_p e^{-j\Delta kz}, \quad (4.6b)$$

where  $\kappa = \frac{d_{\text{eff}}\omega_p\omega_i}{\sqrt{k_p k_i} c_0^2} A_s$ . Furthermore, by using a rotating reference frame, these equations can be expressed in matrix form as

$$j\frac{\partial}{\partial z} \begin{pmatrix} \tilde{A}_p \\ \tilde{A}_i \end{pmatrix} = \begin{pmatrix} \Delta k(z) & \kappa \\ \kappa^* & -\Delta k(z) \end{pmatrix} \begin{pmatrix} \tilde{A}_p \\ \tilde{A}_i \end{pmatrix}. \quad (4.7)$$

Note, this is the same form as the equation of motion for a two-level atomic system described in Eq. 4.3. Thus, under the right conditions, full population transfer can be achieved between the two fields,  $A_p$  and  $A_i$ . See Suchowski et al. [133] for a comparison of rapid adiabatic passage in two-level atomic excitation and adiabatic sum frequency generation. In three-wave mixing, the wave-vector mismatch,  $\Delta k$ , is analogous to the detuning,  $\Delta$ , while the coupling coefficient,  $\kappa$ , is analogous to the Rabi frequency,  $\Omega$ . To achieve full population transfer,  $\Delta k$  must be swept from a large negative value to a large positive value

or vice versa compared to  $\kappa$ . Specifically, the adiabatic condition is satisfied when

$$\left| \frac{d\Delta k}{dz} \right| \ll \frac{(\Delta k^2 + \kappa^2)^{3/2}}{\kappa}. \quad (4.8)$$

Several groups have designed and implemented aperiodically-poled, quasi-phase-matched nonlinear crystals for adiabatic frequency conversion, setting the foundation for broadband ASFG and ADFG for femtosecond pulse generation in visible and MIR. Suchowski et al. [135] demonstrated robust ASFG and later implemented broadband adiabatic frequency conversion for >30-fs pulse conversion [131]. In 2012, Moses et al. [91] demonstrated fully efficient ADFG proving the theory of complete Landau-Zener adiabatic transfer in three-wave mixing. In 2013, broadband few-cycle MIR pulses were generated using ADFG [132], and later the robust transfer of phase from the input NIR pulses to the output MIR pulses was demonstrated [69].

Adiabatic sum and difference frequency generation are employed in our multicolor, femtosecond source architecture to transfer shaped, femtosecond NIR pulses to the visible and MIR spectral ranges. Aperiodically-poled KTP (Raicol Crystals Ltd.) is used for the ASFG stage, and aperiodically-poled lithium niobate (HC Photonics Corp.) is used for the ADFG stage. The stages were characterized by measuring the fractional depletion of the NIR power spectrum (experimental traces, Fig 4.4). Through each stage, a flat photon-number conversion ranging from 80–90% is observed over a bandwidth corresponding to a 10-fs transform-limited pulse (one optical cycle in the MIR and 8 cycles in the visible). The expected group delay of the zero-GDD ASFG device, calculated by split-step Fourier pulse propagation simulation, is shown as the inset in the left-hand panel of Fig. 4.4. At the time of these measurements,

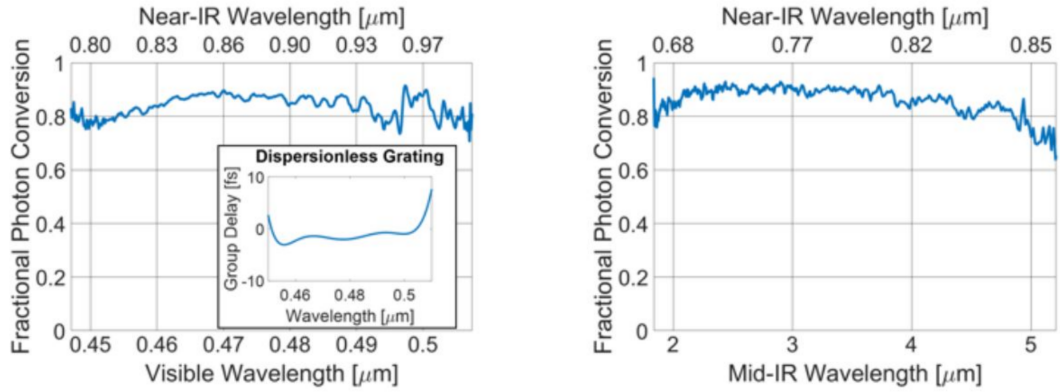


Figure 4.4: Fractional photon conversion of the aperiodically-poled KTP ASFG stage (left) and the aperiodically-poled lithium niobate ADFG stage (right) calculated from the measured fractional depletion of the NIR power spectrum [51].

the ADFG (MIR) device did not employ intrinsic pulse shaping and is based on the design in Krogen et al. [69], which generated single-cycle pulses and pulse pairs through external dispersion management. However, a similar zero-GDD design for the ADFG crystal has an expected peak-to-valley group delay range of 10 fs over the full octave-spanning MIR bandwidth.

### 4.3 INTRINSIC DISPERSION MANAGEMENT

Adiabatic frequency conversion combined with our energetic, femtosecond NIR front end and NIR 4f pulse shapers creates a uniquely-suited platform for efficient generation of amplitude- and phase-controlled femtosecond pulses in the visible, NIR, and MIR. This task, which would typically require independent dispersion compensation for each spectral region, is facilitated by domain-engineering and intrinsic dispersion control in the adiabatic conversion stages. Dispersion and phase engineering in quasi-phase-matched gratings has been implemented in second harmonic generation [3] and difference frequency gen-

eration [57].

There are two main phenomena that contribute to the engineered dispersion of the output pulses from quasi-phase-matched gratings: (1) the intrinsic material dispersion of the grating material resulting in a group velocity mismatch between the NIR pulses and the visible/MIR pulses and (2) the spatial localization of the conversion of different frequencies. For ADFG, with NIR to MIR conversion of each frequency component assumed to be well localized with respect to the length of the grating, the group delay of the MIR pulse is

$$\tau(\omega) = \frac{\partial k_{\text{NIR}}}{\partial \omega} z_c(\omega) + \frac{\partial k_{\text{MIR}}}{\partial \omega} (L - z_c(\omega)), \quad (4.9)$$

where  $L$  is the length of the grating and  $z_c$  is the localized conversion point of the MIR angular frequency,  $\omega$  [69]. The available tuning range of the engineered dispersion is dictated by the group-delay mismatch between the NIR and the MIR angular frequencies. This constraint is shown in Fig. 4.5 for a 2-cm lithium niobate grating using Type-0 phase matching. The group delay of the engineered dispersion function must fall within the range defined by the NIR group delay (blue) and the MIR group delay (orange). To achieve zero GDD, the group delay must be constant over the entire bandwidth of the pulse. Thus, the range of possible group delay is restricted to the smallest value in the NIR bandwidth and the largest value in the MIR bandwidth, shown as the two black, dashed lines in Fig. 4.5.

Conversion positions calculated from Eq. 4.9 resulting in constant group delay are shown in Fig. 4.6. Importantly, not all of these functions would result in adiabatic conversion—the engineered dispersion function must be achievable through a monotonically increasing or decreasing poling period. Moreover, the adiabatic condition requires a relatively slow change in poling period with the

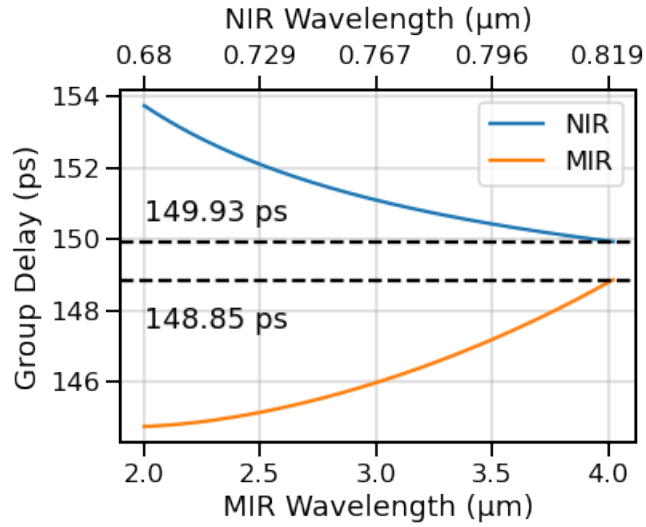


Figure 4.5: Group-delay constraint of the engineered dispersion calculated assuming complete propagation as either NIR (blue) or MIR (orange) in a 2-cm lithium niobate grating using Type-0 phase matching. The black, dashed lines indicate the range of group delay within which zero GDD is possible.

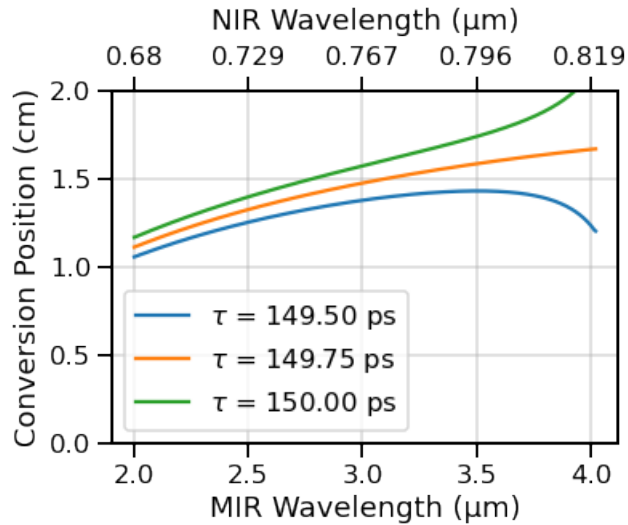
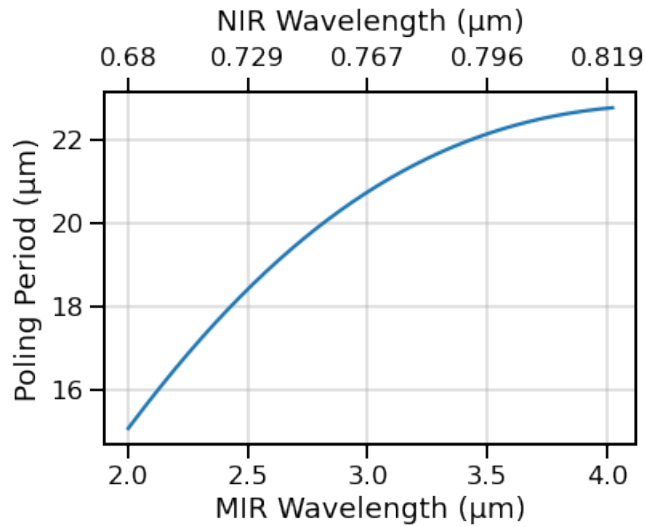


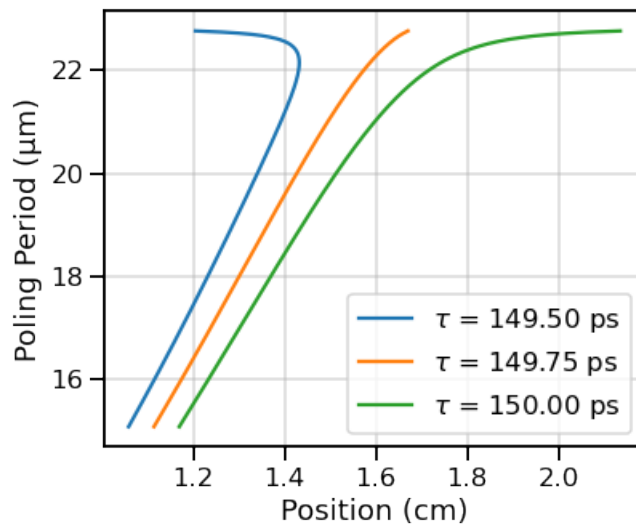
Figure 4.6: Conversion position functions resulting in constant group delay over the target MIR bandwidth. The conversion positions are restricted to 2 cm, the length of our ADFG lithium niobate grating.

maximum rate dictated by the pump intensity, which is limited by the laser-induced damage threshold of the grating material. The poling period required to phase match Type-0 difference frequency generation with a 1.03- $\mu\text{m}$  pump wavelength in lithium niobate is shown in Fig. 4.7a. In Fig. 4.7b, the poling period as a function of position in the lithium niobate grating (i.e. the conversion position within the grating) resulting in the constant group delay values in Fig. 4.6 is plotted. Note, the function resulting in  $\tau = 149.5$  ps (blue) is not monotonic and would therefore not result in adiabatic conversion. Additionally, the function resulting in  $\tau = 150.00$  ps (green) requires a crystal length  $>2$  cm, a length longer than our device, to achieve a constant group delay over the MIR range shown—furthermore, to ensure adiabatic conversion, enough crystal length must remain to adiabatically sweep the poling period away from that of the spectral extremum. Ultimately, the grating function must be carefully designed such that the adiabatic condition can be satisfied over the entire bandwidth of interest.

For our 10-fs multicolor architecture, we designed dispersion-managed adiabatic sum and difference frequency conversion stages that use engineered poling periods to translate our compressed and shaped NIR pulses spanning 680–820 nm to compressed and shaped visible (450–510 nm) and MIR (2–4  $\mu\text{m}$ ) pulses respectively. These new dispersion-managed stages allow efficient, broadband conversion *without* the need of additional, complex dispersion management that is required for traditional frequency conversion and adiabatic frequency conversion stages [69]. As a result, the 13.5-fs NIR pulses emerging from our 4f pulse shapers can be immediately converted to transform-limited visible or MIR pulses, simply by combining them with a pump pulse in our dispersion-managed device. We anticipate that these devices will allow the development



(a) Poling period required to phase match Type-0 difference frequency generation with a 1.03- $\mu\text{m}$  pump wavelength in lithium niobate.



(b) Poling period as a function of position within the grating (i.e. conversion position,  $z_c$ ) resulting in constant group delays of 149.5 ps (blue), 149.75 ps (orange), and 150.00 ps (green).

Figure 4.7: Poling periods for Type-0 phase matching in lithium niobate.

of new sources in the ultrafast community, as new femtosecond beamlines in different spectral regions could be easily added to existing nonlinear spectrometers, facilitating novel multicolor, ultrafast studies spanning broad frequency ranges.

## CHAPTER 5

### EXPERIMENT TO DEMONSTRATE ZERO GROUP DELAY DISPERSION IN AN OCTAVE-SPANNING ADIABATIC FREQUENCY CONVERTER

Adiabatic frequency conversion allows efficient and broadband conversion of ultrafast pulses through three key properties: (1) a one-to-one photon number conversion, (2) a linear transfer of amplitude and phase, and (3) the preservation of absolute bandwidth. However, the inherent, localized frequency-dependent conversion positions, discussed in Chapter 4, result in a complex dispersion profile that can only be compensated using complicated and often expensive dispersion management, such as pulse shapers or custom-designed chirped mirrors. In a recent demonstration of adiabatic frequency conversion, Krogen et al. [69] converted shaped, broadband NIR pulses to shaped, few-cycle, octave-spanning MIR pulses, but their adiabatic frequency conversion stage imparted complex dispersion, requiring a pulse shaper for compensation. Often, a pulse shaper is not available, and, when one is, the limited shaping capabilities would ideally be reserved for amplitude and phase control of pulse sequences used in nonlinear spectroscopy.<sup>1</sup>

To avoid complicated dispersion management while taking advantage of the properties of adiabatic frequency conversion, we implemented intrinsic dispersion management in the grating design, creating a dispersion-managed adiabatic frequency converter. The concept of intrinsic dispersion management in adiabatic frequency conversion is discussed in Section 4.3. Our design allows shaped, transform-limited NIR pulse sequences to be converted to shaped, transform-limited visible or MIR pulse sequences—removing the requirement

---

<sup>1</sup>With 4f pulse shapers using acousto-optic modulators, there is a limited radio-frequency (RF) bandwidth supported by the RF amplifiers and acousto-optic transducer.

of separate dispersion management and pulse shaping in each spectral range. Ultimately, this device could be used to transfer any existing transform-limited pulse to another transform-limited pulse in a different frequency range by adding one additional stage. This concept is shown in Fig. 5.1 where a compressed, multi-cycle NIR pulse is converted to a compressed, single-cycle MIR pulse through a dispersion-managed adiabatic difference frequency converter. Note, the absolute bandwidth of the input pulse,  $\Delta\omega$ , and the pulse duration,  $\Delta t$ , is preserved through conversion. In the next few sections, I will describe our

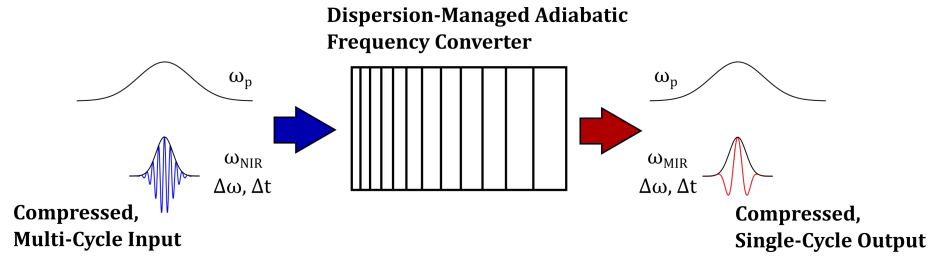


Figure 5.1: Overview of dispersion-managed ADFG. A compressed multi-cycle NIR pulse at angular frequency  $\omega_{\text{NIR}}$  is converted to a compressed single-cycle MIR pulse at angular frequency  $\omega_{\text{MIR}}$  when combined in the dispersion-managed adiabatic frequency converter with a strong pump field at angular frequency  $\omega_p$ . Both absolute bandwidth  $\Delta\omega$  and pulse duration  $\Delta t$  of the input field are preserved.

dispersion-managed ADFG setup and discuss preliminary experimental results demonstrating the performance of this device through the imparted phase and group delay, which are measured by characterizing the input NIR pulse and the output MIR pulse.

## 5.1 SETUP AND PHASE CALCULATION

The dispersion-engineered ADFG stage consists of a 2-cm, aperiodically-poled lithium niobate grating, designed to have constant group delay for a MIR band-

width spanning 2–4  $\mu\text{m}$ . The stage is pumped with 200- $\mu\text{J}$  pump pulses at 1030-nm, stretched to approximately 6-ps FWHM. The pump beam is focused to a spot size to produce a peak intensity of 25  $\text{GW}/\text{cm}^2$ , resulting in 70% energy depletion of the incident NIR power spectrum, which is filtered with a 140-nm square filter centered around 750 nm using the 4f pulse shaper to ensure the transmitted bandwidth lies within the operating range of the dispersion-engineered grating. A schematic of our dispersion-managed adiabatic frequency conversion stage and the beam routes used for pulse characterization are shown in Fig. 5.2. The compressed NIR pulse is combined with the 1030-

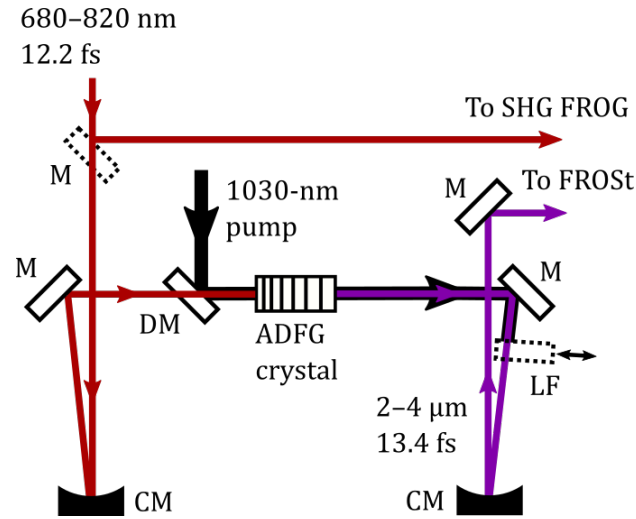


Figure 5.2: Schematic of our dispersion-managed adiabatic difference frequency generation stage used to convert a transform-limited input NIR pulse to a transform-limited output MIR pulse. Beam routes for pulse measurements are indicated. M–mirror, CM–concave mirror, DM–dichroic mirror, LF–longpass filter

nm pump pulse in the ADFG crystal using a dichroic mirror (DMSP1000, Thorlabs). After conversion, a 1.65- $\mu\text{m}$  longpass filter (1.65ILP-25, Andover) is used to block the pump and any residual NIR light from the MIR output. By measuring the input NIR pulse and the output MIR pulse, the spectral phase imparted by our device can be calculated. The NIR pulse is measured using SHG

frequency-resolved optical gating (FROG), and the MIR pulse is measured using frequency-resolved optical switching (FROSt) [76]. However, optics between the measurement stages—other than our frequency converter—add additional dispersion that must be accounted for analytically or empirically. In total, there are three of these optics: (1) the dichroic mirror, (2) the beam splitter in the SHG FROG setup (BSW29R, Thorlabs), and (3) the longpass filter. The phase imparted by the dichroic mirror  $\phi_{DM}$  and the beam splitter  $\phi_{BS}$  must be accounted for analytically. However, we can account for the phase from the longpass filter  $\phi_{LF}$  by taking two FROSt measurements of the MIR pulse, one with a single pass through the filter and one with two passes through the filter, by translating it in and out of the second pass as shown in Fig. 5.2.

To calculate the spectral phase imparted by the device  $\phi_D$ , let us consider the phases imparted by each component ( $\phi_{BS}$ ,  $\phi_{DM}$ ,  $\phi_D$ , and  $\phi_{LF}$ ) and the measured phases ( $\phi_{NIR}$ —NIR phase measured with SHG FROG,  $\phi_{MIR}^{(1)}$ —MIR phase measured with FROSt with one pass through the longpass filter, and  $\phi_{MIR}^{(2)}$ —MIR phase measured with FROSt with two passes through the longpass filter). Consider a pulse starting at the tail of the red arrow in Fig. 5.2 with a phase  $\phi_{in}$  before the dichroic mirror. After passing through the dichroic mirror and ADFG crystal, the output phase is

$$\phi_{out} = \phi_{in} + \phi_{DM} + \phi_D. \quad (5.1)$$

Now,  $\phi_{in}$  is determined by the SHG FROG measurement using

$$\phi_{in} = \pm\phi_{NIR} - \phi_{BS}, \quad (5.2)$$

where the  $\pm$  comes from the sign ambiguity inherent in SHG FROG. Combining Eqs. 5.1 and 5.2 yields

$$\phi_{out} = \pm\phi_{NIR} - \phi_{BS} + \phi_{DM} + \phi_D. \quad (5.3)$$

Next, the phase imparted by the longpass filter can be accounted for using the FROSt measurements,

$$\phi_{\text{MIR}}^{(1)} = \phi_{\text{out}} + \phi_{\text{LF}} \quad (5.4a)$$

$$\phi_{\text{MIR}}^{(2)} = \phi_{\text{out}} + 2\phi_{\text{LF}}, \quad (5.4b)$$

where  $\phi_{\text{MIR}}^{(1)}$  is the MIR phase measured with one pass through the longpass filter and  $\phi_{\text{MIR}}^{(2)}$  is the MIR phase measured with two passes through the longpass filter. Subtracting Eq. 5.4b from twice Eq. 5.4a gives

$$2\phi_{\text{MIR}}^{(1)} - \phi_{\text{MIR}}^{(2)} = \phi_{\text{out}}. \quad (5.5)$$

Finally, the phase imparted by the device can be calculated by substituting Eq. 5.3 into Eq. 5.5 and solving for  $\phi_D$ ,

$$\phi_D = 2\phi_{\text{MIR}}^{(1)} - \phi_{\text{MIR}}^{(2)} \mp \phi_{\text{NIR}} - \phi_{\text{DM}} + \phi_{\text{BS}}. \quad (5.6)$$

Thus, the phase imparted by the device can be determined with three phase measurements,  $\phi_{\text{MIR}}^{(1)}$ ,  $\phi_{\text{MIR}}^{(2)}$ , and  $\phi_{\text{NIR}}$ , while analytically accounting for the phase imparted by the dichroic mirror and beam splitter.

## 5.2 NIR PULSE MEASUREMENT

First, we characterized the input NIR pulse using SHG FROG to obtain  $\phi_{\text{NIR}}$ . The pulse was compressed and spectrally filtered to the operational bandwidth of our dispersion-managed device using the NIR pulse shaper. The SHG FROG trace was taken with a home-built background-free, dispersion-balanced autocorrelator converted into a SHG FROG measurement device, as shown in Fig. 5.3. The measured and retrieved traces are shown in Fig. 5.4. The principal

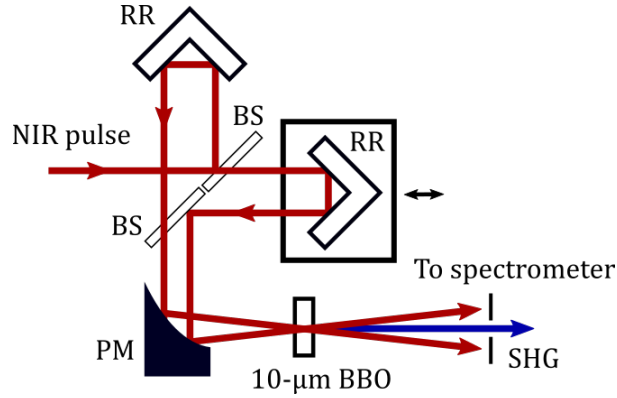


Figure 5.3: Home-built SHG FROG setup using a background-free, dispersion-balanced autocorrelator. The SH signal generated in a thin nonlinear crystal is measured using a visible spectrometer. RR—retroreflector, BS—beam splitter, PM—parabolic mirror

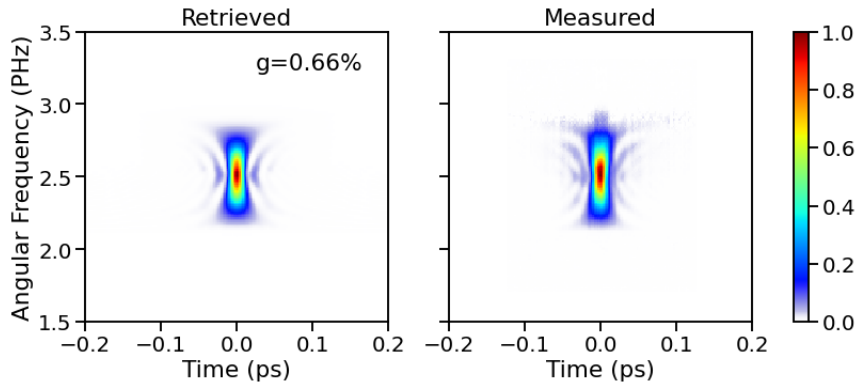


Figure 5.4: Measured (right) and retrieved (left) SHG FROG traces. The retrieved trace error is 0.66%.

component general projection algorithm (PCGPA) was used for the electric field retrieval [24, 61, 62]. The measured trace was corrected based on the frequency marginal of the measured spectrum. During the retrieval, the pulse spectrum was constrained to the measured NIR spectrum, resulting in a  $g$  error of 0.66% as defined in Refs. [138, 139]. The retrieved pulse intensity and phase are shown in Fig. 5.5a, and the spectral intensity and phase are shown in Fig. 5.5b. The FWHM pulse duration was measured as 13.5 fs, which is 1.1 times the calculated transform-limited pulse duration.

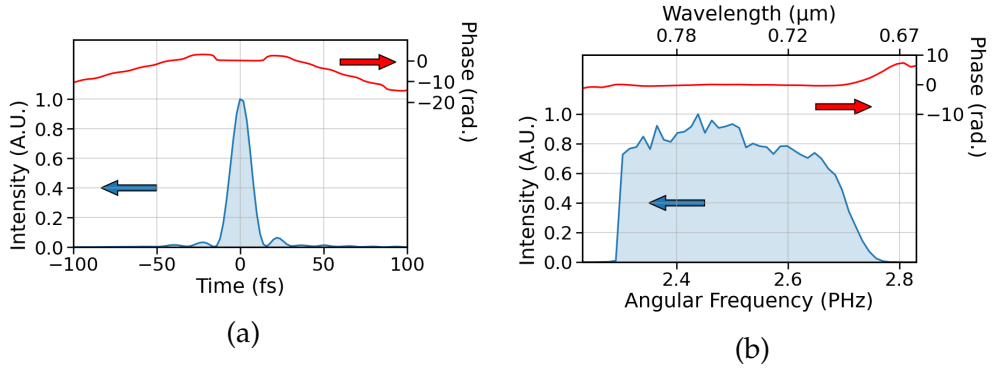


Figure 5.5: (a) Retrieved pulse intensity (blue) and phase (red) of the NIR pulse using SHG FROG. The measured FWHM pulse duration is 13.5 fs, 1.1 times the transform-limited pulse duration, 12.2 fs. (b) Retrieved spectral intensity (blue) and phase (red).

### 5.3 MIR PULSE MEASUREMENT

Next, we characterized the output MIR pulse with one and two passes through the 1.65- $\mu\text{m}$  longpass filter to obtain  $\phi_{\text{MIR}}^{(1)}$  and  $\phi_{\text{MIR}}^{(2)}$  respectively. Because we are using our device to convert a transform-limited NIR pulse to a transform-limited MIR pulse, the amount of input pulse energy is restricted due to the high peak intensity in the crystal. We note significant spatial distortions of the NIR beam through the ADFG crystal as well as visible WL generation for pulse energies  $>0.3 \mu\text{J}$ . With the resulting limited MIR energy, pulse characterization using SHG FROG was not possible. Instead, we implemented a sensitive, phase-matching-free pulse measurement technique, known as frequency resolved optical switching (FROSt), to characterize the MIR pulse [76]. Recently, this technique was used to measure the duration of  $>$ octave-spanning pulses [77]. FROSt uses a pump-probe setup with a semiconductor sample. The frequency of the pump pulse lies above the bandgap of the semiconductor and is focused to a fluence that excites a high density of free carriers, producing a transient absorption response. Thus, the high frequency pump pulse acts as an ultrafast optical

switch while the pulses to be characterized probe the transient absorption response. The probe spectrum is recorded as a function of delay between the pump and the probe pulses, and a ptychography phase retrieval algorithm is used to reconstruct the switch function and the electric-field profile of the probe pulse.<sup>2</sup>

Our FROSt setup, shown in Fig. 5.6, uses a 2-mm thick Si sample that is pumped with a NIR pulse. For the NIR pump, a portion of the NIR beam

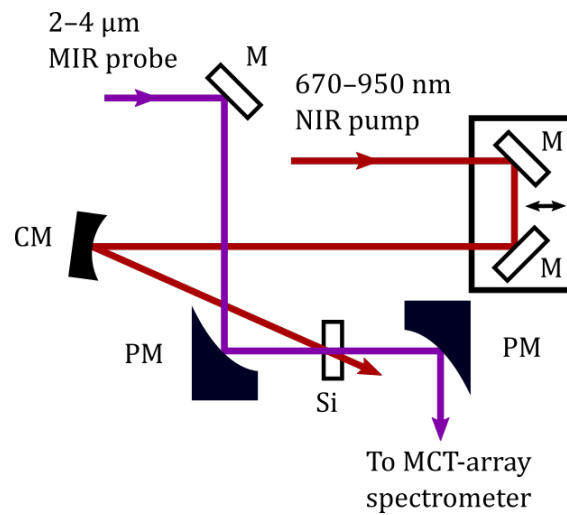


Figure 5.6: FROSt setup. M—mirror, CM—concave mirror, PM—parabolic mirror

is picked off before the 4f pulse shaper and compressed using a dispersion-compensating chirped mirror pair (DCMP175 Thorlabs). The pump spectrum and retrieved pulse intensity is shown in Fig. 5.7. The measured FWHM pulse duration is 13.2 fs, with a transform-limited pulse duration of 7.2 fs. The pump beam is focused to the Si sample using a 25-cm concave mirror. However, the sample is positioned before the focal plane such that the pump beam  $1/e^2$  diameter is 265  $\mu\text{m}$  and the average fluence using 90 mW of pump power is 16  $\text{mJ}/\text{cm}^2$ . This fluence results in near-complete absorption of the probe pulse

<sup>2</sup>This algorithm is discussed in Appendix B.

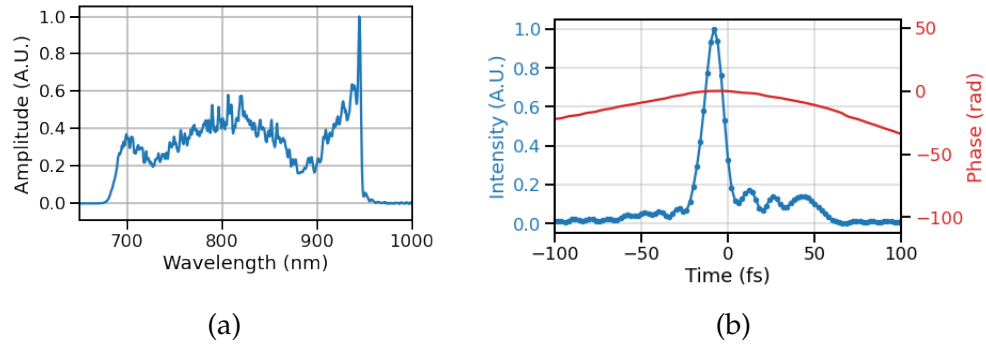


Figure 5.7: (a) Spectrum and (b) pulse intensity of NIR pump used for FROSt. This NIR pulse is compressed using a pair of chirped mirrors instead of the 4f pulse shaper.

without exceeding the damage threshold of the Si sample, which was determined to be  $66 \text{ mJ/cm}^2$  for our pump parameters. The MIR probe must be focused to a beam diameter smaller than that of the NIR pump to ensure uniform absorption and to mitigate walk off resulting from the movement of the translation stage. The probe beam is focused to a  $1/e^2$  beam diameter of  $44 \mu\text{m}$  using a 2-inch off-axis parabolic mirror. Another 2-inch off-axis parabolic mirror collimates the beam, which is then measured with a 2D MCT-array monochromator.

The measured and retrieved FROSt traces for the MIR pulse with one pass through the  $1.65\text{-}\mu\text{m}$  longpass filter are shown in Fig. 5.8. The retrieved pulse

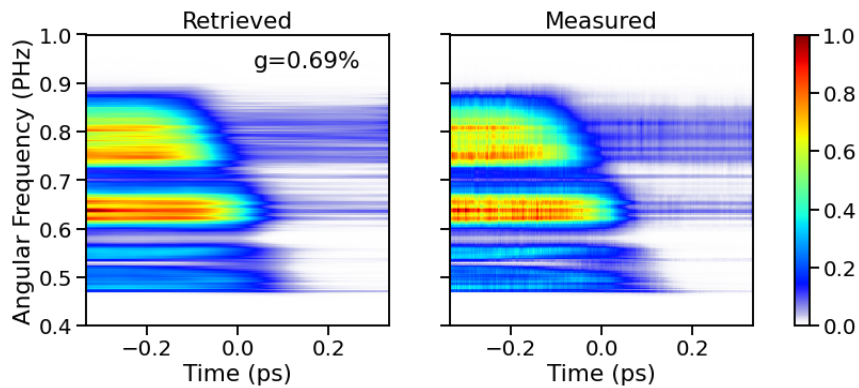


Figure 5.8: Measured (right) and retrieved (left) FROSt traces with one pass through the longpass filter. The retrieved trace error is 0.69%.

intensity, phase, and switch function are shown in Fig. 5.9a. The corresponding spectral intensity and phase are shown in Fig. 5.9b. The measured and retrieved

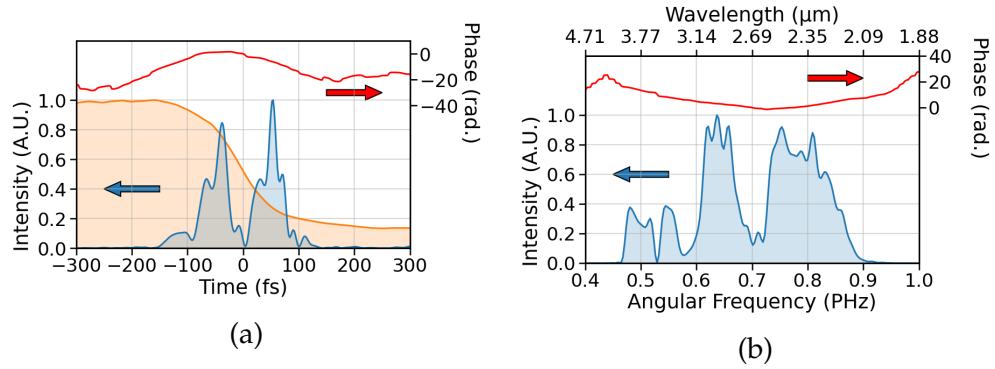


Figure 5.9: (a) Retrieved probe pulse intensity (blue) and probe phase (red) of the MIR pulse using FROSt with one pass through the longpass filter. The corresponding switch function is shown in orange. (b) Retrieved spectral intensity (blue) and phase (red).

FROSt traces for the MIR pulse with two passes through the 1.65- $\mu\text{m}$  longpass filter are shown in Fig. 5.10. The retrieved pulse intensity, phase, and switch

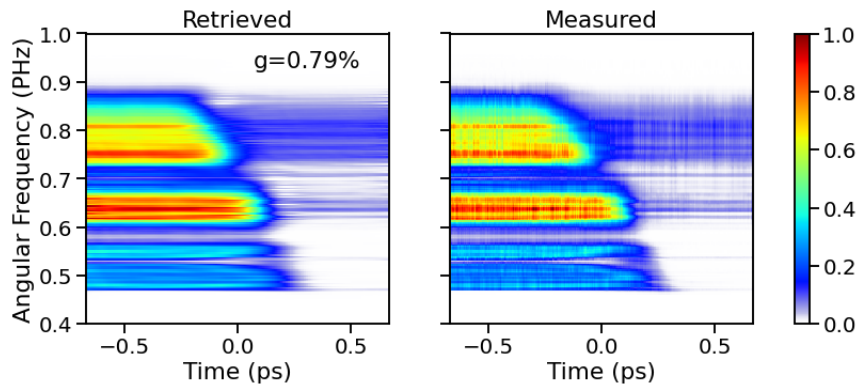


Figure 5.10: Measured (right) and retrieved (left) FROSt traces with two passes through the longpass filter. The retrieved trace error is 0.79%.

function are shown in Fig. 5.11a. The retrieved spectral intensity and phase are shown in Fig. 5.11b. From these measurements, we have the spectral phases  $\phi_{\text{MIR}}^{(1)}$  and  $\phi_{\text{MIR}}^{(2)}$  of the MIR pulse with one and two passes through the longpass filter.

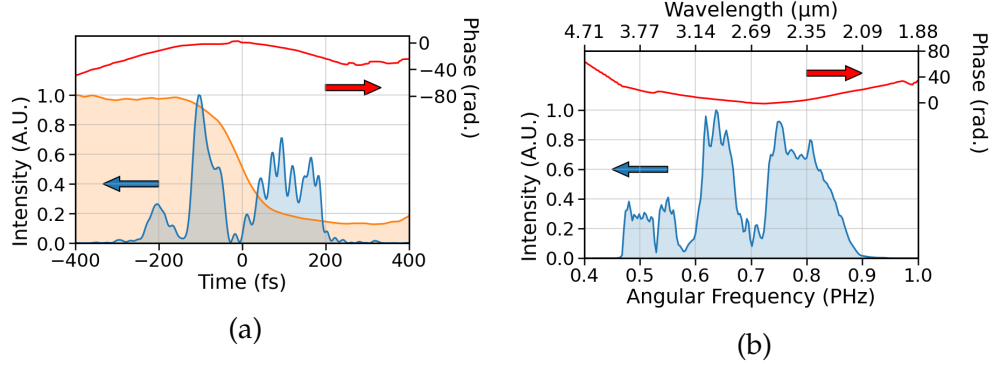


Figure 5.11: (a) Retrieved pulse intensity (blue) and phase (red) of the MIR pulse using FROSt with two passes through the longpass filter. The retrieved switch function is shown in orange. (b) Retrieved spectral intensity (blue) and phase (red).

## 5.4 RESULTS AND DISCUSSION

The phase imparted by the dispersion-managed ADFG device is calculated using Eq. 5.6. We have the first three terms on the right-hand side but must calculate the phases imparted by the additional optics,  $\phi_{BS}$  and  $\phi_{DM}$ . These are calculated using

$$\phi(\omega) = \frac{\omega n_{FS}(\omega)}{c} t_{\text{eff}} \quad (5.7)$$

where  $\omega$  is the angular frequency,  $n_{FS}(\omega)$  is the refractive index of fused silica [82],  $c$  is the speed of light, and  $t_{\text{eff}}$  is the effective path length in the material. For both optics, the effective path length is calculated according to

$$t_{\text{eff}} = \frac{t}{\cos\left(\sin^{-1}\left(\frac{1}{n_{FS}(\omega_0)} \sin(\theta_0)\right)\right)} \quad (5.8)$$

where  $t$  is the substrate thickness,  $\omega_0$  is the carrier frequency of the NIR pulse, and  $\theta_0$  is the incident angle which is assumed to be  $45^\circ$ .

The calculated spectral phase  $\phi_D$  imparted by the dispersion-managed device is shown in Fig. 5.12. Note, the jump around 0.53 PHz is due to the low spectral amplitude measured in the MIR spectrum (see Fig. 5.9b), which is due

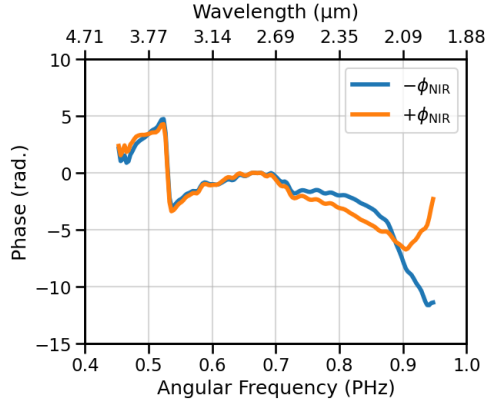


Figure 5.12: Calculated spectral phase  $\phi_D$  imparted by the dispersive-managed adiabatic frequency conversion device.

to a parasitic nonlinear process in the adiabatic frequency conversion device. From this phase, we calculated the imparted group delay using

$$GD = \frac{d\phi_D}{d\omega}. \quad (5.9)$$

The measured group delay imparted by our dispersion-managed device is plotted in Fig. 5.13a alongside the analytic group delay imparted by the adiabatic conversion device used in Krogen et al. [69] which did not employ intrinsic dispersion management. The group delay from our device varies by <200 fs

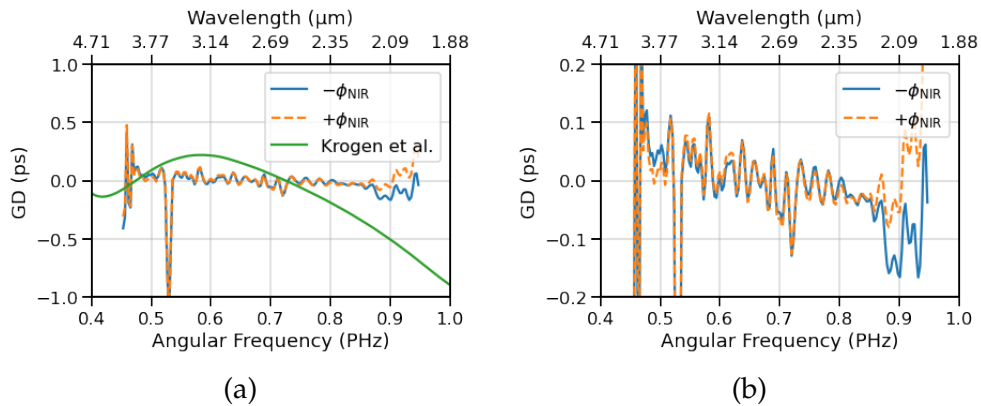


Figure 5.13: Group delay imparted by the dispersion-managed adiabatic frequency conversion device. (a) Comparison with the analytic group delay from the device in Ref. [69]. (b) Zoomed plot showing the group delay from our device.

across the target bandwidth (2–4  $\mu\text{m}$ ), while the group delay from the device in Ref. [69] varies by  $\sim 750$  fs over the same range. On average, the group delay from our device is fairly linear, meaning that the residual dispersion is mostly group delay dispersion. We estimate a residual group delay dispersion of  $-210$   $\text{fs}^2$  using  $+\phi_{\text{NIR}}$  or  $-307$   $\text{fs}^2$  using  $-\phi_{\text{MIR}}$  by applying a linear fit over the target range.

The calculated output MIR pulse using the spectral phase  $\phi_D$  imparted by our device is shown in Fig. 5.14. Notably, the residual dispersion is significant

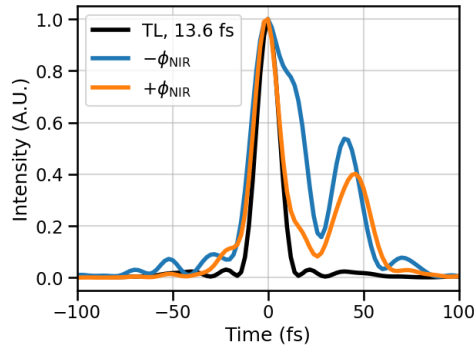


Figure 5.14: Calculated output MIR pulses with phase imparted by the dispersion-managed adiabatic frequency converter. The calculated transform-limited pulse (black) has a FWHM pulse duration of 13.6 fs.

for our octave-spanning pulses, but we could use a small amount of material or our pulse shapers to compensate. More measurements are being conducted to investigate the source of dispersion which could be due the manufacturing uncertainty in the device length. Additionally, dispersion tuning may be achieved using the temperature of the device and the angle of the incident light.

With intrinsic dispersion management, the adiabatic conversion stages are engineered to have a flat group-delay profile with higher-order dispersion terms ( $\geq 2$ ) equal to zero. Thus, the output pulse, either in the visible or MIR, inherits the phase profile of the incident light up to an overall group delay. Notably, the

dispersion-managed adiabatic frequency conversion devices provide a route to directly convert a transform-limited NIR pulse to a transform-limited visible or MIR pulse without the need of additional dispersion management, especially in spectral regions where options for dispersion compensation are limited and/or lossy. The dispersion-engineered ASFG stage, described in Sec. 4.2, producing visible pulses is currently not employed but can be easily implemented by swapping with the ADFG crystal or by building an identical setup allowing concurrent visible, NIR, and MIR femtosecond pulses.

## CHAPTER 6

### FREQUENCY HOMOGENIZATION

Optical frequency conversion provides a means of translating available laser frequencies to other less-accessible regions, enabling tunable and multicolor laser systems for applications including chemical sensing, spectroscopy, optical imaging, and much more. Moreover, frequency conversion has been shown to preserve the quantum nature of light [70]. This ability to connect disparate regions of the electromagnetic spectrum, while preserving quantum states, positions optical frequency conversion as a key tool in connecting quantum technologies that compose the foundations of quantum networks and communication. Thus, single photon sources (detectors) that emit (detect) throughout the visible and NIR [36] can be implemented in the same quantum infrastructure. Additionally, by converting the photons to telecommunication frequencies, quantum networks can take advantage of the low-loss telecommunication infrastructure for long-distance applications. To this end, various groups have made considerable advances, showing that visible photon sources can be down-converted to telecommunication bands [1, 27, 56, 78, 152] and that NIR photons can be upconverted for detection or integration with other quantum technologies [78, 106, 107].

One challenge facing the development of a robust quantum infrastructure is the availability of high-purity, indistinguishable single-photon sources and ensembles in the telecommunication bands. For example, solid-state quantum emitters such as quantum dots and nitrogen vacancy centers in diamond [71, 109, 119, 127] emit in the visible region and suffer from inhomogeneous spectral broadening which increases the spectral distinguishability and dimin-

ishes the purity of the source. Frequency translation using active feed-forward spectral multiplexing [49, 151] and quantum frequency conversion using cross phase modulation [96], three-wave mixing in periodically-poled waveguides [6, 136, 145], and four-wave mixing in nanophotonic chips [126] have been used to address the spectral distinguishability of disparate photon sources. Spectral multiplexing techniques can operate on single photon sources in the telecommunication band but require heralding for feed-forward control and typically use electro-optic modulators resulting in frequency shifts of  $<20$  GHz ( $< 0.16$  nm at 1550 nm). Meanwhile, frequency conversion techniques allow larger shifts in frequency, albeit not always to telecommunication wavelengths. Ates et al. [6] used frequency upconversion in a periodically-poled lithium niobate waveguide to convert two spectrally disparate InAs/GaAs quantum dot sources to 600 nm. Weber et al. [145] converted the output of two narrowband, spectrally distinct quantum emitters to a telecommunication band using two narrowband frequency conversion stages. These stages required independent temperature control and separate, tunable pump laser sources.

We propose a technique to convert an inhomogeneous emission spectrum from a single-photon emitter to a narrow, homogeneous linewidth at  $1.55$   $\mu\text{m}$ , simultaneously increasing the spectral homogeneity and translating the frequency to a telecommunication band. We use a distinct phase-matching function (PMF) that can be achieved in specific birefringent materials and periodically-poled waveguides. The required PMF results when the group velocity of the input single photon is matched with that of the pump field. The spectral homogeneity of the output is determined by the purity of the transfer function associated with the DFG process in analogy to the purity of the joint spectral amplitude (JSA) of a bi-photon state produced from spontaneous para-

metric downconversion (SPDC). The chapter is organized as follows: Sec. 6.1 reviews the purity calculation of the JSA of a bi-photon source using Schmidt decomposition; Sec. 6.2 introduces the analogy to a classical DFG process and details the calculation of the coupling amplitude connecting the input and output spectral distributions; and Sec. 6.3 reviews suitable devices and numerical simulations.

## 6.1 SCHMIDT DECOMPOSITION OF JSA

The purity of a bi-photon state generated via SPDC can be quantified using Schmidt decomposition of the JSA which captures the spectral-temporal properties of the generated photons [48, 158]. In SPDC, a bright pump source of angular frequency  $\omega_p$  is used to generate a pair of photons, the signal and the idler, of angular frequencies  $\omega_s$  and  $\omega_i$  respectively, satisfying  $\omega_p = \omega_s + \omega_i$ . The generated state, assuming single-mode emission from a weakly pumped waveguide<sup>1</sup>, can be described by

$$|\psi_{\text{PDC}}\rangle = C \int d\omega_s d\omega_i f(\omega_s, \omega_i) \hat{a}^\dagger(\omega_s) \hat{b}^\dagger(\omega_i) |0\rangle, \quad (6.1)$$

where  $C$  is a constant including the second-order nonlinear susceptibility and pump power,  $\hat{a}^\dagger(\omega_s)$  and  $\hat{b}^\dagger(\omega_i)$  are creation operators for the signal and idler photons respectively, h.c. is the Hermitian conjugate, and  $f(\omega_s, \omega_i)$  is the JSA normalized such that  $\int d\omega_s d\omega_i |f(\omega_s, \omega_i)|^2 = 1$ . The JSA is characterized by the pump spectral amplitude,  $\alpha(\omega_s + \omega_i)$ , and the phase-matching function (PMF),  $\phi(\omega_s, \omega_i)$ , such that

$$f(\omega_s, \omega_i) = \alpha(\omega_s + \omega_i) \phi(\omega_s, \omega_i). \quad (6.2)$$

---

<sup>1</sup>Weakly pumped indicates that Fock states of photon number  $>2$  in the output are ignored.

By engineering the pump spectral amplitude and the PMF, the purity of the output state can be controlled. If a strong correlation exists between the signal and idler angular frequencies, the output state is highly frequency entangled, and the JSA cannot be expressed as a product of two functions,  $g(\omega_s)$  and  $h(\omega_i)$ , that depend only on the signal angular frequency and the idler angular frequency, respectively. However, if no correlation exists, the output state can be expressed as a product of  $g(\omega_s)$  and  $h(\omega_i)$ . In this case, the JSA is separable and pure. This is the basis of the purity analysis using Schmidt decomposition.

Using Schmidt decomposition [75, 101], the JSA can be expressed as a sum of orthogonal modes such that

$$f(\omega_s, \omega_i) = \sum_n \sqrt{\lambda_n} g_n(\omega_s) h_n(\omega_i), \quad (6.3)$$

where  $\{g_n\}$  and  $\{h_n\}$  are sets of orthonormal basis functions for the signal and idler spectral distributions respectively and  $\sqrt{\lambda_n}$  is the Schmidt coefficient corresponding to the  $n^{\text{th}}$  mode in the summation. The Schmidt coefficients,  $\sqrt{\lambda_n}$ , satisfy the normalization condition  $\sum_n \lambda_n = 1$ . The Schmidt Number defined as

$$K = \frac{1}{\sum_n \lambda_n^2} \quad (6.4)$$

describes the effective number of populated modes [74]. Finally, the purity is defined as the inverse of the Schmidt number,  $P = 1/K$ .

The Schmidt decomposition of a JSA is pictorially represented in Fig. 6.1a. The JSA is decomposed into a sum of orthogonal modes weighted by the Schmidt coefficients,  $\sqrt{\lambda_n}$ . The pump spectral amplitude and the PMF are assumed to have Gaussian distributions with FWHM values indicated by grey dashed and solid lines respectively. The first three modes are shown on the right-hand side of Fig. 6.1a. Figure 6.1b shows the square of the Schmidt coeffi-

coefficients for the first 5 modes. The Schmidt number is 1.76, and the purity is 0.57.

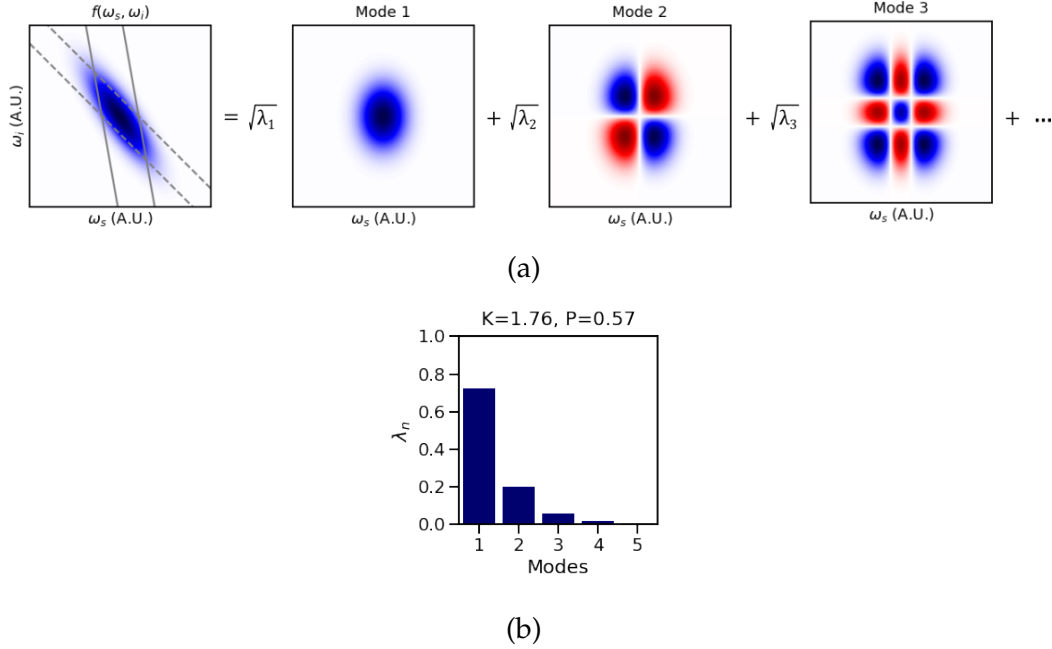


Figure 6.1: Schmidt decomposition of an example JSA for SPDC. (a) Pictorial representation of the decomposition. The JSA is constructed from a Gaussian pump spectral amplitude and PMF. The FWHM of the functions are shown as the grey dashed and solid lines respectively. The first three orthogonal modes are shown. (b) Square of the Schmidt coefficients for the first 5 modes. The JSA has a Schmidt number  $K = 1.76$  and a purity  $P = 0.57$ .

## 6.2 DFG ANALOGY AND COUPLING AMPLITUDE

In analogy with the JSA of a bi-photon state from SPDC, a coupling amplitude between the input and output fields in a DFG process can be constructed. Consider a classical device that downconverts an input field of angular frequency  $\omega_{\text{in}}$  to an output field of angular frequency  $\omega_{\text{out}}$  using a strong pump field of angular frequency  $\omega_p$  such that  $\omega_{\text{in}} = \omega_p + \omega_{\text{out}}$ . The dynamics are described by

the set of coupled wave equations given in Eq. 2.5. For the DFG process, the subscripts  $\{p, s, i\}$  are replaced with  $\{\text{in}, p, \text{out}\}$ .

In the low-conversion regime (i.e.  $\frac{dA_{\text{in}}}{dz} = 0$ ) and with a constant pump (i.e.  $\frac{dA_p}{dz} = 0$ ), Eq. 2.5a can be solved by integrating over the interaction length,  $L$ , such that

$$A_{\text{out}} = -j \frac{\omega_{\text{out}} d_{\text{eff}}}{n_{\text{out}} c_0} A_p^* A_{\text{in}} \int_0^L e^{-j\Delta k z} dz. \quad (6.5)$$

Eq. 6.5 can be written in terms of a coupling amplitude  $f(\omega_{\text{in}}, \omega_{\text{out}})$  as

$$A_{\text{out}} = f(\omega_{\text{in}}, \omega_{\text{out}}) A_{\text{in}}, \quad (6.6)$$

where

$$f(\omega_{\text{in}}, \omega_{\text{out}}) = -j \frac{\omega_{\text{out}} d_{\text{eff}}}{n_{\text{out}} c_0} A_p^* \int_0^L e^{-j\Delta k z} dz. \quad (6.7)$$

Using the syntax of the JSA in Eq. 6.2,

$$f(\omega_{\text{in}}, \omega_{\text{out}}) = -j \frac{\omega_{\text{out}} d_{\text{eff}}}{n_{\text{out}} c_0} \alpha^*(\omega_{\text{in}} - \omega_{\text{out}}) \phi(\omega_{\text{in}}, \omega_{\text{out}}), \quad (6.8)$$

where  $\alpha(\omega_{\text{in}} - \omega_{\text{out}}) = A_p$  is the pump spectral amplitude and  $\phi(\omega_{\text{in}}, \omega_{\text{out}}) = \int_0^L e^{-j\Delta k z} dz$  is the PMF.

Our goal is *frequency homogenization*—to convert a broad, inhomogeneous input spectral distribution to a narrow, homogeneous output spectral distribution. Thus, the desired coupling amplitude is a long, narrow ridge lying parallel to the axis corresponding to the input angular frequency. From Eq. 6.8, there are two main contributions to the coupling amplitude,  $f(\omega_{\text{in}}, \omega_{\text{out}})$ : the pump spectral amplitude and the PMF. First, the pump spectral amplitude must be broad enough to satisfy the energy conservation required to convert a broad input bandwidth to a narrow output bandwidth. Moreover, the pump spectral amplitude will always be oriented along the line dictated by energy conservation of the carrier angular frequencies,  $\bar{\omega}_{\text{out}} = \bar{\omega}_{\text{in}} - \bar{\omega}_p$ . Second, the PMF must allow

efficient conversion of the broad input to a single output frequency. The contribution of the PMF to the coupling amplitude can be determined by expanding the wavenumbers to first order around the carrier frequencies and solving for the wave-vector mismatch. The expansion of the wavenumbers gives

$$k_j(\omega_j) = k_j(\bar{\omega}_j) + v_j^{-1}\Omega_j, \quad (6.9)$$

where  $v_j^{-1} = \left. \frac{\partial k_j}{\partial \omega_j} \right|_{\bar{\omega}_j}$  is the inverse of the group velocity evaluated at the carrier angular frequency  $\bar{\omega}_j$  and  $\Omega_j = \omega_j - \bar{\omega}_j$  is the relative angular frequency. Solving for the wave-vector mismatch gives

$$\begin{aligned} \Delta k &= k_{\text{in}} - k_p - k_{\text{out}} \\ &= k_{\text{in}}(\bar{\omega}_{\text{in}}) + v_{\text{in}}^{-1}\Omega_{\text{in}} - k_p(\bar{\omega}_p) - v_p^{-1}\Omega_p - k_{\text{out}}(\bar{\omega}_{\text{out}}) - v_{\text{out}}^{-1}\Omega_{\text{out}}. \end{aligned} \quad (6.10)$$

Using  $\Omega_p = \Omega_{\text{in}} - \Omega_{\text{out}}$ , Eq. 6.10 can be simplified to

$$\Delta k = \Delta k_0 + (v_{\text{in}}^{-1} - v_p^{-1})\Omega_{\text{in}} + (v_p^{-1} - v_{\text{out}}^{-1})\Omega_{\text{out}}, \quad (6.11)$$

where  $\Delta k_0 = k_{\text{in}}(\bar{\omega}_{\text{in}}) - k_p(\bar{\omega}_p) - k_{\text{out}}(\bar{\omega}_{\text{out}})$ . When  $\Delta k_0 = 0$ , the orientation of the PMF can be determined by assuming  $\Delta k = 0$  and solving for the output angular frequency  $\Omega_{\text{out}}$  as a function of the input angular frequency  $\Omega_{\text{in}}$ . This gives

$$\Omega_{\text{out}} = \frac{v_{\text{in}}^{-1} - v_p^{-1}}{v_p^{-1} - v_{\text{out}}^{-1}}\Omega_{\text{in}}. \quad (6.12)$$

The angle,  $\Theta$ , that the PMF makes with respect to the axis corresponding to the input angular frequency is

$$\Theta = \tan^{-1} \left( \frac{v_{\text{in}}^{-1} - v_p^{-1}}{v_p^{-1} - v_{\text{out}}^{-1}} \right). \quad (6.13)$$

Thus, the PMF is parallel to the input angular frequency axis ( $\Theta = 0$ ) when the group velocity of the input field is equal to the group velocity of the pump

field<sup>2</sup>,  $v_{\text{in}} = v_{\text{p}}$ .

The group velocities of the pump and input fields are equal for the crystals, wavelengths, and phase-matching conditions shown in Table 6.1. Note, this list is not exhaustive and only considers bulk, unpoled crystals with an output wavelength of 1.55  $\mu\text{m}$ . Waveguide dispersion and quasi-phase matching may allow the group-velocity matching condition to be met for other materials and wavelengths.

### 6.3 DEVICE CALCULATIONS AND SIMULATIONS

Two devices are proposed and analyzed: (1) a 12.5-mm BBO crystal and (2) a 2-mm, quasi-phase-matched Rb:KTP waveguide. For each device, the target output wavelength is  $\lambda_{\text{out}}=1.55 \mu\text{m}$ ; the purity of the coupling amplitude is calculated using Schmidt decomposition; and the performance is further analyzed using a split-step Fourier pulse propagation simulation. Simulations are performed for several narrowband input spectral intensities with different carrier frequencies spaced around the group-velocity-matched input frequency. The pump spectral intensity is kept fixed for all simulations of a single device. The degree of homogenization is calculated using the normalized intensity spectral overlap between the output spectral intensities,  $I_{\text{out}}$ , and the group-velocity-

---

<sup>2</sup>The group velocity requirements are similar to those for broadband OPA. However, for the OPA process, a quasi-monochromatic pump is used to amplify a broadband signal and generate a broadband idler. In frequency homogenization, a broadband pump is used to transfer a broadband input to a quasi-monochromatic output. The group velocities of the broadband input and pump fields must be equal.

Crystal	$\lambda_{\text{in}}$ (nm)	$\lambda_{\text{out}}$ (nm)	$\lambda_p$ (nm)	$\theta$ ( $^\circ$ )	$\phi$ ( $^\circ$ )	PP	$n$ Ref.
BBO	908 (e)	1550 (o)	2192.2 (e)	26.7	—	—	[137]
BiBO	705 (o)	1550 (o)	1293.2 (e)	44	0	XZ	[140]
BiBO	969 (o)	1550 (e)	2585.1 (e)	41.3	0	XZ	[140]
BiBO	885 (o)	1550 (e)	2062.8 (e)	34.9	—	XZ	[140]
LBO	640 (o)	1550 (e)	1090.1 (e)	87.7	0	XZ	[65]
LBO	520 (e)	1550 (o)	782.5 (o)	22.3	0	XZ	[65]
LBO	840 (o)	1550 (e)	1833.8 (o)	15.4	90	YZ	[65]
LiIO <sub>3</sub>	815 (e)	1550 (e)	1718.7 (o)	30.6	—	—	[63]
KTP	745 (o)	1550 (o)	1434.5 (e)	53	0	XZ	[66]
KTP	735 (o)	1550 (o)	1397.9 (e)	44	90	YZ	[66]
Mg:LNB	961 (e)	1550 (o)	2528.9 (o)	43	—	—	[153]

Table 6.1: Crystals, wavelengths, and phase-matching parameters that result in group-velocity matching between the input and pump fields and an output wavelength of 1.55  $\mu\text{m}$ . The input, output, and pump wavelengths are  $\lambda_{\text{in}}$ ,  $\lambda_{\text{out}}$ , and  $\lambda_p$ , respectively. The polarization of each field is listed as either e for extraordinary or o for ordinary, where the extraordinary polarization lies in the plane created by the wave vector and the crystal axis for uniaxial crystals or in the principal plane (PP) for biaxial crystals. For uniaxial crystals, the phase-matching angle  $\theta$  defines the angle between the crystal axis and the wave vector. For biaxial crystals, the phase-matching angles  $\theta$  and  $\phi$  define the direction of the wave vector from the crystal Z axis to the XY plane and from the crystal X axis to the crystal Y axis, where the crystal axes are defined such that  $n_x < n_y < n_z$ . The phase-matching angle  $\phi$  and the principal plane are only listed for biaxial crystals.

matched output spectral intensity,  $I_{\text{out},0}$ ,

$$S = \frac{\int d\omega' d\omega I_{\text{out},0}(\omega') I_{\text{out}}(\omega)}{\sqrt{\int d\omega' I_{\text{out},0}(\omega')^2 \int d\omega I_{\text{out}}(\omega)^2}}. \quad (6.14)$$

### 6.3.1 BBO Free-Space Device

For a target output wavelength of 1.55  $\mu\text{m}$ , the input and pump group velocities are matched for  $\lambda_{\text{in}}=0.908 \mu\text{m}$  and  $\lambda_p=2.1922 \mu\text{m}$  in BBO. Corresponding to the first row of Table 6.1, the polarizations of the input, output, and pump fields

are (e), (o), and (e) respectively, and the phase-matching angle is  $26.7^\circ$ . The Sellmeier equations from Tamosauskas et al. [137] are used for the calculation. The coupling amplitude, shown in Fig. 6.2, is calculated according to Eq. 6.8, given a pump spectral intensity with a 100-nm FWHM bandwidth centered at 2192.2 nm. The absolute values of the PMF, pump spectral amplitude  $A_p$ , and coupling amplitude  $f$  are shown in Fig. 6.2. The Schmidt number is 1.114, and the purity is 0.898.

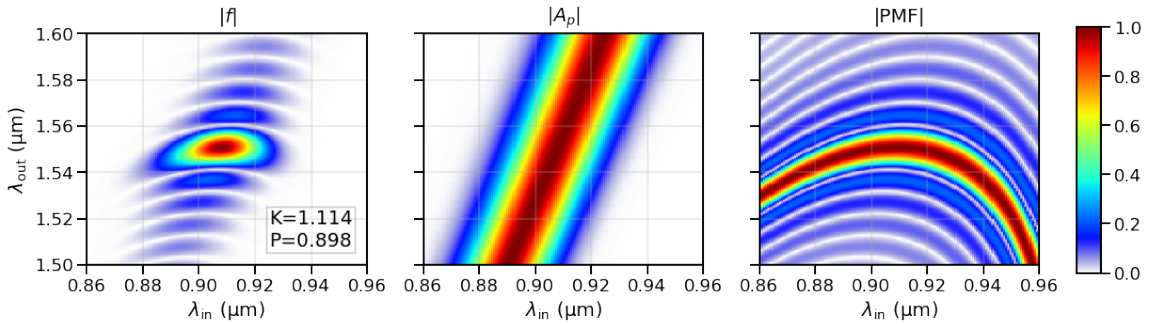


Figure 6.2: Absolute value of the coupling amplitude  $f$  calculated from the pump spectral amplitude  $A_p$  and the PMF. The pump spectral intensity is assumed to have a 100-nm FWHM bandwidth centered at 2192.2 nm. All plots are normalized to the maximum values. The Schmidt number and purity of the coupling amplitude are 1.114 and 0.898 respectively.

Split-step Fourier pulse propagation simulations are performed to verify the homogenization capabilities of the device. For all simulations, the pump pulse parameters are kept fixed while the center wavelength of the input pulse,  $\lambda_{in,0}$ , is varied. The pump pulse is assumed to have a 100-nm FWHM bandwidth centered at 2192.2 nm. The pump beam size, intensity, and energy are determined by the spatial walk off, conversion rate, and crystal length. The Poynting vector walk off of the pump and input fields is  $\sim 62.5$  mrad corresponding to 720  $\mu\text{m}$  of spatial walk off after the 12.5-mm crystal. To avoid significant distortion to the generated output, the pump beam radius is assumed to be 0.775  $\mu\text{m}$  at half maximum. To achieve the target peak pump intensity of 0.5  $\text{GW}/\text{cm}^2$ , a pulse

energy of 1  $\mu\text{J}$  is required. The input pulse is assumed to have 0.1-nm FWHM spectral bandwidth corresponding to a transform-limited pulse durations of  $\sim 5$  ps. The input pulse energy is set equal to that of a single photon,  $E = \hbar\omega_{\text{in}}$ , where  $\hbar$  is Planck's constant divided by  $2\pi$ . The input beam size is assumed to be equal to the pump beam size. The resulting output spectra are shown in Fig. 6.3.

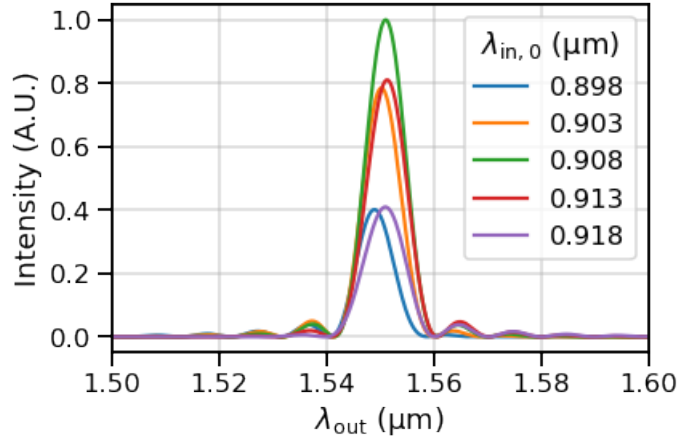


Figure 6.3: Output spectra from split-step Fourier pulse propagation simulations for the 12.5-mm BBO crystal. The input center wavelength,  $\lambda_{\text{in},0}$ , is varied about the group-velocity matched wavelength.

The spectral overlap integral from Eq. 6.14 is used to quantify the degree of homogenization. The normalized overlap integrals between the output spectrum generated by the input field with a center wavelength of  $\lambda_{\text{in},0} = 0.908 \mu\text{m}$  and output spectra generated from other input fields are plotted in Fig. 6.4. The open circles show the results of the pulse propagation simulations assuming a 50-nm FWHM pump spectrum (blue) and a 100-nm FWHM pump spectrum (orange). The solid lines show the normalized spectral overlap integrals calculated using the coupling amplitudes assuming a 50-nm FWHM pump spectrum (blue) and a 100-nm FWHM pump spectrum (orange). The black dashed line in Fig. 6.4 corresponds to an overlap integral  $S = 0.9$ . For the 50-nm (100-nm)

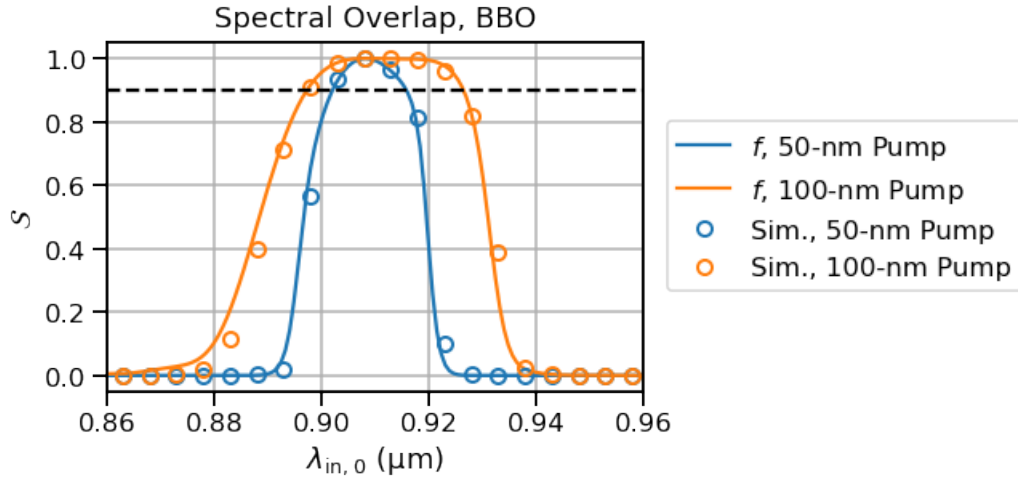


Figure 6.4: Normalized spectral overlap integrals between the output spectra generated from the input pulse with a center wavelength of  $0.908 \mu\text{m}$  and the input pulses with center wavelengths,  $\lambda_{in,0}$ . The solid lines show the overlap integral calculated from the coupling amplitudes, and the open circles show the overlap integral calculated from the pulse propagation simulations. The calculations are done for a 50-nm pump bandwidth (blue) and a 100-nm pump bandwidth (orange). The black dashed line marks an overlap integral of  $S = 0.9$ . For the 50-nm (100-nm) pump, 14 nm (29 nm) of the overlap integrals calculated using the coupling amplitude lie above this threshold.

pump, the overlap integral calculated using the coupling amplitude lies above this threshold for 14 nm (29 nm).

### 6.3.2 Rb:KTP Waveguide Device

Waveguide dispersion and quasi-phase matching can be used to tune the wavelengths at which the group-velocity condition and phase matching are satisfied for frequency homogenization. A rubidium-doped KTP (Rb:KTP) waveguide with a  $2\text{-}\mu\text{m}$  width,  $5\text{-}\mu\text{m}$  diffusion depth, and  $81.8\text{-}\mu\text{m}$  poling period satisfies these conditions for a  $0.605\text{-}\mu\text{m}$  input,  $0.992\text{-}\mu\text{m}$  pump, and  $1.55\text{-}\mu\text{m}$  output. Considering the temporal walk off of the output field and damage threshold of KTP, the device length is chosen to be 2 mm with a target pump intensity of

5 GW/cm<sup>2</sup>. The waveguide profile is shown in Fig. 6.5. The index profile is

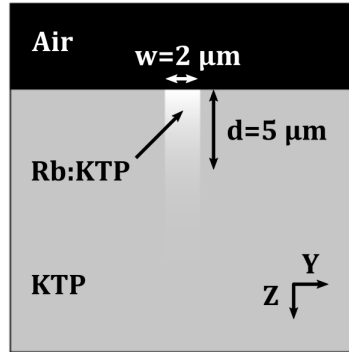


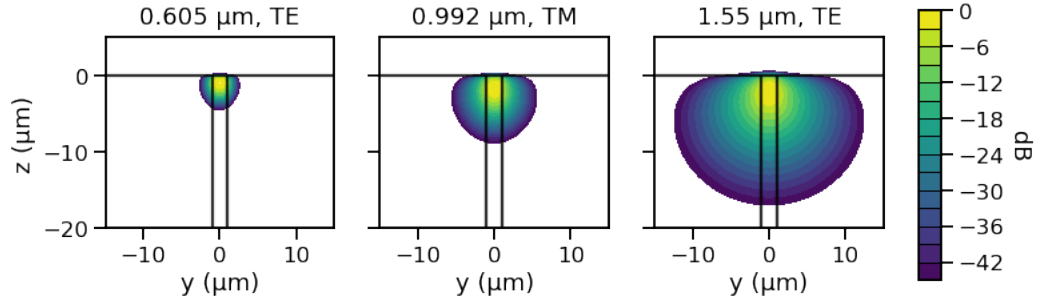
Figure 6.5: Rb:KTP waveguide profile. The waveguide has a 2- $\mu\text{m}$  width and a 5- $\mu\text{m}$  diffusion depth. The waveguide is constructed by diffusing rubidium ions into the KTP crystal along the crystal Z axis and poling the electric susceptibility along the crystal X axis. The composition of different areas and the crystal axes are labelled.

modeled as a complimentary error function

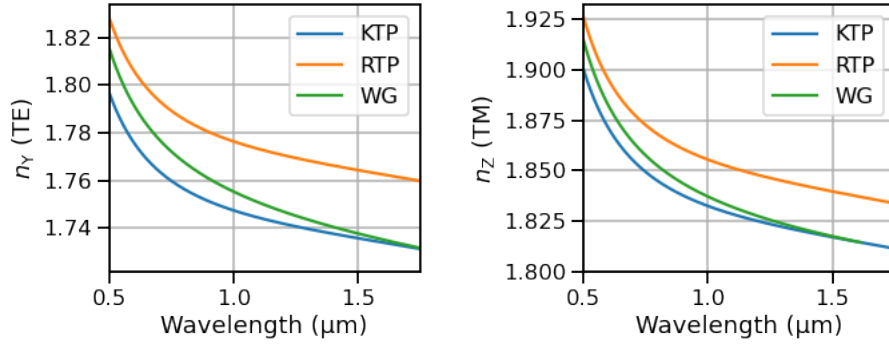
$$n_j^{\text{Rb:KTP}} = n_j^{\text{KTP}} + (n_j^{\text{RTP}} - n_j^{\text{KTP}}) \text{erfc}(z/d), \quad (6.15)$$

where  $j$  indicates the crystal axis,  $n^{\text{KTP}}$  and  $n^{\text{RTP}}$  are the refractive indices of KTP and RTP respectively,  $d$  is the diffusion depth, and  $z$  is the vertical distance measured from the crystal surface [125]. Due to restrictions from ferro-electric poling and rubidium diffusion, optical propagation is confined to the crystal X axis with the crystal Z and crystal Y axes corresponding to vertical (TM) and horizontal (TE) polarizations respectively. The polarizations of the input, output, and pump fields are Y, Y, and Z respectively. The effective refractive indices of the fundamental modes of the waveguide are calculated using the Finite-Difference Time-Domain (FDTD) method developed by Fallahkair et al. [38]. The field profiles and effective indices are shown in Fig. 6.6.

The purity of the coupling amplitude and the normalized spectral overlap



(a) The field intensity profile of the fundamental mode at  $\lambda_{\text{in}} = 0.605 \mu\text{m}$  (TE),  $\lambda_p = 0.992 \mu\text{m}$  (TM), and  $\lambda_{\text{out}} = 1.55 \mu\text{m}$  (TE).



(b) The refractive indices along the crystal Y and crystal Z axes of KTP (blue), RTP (orange), and the fundamental mode of the waveguide (green).

Figure 6.6: (a) Rb:KTP waveguide fundamental mode profile and (b) effective refractive indices.

integrals of the output spectra are calculated for the Rb:KTP waveguide. The coupling amplitude is shown in Fig. 6.7. The Schmidt number is 1.196, and the purity is 0.836.

Split-step Fourier pulse propagation simulations are used to verify the performance of the device. The output spectra obtained from input fields with various center wavelengths and 0.1-nm bandwidths are shown in Fig. 6.8. For these simulations, the pump center wavelength and bandwidth are kept fixed at 0.992  $\mu\text{m}$  and 100 nm, respectively. The normalized spectral overlap integrals calculated between the output spectrum from the group-velocity matched input and

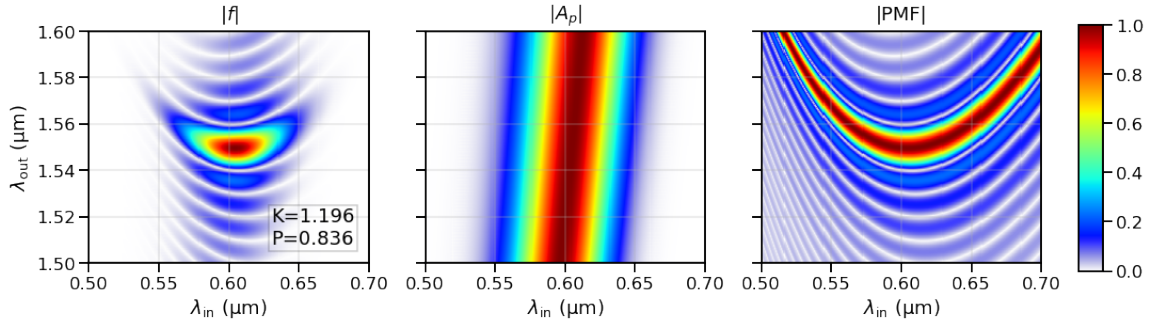


Figure 6.7: Absolute value of the coupling amplitude  $f$  calculated from the pump spectral amplitude  $A_p$  and the PMF. The pump spectral intensity is assumed to have a 100-nm FWHM bandwidth centered at 992 nm. All plots are normalized to the maximum values. The Schmidt number and purity of the coupling amplitude are 1.196 and 0.836 respectively.

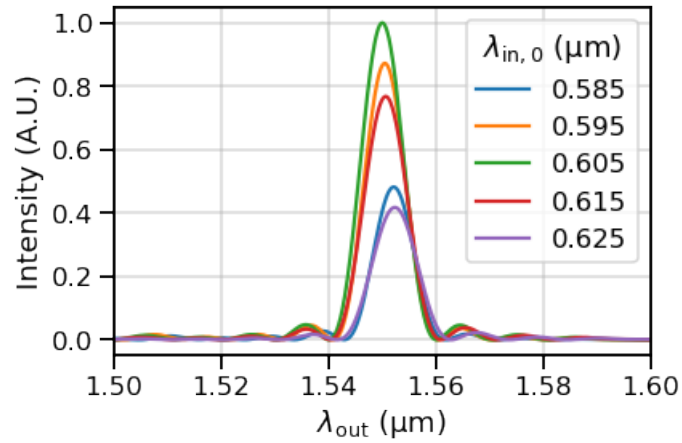


Figure 6.8: Output spectra calculated from split-step Fourier pulse propagation simulations for the 2-mm Rb:KTP waveguide. The input center wavelength,  $\lambda_{in,0}$ , is varied about the group-velocity matched wavelength.

the output spectra from other inputs is shown in Fig. 6.9. The results from the pulse propagation simulations (open circles) and from the coupling amplitude (solid lines) using a 50-nm bandwidth pump (blue) and a 100-nm bandwidth pump (orange) are compared.

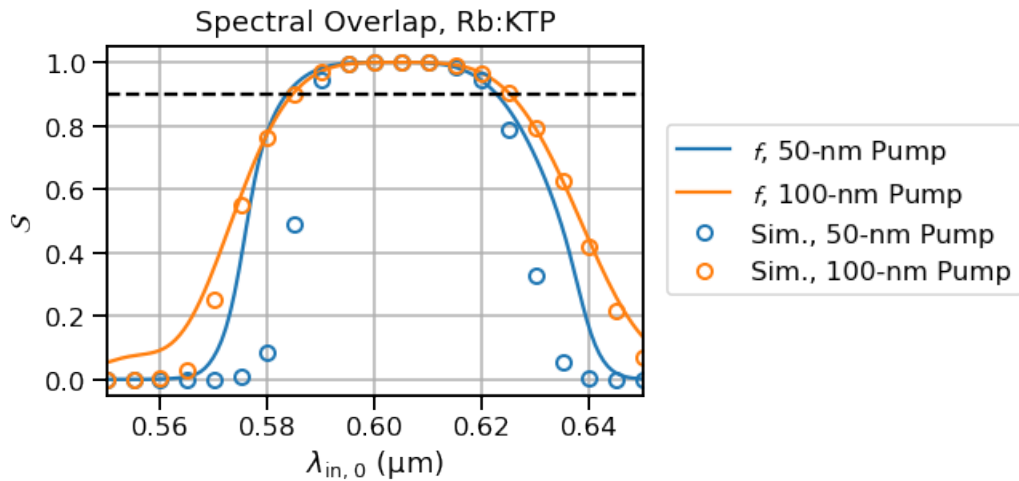


Figure 6.9: Normalized spectral overlap integrals between the output spectra generated from the input pulse with a center wavelength of  $0.605 \mu\text{m}$  and the input pulses with center wavelengths,  $\lambda_{in,0}$ . The solid lines show the overlap integral calculated from the coupling amplitudes, and the open circles show the overlap integral calculated from the pulse propagation simulations. The calculations are done for a 50-nm pump bandwidth (blue) and a 100-nm pump bandwidth (orange). The black dashed line marks an overlap integral of  $S = 0.9$ . For the 50-nm (100-nm) pump, 39.1 nm (40.7 nm) of the overlap integrals calculated using the coupling amplitude lie above this threshold.

## CHAPTER 7

### CONCLUSIONS AND FUTURE OUTLOOK

#### 7.1 SYSTEM REVIEW

A multicolor, 10-fs laser source has been developed from a high-repetition-rate, energetic NIR front end system, NIR 4f pulse shaping, and adiabatic frequency conversion. The NIR front end consists of a high-average-power, picosecond Yb:YAG Innoslab pump laser, a WLG stage, and a series of broadband OPCPA stages. The design of the pump system includes two exit ports: a low-power exit of 2  $\mu\text{J}$  with a FWHM pulse duration of  $\sim 900$  fs and a high-power exit of 18 mJ with a FWHM pulse duration of 3 ps. The pump system is ideally suited for driving a femtosecond NIR front end source as the short pulse from the low-power exit can be used to drive stable WLG while the picosecond pulse can be used to pump the nonlinear frequency conversion stages. A portion of the WL spectrum (650–950 nm) seeds the preamplifier OPCPA stage, which amplifies the pulse to  $\sim 10$   $\mu\text{J}$ . The pulse is then amplified to  $>100$   $\mu\text{J}$  in the power amplifier OPCPA stage, providing enough energy to split the NIR beam into several paths for various applications including seeding visible and MIR generation and providing pump and probe pulses for spectroscopy experiments. The bandwidth of the amplified pulse spans 670–950 nm supporting a 6.4-fs FWHM transform-limited pulse.

After the NIR front end, a pair of NIR 4f pulse shapers and adiabatic frequency conversion stages complete the 10-fs, multicolor laser architecture. The NIR 4f pulse shapers are used to control the amplitude and phase of the NIR pulses. The pulse shapers accommodate 171 nm of the NIR bandwidth and

compress the pulses to 10.5-fs FWHM. The NIR pulses are converted to the visible and MIR spectral ranges using adiabatic sum frequency conversion and adiabatic difference frequency conversion respectively. The conversion stages are designed to impart a constant group delay to the converted pulses—the higher-order dispersion ( $n \geq 2$ ) from the frequency-dependent conversion positions offsets that of the material dispersion of the device. Thus, a transform-limited NIR pulse is converted to a transform-limited MIR or visible pulse.

Our 10-fs, multicolor laser architecture provides several advantages for spectroscopy applications and ultrafast measurements. With the high-repetition rate and energies of the NIR front end afforded by the high-average-power pump laser, our multicolor laser source enables fast acquisition of multidimensional spectra when combined with the rapid update and acquisition rates of the NIR pulse shapers and modern array detectors. Additionally, the combination of NIR pulse shaping and adiabatic frequency conversion extends the rapid control of pulse sequences to multiple octaves of bandwidth, allowing the benefits of pulse-shaper-assisted multidimensional spectroscopy such as phase-cycling, pi-shift for background subtraction, and interferometrically stable control of pulse-pair delay in the visible, NIR, and MIR.

## 7.2 ULTRAFAST PUMP-PROBE SPECTROSCOPY

During nonadiabatic transitions where the Born-Oppenheimer approximation fails, molecular dynamics can occur within the span of a few hundred femtoseconds. These dynamics are mediated by electronic energy degeneracies in the reaction pathway of the excited molecule, known as conical intersections.

With  $\sim 10$ -fs pulses in the visible, NIR, and MIR and the pulse-to-pulse control afforded by the 4f pulse shapers, our 10-fs multicolor laser source is a powerful tool that can be used to explore these dynamics. We have planned several ultrafast spectroscopy experiments to benchmark the 10-fs multicolor laser source and to explore the ultrafast dynamics mediated by conical intersections.

### **Pauli Blocking**

First, we plan to perform a novel benchmark experiment using single-layer graphene (SLG). The primary thermalization events in SLG occur in  $< 100$  fs after photoexcitation. These events have been studied using ultrafast pump-probe spectroscopy [14] and time- and angle-resolved photoemission spectroscopy [47]. Despite the impressive time resolution, the pump-probe spectroscopy was limited to a temporal range dictated by the available probe wavelengths, 855–1030 nm. We propose performing the study with our NIR and MIR pulses, using the NIR pulses to excite the SLG and the NIR and MIR pulses to probe the dynamics, covering the spectral ranges 670–950 nm and 2000–4000 nm. As the carriers relax, the probe absorption is strongly suppressed at the frequency corresponding to the transition between the valence and conduction bands corresponding to the maximum of the electron distribution due to Pauli blocking. Thus, by using our octave-spanning femtosecond MIR pulses, the excited-carrier dynamics can be followed as they approach the Dirac point.

## Rhodopsin and Chrimson

Some biological reactions involve steps that occur on the femtosecond timescale. Often, these reactions are found in processes that hold significant importance to the function of an organism. For example, the torsional isomerization of the retinal chromophore, the primary event in dim-light vision in vertebrates and light-driven ion pumps in bacteria, takes place in less than a few hundred femtoseconds [116]. Interestingly, this reaction is mediated by a conical intersection. As such, there is particular interest in studying how the electronic energy topography affects the timescale and photoproduct yield of the reaction.

Polli et al. [104] have tracked the electronic wavepacket after photoexcitation of the retinal chromophore in rhodopsin using 10-fs, 500-nm pump pulses over an energy range corresponding to a visible wavelength range of 500–720 nm and a NIR wavelength range of 820–1020 nm. This probe range is sufficient to see a clear progression of the wavepacket toward and away from the conical intersection; however, the wavepacket is unaccounted for during a period of 50 fs in its last approach to and emergence from the intersection. We plan to extend this map of the energy topography using probe pulses covering 530–700 nm, 670–950 nm, 1.1–2.2  $\mu\text{m}$ , and 2–4  $\mu\text{m}$ .

Additionally, we plan to study the ultrafast dynamics of Chrimson, a red-light-activated channelrhodopsin from the algae *Chlamydomonas noctigama*, and other channelrhodopsin mutants. Naturally, channelrhodopsins mediate phototaxis and photophobic responses in algae, allowing it to respond to light. The isomerization of the retinal chromophore mediates ion pore formation and passive ion translocation, creating a light-induced ion conductance [10, 92, 93]. In optogenetics, channelrhodopsins are widely used to selectively control neuronal

activity because of their fast response and red-shifted activation spectrum which allows deeper penetration into tissue [13,28]. Further investigation of the structure and operation of these molecules would inform the development of mutants with faster kinetics and alternative activation wavelengths. For example, through mutation analysis Oda et al. [98] identified the structural features responsible for the red-shifted absorption and engineered a mutant with an activation wavelength shifted beyond 605 nm with accelerated dynamics. Measurements of the potential energy topography of these molecules may provide additional insights.

Previous pump-probe studies [115,129,141] have found branching ratios and time constants that are highly dependent on the mutant—each mutation having different steric electrostatic effects on the electronic structure. Moreover, these results depend on the specific experimental factors such as excitation wavelength and solvent. As such, Chrimson and other channelrhodopsin mutants comprise a rich resource of information regarding how the potential energy topography affects the dynamics. Using our multicolor source, the channelrhodopsin samples would be pumped using visible pulses (530–700 nm) generated using adiabatic sum frequency generation and probed using pulses covering the visible, NIR, and MIR (530–700 nm, 670–950 nm, 1.1–2.2  $\mu\text{m}$ , and 2–4  $\mu\text{m}$ ). Furthermore, we propose using 2D spectroscopy to investigate the affect of the pump wavelength on the kinetic energy of the excited-state wavepacket.

## DNA

The final molecule that we are interested in studying is DNA. When radiated with ultraviolet light, DNA is prone to photodamage resulting in photolesions

that cause skin cancer [4, 26, 103]. However, this reaction depends strongly on the conformation at the time of radiation and is often suppressed by other, ultrafast relaxation pathways [23, 87]. The relaxation time of DNA monomers has been measured below one picosecond—fast enough to suppress the formation of harmful photolesions—and is thought to be strongly affected by crossings with other excited states as well as the local potential energy topography, such as slopes and barriers. By studying the relaxation rates of the DNA monomers and various modifications including methylation, we aim to quantify the impact of these factors. Furthermore, by studying the differences in the transient absorption spectra of adenine monomers in solution and adenine bases in a double-stranded DNA environment, we can gain valuable insight into the effects of the local topography. Adenine monomers are predicted to have a *peaked* topography at the conical intersection (i.e. the point of degeneracy is a local minimum of the upper potential energy surface) and have fluorescence lifetimes of 0.1 ps and 0.3–0.5 ps [21, 22, 50]. Whereas, stacked Adenine bases in a double-stranded DNA environment have a *sloped* topography at the conical intersection (the point of degeneracy is not a local minimum of the upper potential energy surface) and have lifetimes of 0.39 ps and 4.3 ps [21, 22, 72].

For the DNA studies, pump-probe spectroscopy would be employed. A 260–300-nm UV pump pulse would be obtained from second harmonic generation of the 530–700 nm pulse from the adiabatic sum frequency generation. The pump pulse would be followed by a ~10-fs visible, NIR, or MIR probe pulse, allowing us to precisely track the transition energy over a broad range (0.45–4  $\mu\text{m}$ ) as a function of relaxation time.

### 7.3 QUANTUM COMMUNICATION

Frequency conversion plays a significant role in the development of ultrafast laser sources and their applications, allowing the generation and amplification of energetic, broadband pulses from high-power narrowband lasers. In quantum communication, frequency conversion has been shown to preserve the quantum nature of light and can be used to translate quantum states to different spectral regions [70], allowing the interconnect of quantum technologies that operate in disparate spectral regions. High purity and deterministic single-photon sources operating at telecommunication wavelengths would facilitate the development of a robust quantum communication infrastructure using existing telecommunication technology. A variety of deterministic, single-photon sources operate in the visible region of the electro-magnetic spectrum [36], including solid-state quantum emitters such as quantum dots and color centers. These technologies suffer from inhomogeneous spectral broadening which decreases the purity of the quantum state. Frequency translation using a narrowband pump preserves the spectral distinguishability—however, we propose using a broadband pump and a group-velocity matched phase-matching function to simultaneously translate the frequency to the telecommunication band and decrease the spectral distinguishability.

Two frequency homogenization devices are proposed and simulated: a 12.5-mm BBO crystal and a 2-mm Rb:KTP waveguide. To evaluate performance, the purity of the coupling amplitude and the spectral homogeneity of the output spectra are calculated. Furthermore, the devices are simulated using split-step Fourier pulse propagation to capture the temporal dynamics and confirm the spectral homogeneity of the output spectra. The BBO device converts an inho-

mogeneous distribution of input spectra around  $\lambda_{\text{in}} = 0.908 \mu\text{m}$  to a homogeneous output spectrum at  $\lambda_{\text{out}} = 1.55 \mu\text{m}$ . Using a 100-nm bandwidth pump centered at  $\lambda_p = 2.192 \mu\text{m}$ , the normalized spectral overlap is above 0.9 for a 29-nm range of input center wavelengths. The Rb:KTP waveguide converts an inhomogeneous distribution of input spectra around  $\lambda_{\text{in}} = 0.605 \mu\text{m}$  to a homogeneous output spectrum at  $\lambda_{\text{out}} = 1.55 \mu\text{m}$ . Using a 100-nm bandwidth pump centered at  $\lambda_p = 0.992 \mu\text{m}$ , the normalized spectral overlap is above 0.9 for a 40.7-nm range of input center wavelengths.

Future work includes experimental verification of the devices. The BBO device has been ordered from Conex Systems Technology, Inc. and will be tested in Dr. Jeffrey Moses' laboratory at Cornell University. To demonstrate the homogenization capabilities, the output spectrum will be measured for several narrowband input spectra selected using the NIR 4f pulse shapers. By tilting the crystal, the phase-matching angle can be detuned from the angle necessary to achieve group-velocity matching between the pump and input fields such that homogenization will not occur. Thus, group-velocity-matched operation resulting in homogenization can be directly verified. The Rb:KTP waveguide is being manufactured by AdvR, Inc. and will be tested at the Air Force Research Laboratory in Rome, NY. A nondegenerate spontaneous parametric downconversion source driven at 325 nm will be used to generate the input photons. The performance of the device will be analyzed by tuning the input center wavelength. The quantum characteristics will be investigated by measuring the visibility of Hong-Ou-Mandel interference between the outputs of two devices seeded with input spectra at different center wavelengths.

APPENDIX A  
PHASE MATCHING OPA PROCESSES

## A.1 GROUP-VELOCITY MATCHING IN NONCOLLINEAR CONFIGURATION

The relationship between the group velocities of the signal and idler in the non-collinear configuration can be determined under the phase-matched condition by setting the components of the wave-vector mismatch in Eqs. 2.8 to zero and taking the derivative with respect to the signal angular frequency:

$$\Delta k_{\parallel} = 0 = \frac{\partial}{\partial \omega_s} (k_p \cos(\alpha)) - \frac{\partial}{\partial \omega_s} k_s - \frac{\partial \omega_i}{\partial \omega_s} \frac{\partial}{\partial \omega_i} (k_i \cos(\beta)) \quad (\text{A.1a})$$

$$\Delta k_{\perp} = 0 = \frac{\partial}{\partial \omega_s} (k_p \sin(\alpha)) - \frac{\partial \omega_i}{\partial \omega_s} \frac{\partial}{\partial \omega_i} (k_i \sin(\beta)), \quad (\text{A.1b})$$

where the chain rule has been used for terms that are explicitly dependent on the idler angular frequency.

Now, let us consider Eqs. A.1a and A.1b. The first term in Eq. A.1a is zero because  $k_p$  and  $\alpha$  are constant with respect to the signal angular frequency. The second term is the inverse of the signal group velocity  $\frac{\partial k_s}{\partial \omega_s} = v_s^{-1}$ . Using  $\frac{\partial \omega_i}{\partial \omega_s} = -1$  from conservation of energy and the product rule, the third term can be simplified to

$$\begin{aligned} \frac{\partial \omega_i}{\partial \omega_s} \frac{\partial}{\partial \omega_i} (k_i \cos(\beta)) &= - \left( \frac{\partial k_i}{\partial \omega_i} \cos(\beta) - k_i \sin(\beta) \frac{\partial \beta}{\partial \omega_i} \right) \\ &= - \left( v_i^{-1} \cos(\beta) - k_i \sin(\beta) \frac{\partial \beta}{\partial \omega_i} \right). \end{aligned} \quad (\text{A.2})$$

Finally, Eq. A.1a becomes

$$\Delta k_{\parallel} = 0 = -v_s^{-1} + v_i^{-1} \cos(\beta) - k_i \sin(\beta) \frac{\partial \beta}{\partial \omega_i}. \quad (\text{A.3})$$

Similarly, Eq. A.1b becomes

$$\Delta k_{\perp} = 0 = v_i^{-1} \sin(\beta) + k_i \cos(\beta) \frac{\partial \beta}{\partial \omega_i}. \quad (\text{A.4})$$

Solving Eq. A.4 for  $k_i \frac{\partial \beta}{\partial \omega_i}$  and substituting it into Eq. A.3 yields

$$\begin{aligned} 0 &= -v_s^{-1} + v_i^{-1} \cos(\beta) - \left( -\frac{v_i^{-1} \sin(\beta)}{\cos(\beta)} \right) \sin \beta \\ &= -v_s^{-1} \cos(\beta) + v_i^{-1} \cos^2(\beta) + v_i^{-1} \sin^2(\beta) \\ &= -v_s^{-1} \cos(\beta) + v_i^{-1}. \end{aligned} \quad (\text{A.5})$$

Eq. 2.9 is obtained from Eq. A.5.

APPENDIX B  
FROST RETRIEVAL ALGORITHM

### B.1 OVERVIEW

The FROSt technique uses a ptychographic phase retrieval algorithm to reconstruct the measured trace,  $I(\omega, \tau)$ , where  $\omega$  is the angular frequency of the probe pulse and  $\tau$  is the delay between the pump and probe pulses. For our implementation, we follow the procedure outlined in Ref. [76] which begins with the Hybrid Input-Output scheme [37,41,42] to identify the space of all approximate solutions and ends with the Error Reduction scheme [42,45] to find the closest local solution. Additional ptychography methods and algorithms are reviewed in Refs. [9,84,108].

The goal is to determine the probe electric field  $P(t)$  and the switch function  $S(t)$  created by the transient absorption of the free-carriers excited by the pump pulse. The measured trace can be expressed as

$$I(\omega, \tau) = \left| \int_t P(t)S(t - \tau)e^{j\omega t} dt \right|^2. \quad (\text{B.1})$$

By defining a function  $Q(t, \tau) = P(t)S(t - \tau)$  as a product between the probe electric field and the switch function delayed by a time  $\tau$ , Eq. B.1 can be expressed as

$$I(\omega, \tau) = |\mathcal{F}[Q(t, \tau)]|^2, \quad (\text{B.2})$$

where  $\mathcal{F}$  represents Fourier transformation from  $t \rightarrow \omega$  ( $\mathcal{F}^{-1}$  is the inverse Fourier transformation).

The retrieval algorithm uses two projections to update  $Q(t, \tau)$ . These projections are the experimental projection  $\Pi_E$ , performed in the frequency domain,

and the product projection  $\Pi_P$ , performed in the time domain. The experimental projection  $\Pi_E$  constrains the Fourier magnitude of  $Q(t, \tau)$  to the measured trace  $I_E(\omega, \tau)$ , such that

$$\Pi_E [Q(t, \tau)] = \mathcal{F}^{-1} \left[ \frac{\mathcal{F}[Q(t, \tau)]}{|\mathcal{F}[Q(t, \tau)]|} \sqrt{I_E(\omega, \tau)} \right]. \quad (\text{B.3})$$

The product projection  $\Pi_P$  fits  $Q(t, \tau)$  with the product of two guessed functions such that

$$\Pi_P [Q(t, \tau)] = P_g(t)S_g(t - \tau), \quad (\text{B.4})$$

where  $P_g(t)$  and  $S_g(t - \tau)$  are guesses for the probe electric field and the switch function delayed by a time  $\tau$ , respectively. The guessed functions,  $P_g(t)$  and  $S_g(t)$ , are obtained by minimizing the least-square error  $\epsilon$  given by

$$\epsilon = \sum_{t, \tau} |Q(t, \tau) - P_g(t)S_g(t - \tau)|^2. \quad (\text{B.5})$$

The least-square error is minimized when the complex gradients with respect to the guessed functions are equal to zero such that  $\partial\epsilon/\partial P_g = \partial\epsilon/\partial S_g = 0$ . Solving for  $P_g(t)$  and  $S_g(t)$  gives

$$P_g(t) = \frac{\int Q(t, \tau)S_g^*(t - \tau)d\tau}{\int |S_g(t - \tau)|^2 d\tau} \quad (\text{B.6a})$$

$$S_g(t) = \frac{\int Q(t + \tau, \tau)P_g^*(t + \tau)d\tau}{\int |P_g(t + \tau)|^2 d\tau}. \quad (\text{B.6b})$$

These create a coupled system of equations that can be iteratively solved. Starting with a random complex guess for  $S_g$ ,  $P_g$  can be calculated from Eq. B.6a. Then,  $S_g$  is recalculated using Eq. B.6b. Repeating this procedure, the guessed functions  $P_g$  and  $S_g$  can be found within a few iterations, typically  $<10$ .

In the retrieval algorithm, these projections are applied in two ways to produce different converging behaviors [42]. First is the Hybrid Input-Output

(HIO) scheme described in Refs. [37, 41, 42]. Here,  $Q(t, \tau)$  for the next iteration ( $n + 1$ ) is given by

$$Q_{(n+1)}^{HIO} = Q_{(n)} + \Pi_E[2\Pi_P[Q_{(n)}] - Q_{(n)}] - \Pi_P[Q_{(n)}]. \quad (\text{B.7})$$

Second is the Error Reduction (ER) scheme described in Ref. [42, 45] where  $Q(t, \tau)$  for the next iteration ( $n + 1$ ) is given by

$$Q_{(n+1)}^{ER} = \Pi_E[\Pi_P[Q_{(n)}]]. \quad (\text{B.8})$$

The algorithm is summarized in Fig. B.1. First, an initial probe electric field

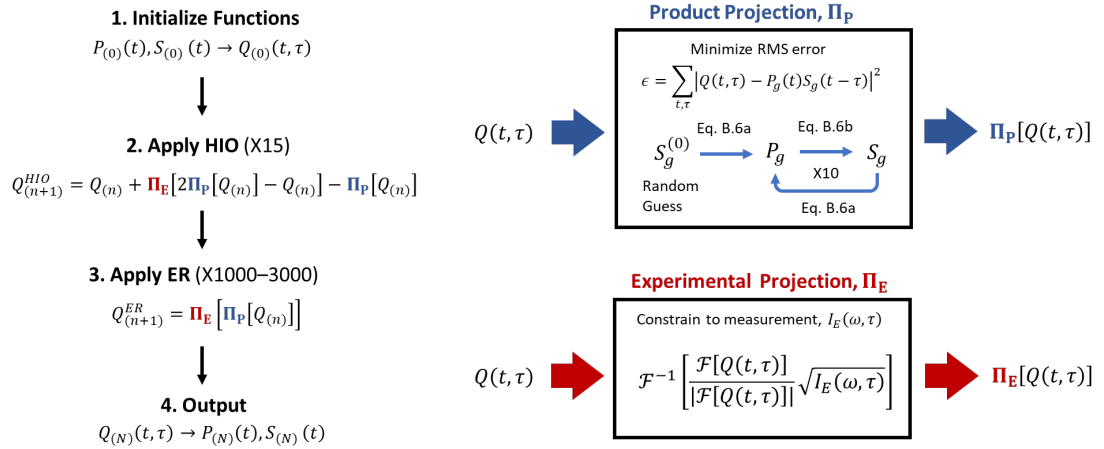


Figure B.1: Diagram of FROSt retrieval algorithm. (left) Algorithm overview. (right) Experimental and product projections used in the HIO and ER schemes.

and switch function, which could be random functions or educated guesses (e.g. the probe pulse amplitude with a specified amount of dispersion), are used to construct the initial function  $Q_{(0)}(t, \tau)$ . Next, the HIO scheme is used for the first 15 iterations. Note, the projections used in each scheme are outlined on the right side of Fig. B.1. Using the HIO scheme, the algorithm converges to a steady-state regime where it continues to explore the space of all approximate solutions. Finally, the ER scheme is applied for a few thousand iterations which slowly converges to the closest local solution. Typically, 1000–3000 iterations

are sufficient for convergence. The retrieved switch function and probe electric field are calculated from  $Q_{(N)}(t, \tau)$  from the final iteration ( $N$ ).

## BIBLIOGRAPHY

- [1] B. Albrecht, P. Farrera, X. Fernandez-Gonzalvo, M. Cristiani, and H. de Riedmatten. A waveguide frequency converter connecting rubidium-based quantum memories to the telecom C-band. *Nat. Commun.*, 5:3376, Feb 2014.
- [2] J. Alda. Laser and gaussian beam propagation and transformation. In R. G. Driggers, C. Hoffman, and R. Driggers, editors, *Encyclopedia of Optical Engineering*, pages 999–1013. CRC Press, 2003.
- [3] M. A. Arbore, A. Galvanauskas, D. Harter, M. H. Chou, and M. M. Fejer. Engineerable compression of ultrashort pulses by use of second-harmonic generation in chirped-period-poled lithium niobate. *Opt. Lett.*, 22(17):1341–1343, Sep 1997.
- [4] B. K. Armstrong and A. Krieger. The epidemiology of UV induced skin cancer. *J. Photoch. Photobio. B*, 63(1):8–18, 2001.
- [5] J. B. Ashcom, R. R. Gattass, C. B. Schaffer, and E. Mazur. Numerical aperture dependence of damage and supercontinuum generation from femtosecond laser pulses in bulk fused silica. *J. Opt. Soc. Am. B*, 23(11):2317–2322, Nov 2006.
- [6] S. Ates, I. Agha, A. Gulinatti, I. Rech, M. T. Rakher, A. Badolato, and K. Srinivasan. Two-photon interference using background-free quantum frequency conversion of single photons emitted by an InAs quantum dot. *Phys. Rev. Lett.*, 109:147405, Oct 2012.
- [7] N. B. Baranova. Adiabatic transition of the pump into second optical harmonic. *JETP Lett.*, 1993.
- [8] N. B. Baranova, M. A. Bolshtyanskii, and B. Ya Zel'dovich. Adiabatic energy transfer from a pump wave to its second harmonic. *Quantum Electron.*, 25(7):638–640, Jul 1995.
- [9] H. H. Bauschke, P. L. Combettes, and D. R. Luke. Phase retrieval, error reduction algorithm, and fienup variants: a view from convex optimization. *J. Opt. Soc. Am. A*, 19(7):1334–1345, Jul 2002.
- [10] P. Berthold, S. P. Tsunoda, O. P. Ernst, W. Mages, D. Gradmann, and P. Hegemann. Channelrhodopsin-1 initiates phototaxis and photopho-

- bic responses in *Chlamydomonas* by immediate light-induced depolarization. *The Plant Cell*, 20(6):1665–1677, 06 2008.
- [11] G. D. Boyd and D. A. Kleinman. Parametric interaction of focused gaussian light beams. *J. Appl. Phys.*, 39(8):3597–3639, 1968.
- [12] R. W. Boyd. *Nonlinear Optics*. Academic Press, 3 edition, 2008.
- [13] E. S. Boyden, F. Zhang, E. Bamberg, G. Nagel, and K. Deisseroth. Millisecond-timescale, genetically targeted optical control of neural activity. *Nat. Neurosci.*, 8(9):1263–1268, 2005.
- [14] D. Brida, A. Tomadin, C. Manzoni, Y. J. Kim, A. Lombardo, S. Milana, R. R. Nair, K. S. Novoselov, A. C. Ferrari, G. Cerullo, and M. Polini. Ultrafast collinear scattering and carrier multiplication in graphene. *Nat. Commun.*, 4:1987, Jun 2013.
- [15] W. S. Brocklesby. Progress in high average power ultrafast lasers. *The European Physical Journal Special Topics*, 224(13):2529–2543, 2015.
- [16] A.-L. Calendron, H. Çankaya, G. Cirmi, and F. X. Kärtner. White-light generation with sub-ps pulses. *Opt. Express*, 23(11):13866–13879, Jun 2015.
- [17] J. C. Camparo and R. P. Frueholz. A dressed atom interpretation of adiabatic rapid passage. *J. Phys. B: At. Mol. Opt.*, 17(20):4169–4178, Oct 1984.
- [18] G. Cerullo and S. De Silvestri. Ultrafast optical parametric amplifiers. *Rev. Sci. Instrum.*, 74(1):1–18, 2003.
- [19] I. C. Chang. *Handbook of Optics*, volume 2, chapter 12. Acousto-Optic Devices and Applications. McGraw-Hill, 2 edition, 1995.
- [20] I. Gražulevičiūtė, M. Skeivyte, E. Keblyte, J. Galinis, G. Tamosauskas, and A. Dubietis. Supercontinuum generation in YAG and sapphire with picosecond laser pulses. *Lith. J. Phys.*, 55, 2015.
- [21] I. Conti, P. Altoè, M. Stenta, M. Garavelli, and G. Orlandi. Adenine deactivation in DNA resolved at the CASPT2//CASSCF/AMBER level. *Phys. Chem. Chem. Phys.*, 12:5016–5023, 2010.
- [22] I. Conti, A. Nenov, S. Höfner, S. Flavio Altavilla, I. Rivalta, E. Dumont, G. Orlandi, and M. Garavelli. Excited state evolution of DNA

- stacked adenines resolved at the CASPT2//CASSCF/Amber level: from the bright to the excimer state and back. *Phys. Chem. Chem. Phys.*, 17:7291–7302, 2015.
- [23] C. E. Crespo-Hernández, B. Cohen, P. M. Hare, and B. Kohler. Ultrafast excited-state dynamics in nucleic acids. *Chem. Rev.*, 104(4):1977–2020, 2004. PMID: 15080719.
- [24] J. K. Daniel. Principal components generalized projections: a review. *J. Opt. Soc. Am. B*, 25(6):A120–A132, Jun 2008.
- [25] C. Danson, D. Hillier, N. Hopps, and D. Neely. Petawatt class lasers worldwide. *High Power Laser Science and Engineering*, 3:e3, 2015.
- [26] L. Daya-Grosjean and A. Sarasin. The role of UV induced lesions in skin carcinogenesis: an overview of oncogene and tumor suppressor gene modifications in xeroderma pigmentosum skin tumors. *Mutat. Res.-Fund. Mol. M.*, 571(1):43–56, 2005. Biological Effects of Ultraviolet Radiation.
- [27] K. De Greve, L. Yu, P. L. McMahon, J. S. Pelc, C. M. Natarajan, N. Y. Kim, E. Abe, S. Maier, C. Schneider, M. Kamp, S. Höfling, R. H. Hadfield, A. Forchel, M. M. Fejer, and Y. Yamamoto. Quantum-dot spin–photon entanglement via frequency downconversion to telecom wavelength. *Nature*, 491:421–425, Nov 2012.
- [28] K. Deisseroth and P. Hegemann. The form and function of channel-rhodopsin. *Science*, 357(6356):eaan5544, 2017.
- [29] A. K. Dharmadhikari, J. A. Dharmadhikari, and D. Mathur. Visualization of focusing-refocusing cycles during filamentation in BaF<sub>2</sub>. *Appl. Phys. B*, 94(259), 2009.
- [30] A. K. Dharmadhikari, F. A. Rajgara, and D. Mathur. Systematic study of highly efficient white light generation in transparent materials using intense femtosecond laser pulses. *Appl. Phys. B*, 80:61–66, Jan 2005.
- [31] A. Dubietis, G. Jonušauskas, and A. Piskarskas. Powerful femtosecond pulse generation by chirped and stretched pulse parametric amplification in BBO crystal. *Opt. Commun.*, 88(4):437–440, 1992.
- [32] A. Dubietis, G. Tamošauskas, R. Šuminas, V. Jukna, and A. Couairon. Ul-

trafast supercontinuum generation in bulk condensed media (Invited Review), 2017.

- [33] M. A. Dugan, J. X. Tull, and W. S. Warren. High-resolution acousto-optic shaping of unamplified and amplified femtosecond laser pulses. *J. Opt. Soc. Am. B*, 14(9):2348–2358, Sep 1997.
- [34] T. Eidam, S. Hanf, E. Seise, T. V. Andersen, T. Gabler, C. Wirth, T. Schreiber, J. Limpert, and A. Tünnermann. Femtosecond fiber CPA system emitting 830 W average output power. *Opt. Lett.*, 35(2):94–96, Jan 2010.
- [35] T. Eidam, J. Rothhardt, F. Stutzki, F. Jansen, S. Hädrich, H. Carstens, C. Jauregui, J. Limpert, and A. Tünnermann. Fiber chirped-pulse amplification system emitting 3.8 GW peak power. *Opt. Express*, 19(1):255–260, Jan 2011.
- [36] M. D. Eisaman, J. Fan, A. Migdall, and S. V. Polyakov. Invited review article: Single-photon sources and detectors. *Rev. Sci. Instrum.*, 82(7):071101, 2011.
- [37] V. Elser. Phase retrieval by iterated projections. *J. Opt. Soc. Am. A*, 20(1):40–55, Jan 2003.
- [38] A. B. Fallahkhair, K. S. Li, and T. E. Murphy. Vector finite difference modesolver for anisotropic dielectric waveguides. *J. Lightw. Technol.*, 26(11):1423–1431, 2008.
- [39] M. R. Fetterman, D. Goswami, D. Keusters, W. Yang, J.-K. Rhee, and W. S. Warren. Ultrafast pulse shaping: amplification and characterization. *Opt. Express*, 3(10):366–375, Nov 1998.
- [40] J. J. Field, T. A. Planchon, W. Amir, C. G. Durfee, and J. A. Squier. Characterization of a high efficiency, ultrashort pulse shaper incorporating a reflective 4096-element spatial light modulator. *Opt. Commun.*, 278(2):368–376, 2007.
- [41] J. R. Fienup. Reconstruction of an object from the modulus of its Fourier transform. *Opt. Lett.*, 3(1):27–29, Jul 1978.
- [42] J. R. Fienup. Phase retrieval algorithms: a comparison. *Appl. Opt.*, 21(15):2758–2769, Aug 1982.

- [43] N. Flemens, P. Krogen, H. Suchowski, H. Liang, K.-H. Hong, F. X. Kärtner, and J. Moses. Single-cycle or arbitrarily shaped octave-spanning mid-infrared pulses: Intrinsic and extrinsic pulse shaping in adiabatic frequency conversion. In *High-Brightness Sources and Light-driven Interactions*, page MW2C.7. Optical Society of America, 2018.
- [44] J. Galinis, G. Tamošauskas, I. Gražulevičiūtė, E. Keblytė, V. Jukna, and A. Dubietis. Filamentation and supercontinuum generation in solid-state dielectric media with picosecond laser pulses. *Phys. Rev. A*, 92:033857, Sep 2015.
- [45] R. W. Gerchberg and W. O. Saxton. A practical algorithm for the determination of phase from image and diffraction plane pictures. *Optik*, 35:237–246, 1972.
- [46] A. Ghosh, A. L. Serrano, T. A. Oudenhoven, J. S. Ostrander, E. C. Eklund, A. F. Blair, and M. T. Zanni. Experimental implementations of 2d ir spectroscopy through a horizontal pulse shaper design and a focal plane array detector. *Opt. Lett.*, 41(3):524–527, Feb 2016.
- [47] I. Gierz, F. Calegari, S. Aeschlimann, M. Chávez Cervantes, C. Cacho, R. T. Chapman, E. Springate, S. Link, U. Starke, C. R. Ast, and A. Cavalleri. Tracking primary thermalization events in graphene with photoemission at extreme time scales. *Phys. Rev. Lett.*, 115:086803, Aug 2015.
- [48] F. Graffitti, J. Kelly-Massicotte, A. Fedrizzi, and A. M. Brańczyk. Design considerations for high-purity heralded single-photon sources. *Phys. Rev. A*, 98:053811, Nov 2018.
- [49] M. Grimau Puigibert, G. H. Aguilar, Q. Zhou, F. Marsili, M. D. Shaw, V. B. Verma, S. W. Nam, D. Oblak, and W. Tittel. Heralded single photons based on spectral multiplexing and feed-forward control. *Phys. Rev. Lett.*, 119:083601, Aug 2017.
- [50] T. Gustavsson, N. Sarkar, I. Vayá, M. C. Jiménez, D. Markovitsi, and R. Improta. A joint experimental/theoretical study of the ultrafast excited state deactivation of deoxyadenosine and 9-methyladenine in water and acetonitrile. *Photochem. Photobiol. Sci.*, 12:1375–1386, 2013.
- [51] D. A. Heberle, N. R. Flemens, X. Ding, W.-Z. Chang, and J. Moses. Towards a 10-fs hyperspectral spectroscopy source with arbitrary pulse shaping based on adiabatic frequency conversion. In *EPJ Web of Conferences*, volume 205, page 01027. EDP Sciences, 2019.

- [52] D. A. Heberle, C. T. Middleton, N. R. Flemens, and J. Moses. Understanding chromatic aberrations in 4f few-cycle pulse shapers. In *Ultrafast Optics 2019*, volume 11370, pages 379–382. SPIE, 2019.
- [53] C. Heese, C. R. Phillips, B. W. Mayer, L. Gallmann, M. M. Fejer, and U. Keller. 75 mw few-cycle mid-infrared pulses from a collinear apodized appln-based opcpa. *Opt. Express*, 20(24):26888–26894, Nov 2012.
- [54] C. W. Hillegas, J. X. Tull, D. Goswami, D. Strickland, and W. S. Warren. Femtosecond laser pulse shaping by use of microsecond radio-frequency pulses. *Opt. Lett.*, 19(10):737–739, May 1994.
- [55] G. Hithell, P. M. Donaldson, G. M. Greetham, M. Towrie, A. W. Parker, G. A. Burley, and N. T. Hunt. Effect of oligomer length on vibrational coupling and energy relaxation in double-stranded dna. *Chem. Phys.*, 512:154–164, 2018. Advanced Vibrational Spectroscopies, dedicated to Dr. Edwin J. Heilweil on the occasion of his 60th birthday.
- [56] R. Ikuta, Y. Kusaka, T. Kitano, H. Kato, T. Yamamoto, M. Koashi, and N. Imoto. Wide-band quantum interface for visible-to-telecommunication wavelength conversion. *Nat. Commun.*, 2:537, Nov 2011.
- [57] G. Imeshev, M. M. Fejer, A. Galvanauskas, and D. Harter. Pulse shaping by difference-frequency mixing with quasi-phase-matching gratings. *J. Opt. Soc. Am. B*, 18(4):534–539, Apr 2001.
- [58] C. Jauregui, J. Limpert, and A. Tünnermann. High-power fibre lasers. *Nat. Photonics*, 7(11):861–867, Nov 2013.
- [59] A. C. Jones, N. M. Kearns, M. Bohlmann Kunz, J. T. Flach, and M. T. Zanni. Multidimensional spectroscopy on the microscale: Development of a multimodal imaging system incorporating 2d white-light spectroscopy, broadband transient absorption, and atomic force microscopy. *J. Phys. Chem. A*, 123(50):10824–10836, 2019. PMID: 31697080.
- [60] A. C. Jones, M. Bohlmann Kunz, I. Tigges-Green, and M. T. Zanni. Dual spectral phase and diffraction angle compensation of a broadband aom 4-f pulse-shaper for ultrafast spectroscopy. *Opt. Express*, 27(26):37236–37247, Dec 2019.
- [61] D. J. Kane. Real-time measurement of ultrashort laser pulses using principal component generalized projections. *IEEE J. Sel. Top. Quant.*, 4(2):278–284, 1998.

- [62] D. J. Kane. Recent progress toward real-time measurement of ultrashort laser pulses. *IEEE J. Quantum. Elect.*, 35(4):421–431, 1999.
- [63] K. Kato. High-power difference-frequency generation at 4.4–5.7  $\mu\text{m}$  in  $\text{LiIO}_3$ . *IEEE J. Quantum Electron.*, 21(2):119–120, 1985.
- [64] K. Kato. Second-harmonic generation to 2048  $\text{\AA}$  in  $\beta\text{-Ba}_2\text{O}_4$ . *IEEE J. Quantum Electron.*, 22(7):1013–1014, 1986.
- [65] K. Kato. Temperature-tuned  $90^\circ$  phase-matching properties of  $\text{LiB}_3\text{O}_5$ . *IEEE J. Quantum Electron.*, 30(12):2950–2952, 1994.
- [66] K. Kato and E. Takaoka. Sellmeier and thermo-optic dispersion formulas for KTP. *Appl. Opt.*, 41(24):5040–5044, Aug 2002.
- [67] D. A. Kleinman, A. Ashkin, and G. D. Boyd. Second-harmonic generation of light by focused laser beams. *Phys. Rev.*, 145:338–379, May 1966.
- [68] H. Kogelnik and T. Li. Laser beams and resonators. *Appl. Opt.*, 5(10):1550–1567, Oct 1966.
- [69] P. Krogen, H. Suchowski, H. Liang, N. Flemens, K.-H. Hong, F. X. Kärtner, and J. Moses. Generation and multi-octave shaping of mid-infrared intense single-cycle pulses. *Nat. Photonics*, 11(4):222–226, Apr 2017.
- [70] P. Kumar. Quantum frequency conversion. *Opt. Lett.*, 15(24):1476–1478, Dec 1990.
- [71] C. Kurtsiefer, S. Mayer, P. Zarda, and H. Weinfurter. Stable solid-state source of single photons. *Phys. Rev. Lett.*, 85:290–293, Jul 2000.
- [72] W.-M. Kwok, C. Ma, and D. L. Phillips. Femtosecond time- and wavelength-resolved fluorescence and absorption spectroscopic study of the excited states of adenosine and an adenine oligomer. *J. Am. Chem. Soc.*, 128(36):11894–11905, 2006. PMID: 16953630.
- [73] L. D. Landau. Zur theorie der energieubertragung ii. *Z. Sowjetunion*, 2:46–51, 1932.
- [74] C. K. Law and J. H. Eberly. Analysis and interpretation of high transverse entanglement in optical parametric down conversion. *Phys. Rev. Lett.*, 92:127903, Mar 2004.

- [75] C. K. Law, I. A. Walmsley, and J. H. Eberly. Continuous frequency entanglement: Effective finite Hilbert space and entropy control. *Phys. Rev. Lett.*, 84:5304–5307, Jun 2000.
- [76] A. Leblanc, P. Lassonde, S. Petit, J.-C. Delagnes, E. Haddad, G. Ernotte, M. R. Bionta, V. Gruson, B. E. Schmidt, H. Ibrahim, E. Cormier, and F. Légaré. Phase-matching-free pulse retrieval based on transient absorption in solids. *Opt. Express*, 27(20):28998–29015, Sep 2019.
- [77] A. Leblanc, A. Longa, M. Kumar, A. Laramée, C. Dansereau, H. Ibrahim, P. Lassonde, and F. Légaré. Temporal characterization of two-octave infrared pulses by frequency resolved optical switching. *J. Phys.-Photonics*, 3(4):045002, aug 2021.
- [78] Q. Li, M. Davanço, and K. Srinivasan. Efficient and low-noise single-photon-level frequency conversion interfaces using silicon nanophotonics. *Nat. Photonics*, 10:406–414, Jun 2016.
- [79] W. Liu, S. L. Chin, O. Kosareva, I. S. Golubtsov, and V. P. Kandidov. Multiple refocusing of a femtosecond laser pulse in a dispersive liquid (methanol). *Opt. Commun.*, 225(1):193–209, 2003.
- [80] M. Maiuri, M. Garavelli, and G. Cerullo. Ultrafast spectroscopy: State of the art and open challenges. *J. Am. Chem. Soc.*, 142(1):3–15, 2020. PMID: 31800225.
- [81] V. S. Malinovsky and J. L. Krause. General theory of population transfer by adiabatic rapid passage with intense, chirped laser pulses. *The European Physical Journal D - Atomic, Molecular, Optical and Plasma Physics*, 14(2):147–155, Jan 2001.
- [82] I. H. Malitson. Interspecimen comparison of the refractive index of fused silica\*,†. *J. Opt. Soc. Am.*, 55(10):1205–1209, Oct 1965.
- [83] C. Manzoni and G. Cerullo. Design criteria for ultrafast optical parametric amplifiers. *J. Opt.*, 18(10):103501, Aug 2016.
- [84] S. Marchesini. Invited article: A unified evaluation of iterative projection algorithms for phase retrieval. *Review of Scientific Instruments*, 78(1):011301, 2007.
- [85] B. W. Mayer, C. R. Phillips, L. Gallmann, M. M. Fejer, and U. Keller. Sub-

- four-cycle laser pulses directly from a high-repetition-rate optical parametric chirped-pulse amplifier at 3.4  $\mu\text{m}$ . *Opt. Lett.*, 38(21):4265–4268, Nov 2013.
- [86] T. Metzger, A. Schwarz, C. Yuriko Teisset, D. Sutter, A. Killi, R. Kienberger, and F. Krausz. High-repetition-rate picosecond pump laser based on a yb:yag disk amplifier for optical parametric amplification. *Opt. Lett.*, 34(14):2123–2125, Jul 2009.
- [87] C. T. Middleton, K. de La Harpe, C. Su, Y. K. Law, C. E. Crespo-Hernández, and B. Kohler. DNA excited-state dynamics: From single bases to the double helix. *Annu. Rev. Phys. Chem.*, 60(1):217–239, 2009. PMID: 19012538.
- [88] A. Monmayrant, S. Weber, and B. Chatel. A newcomer's guide to ultrashort pulse shaping and characterization. *J. Phys. B-At. Mol. Opt.*, 43(10):103001, may 2010.
- [89] J. Moses and S.-W. Huang. Conformal profile theory for performance scaling of ultrabroadband optical parametric chirped pulse amplification. *J. Opt. Soc. Am. B*, 28(4):812–831, Apr 2011.
- [90] J. Moses, C. Manzoni, S.-W. Huang, G. Cerullo, and F. X. Kärtner. Temporal optimization of ultrabroadband high-energy opcpa. *Opt. Express*, 17(7):5540–5555, Mar 2009.
- [91] J. Moses, H. Suchowski, and F. X. Kärtner. Fully efficient adiabatic frequency conversion of broadband ti:sapphire oscillator pulses. *Opt. Lett.*, 37(9):1589–1591, May 2012.
- [92] G. Nagel, D. Ollig, M. Fuhrmann, S. Kateriya, A. Maria Musti, E. Bamberg, and P. Hegemann. Channelrhodopsin-1: A light-gated proton channel in green algae. *Science*, 296(5577):2395–2398, 2002.
- [93] G. Nagel, T. Szellas, W. Huhn, S. Kateriya, N. Adeishvili, P. Berthold, D. Ollig, P. Hegemann, and E. Bamberg. Channelrhodopsin-2, a directly light-gated cation-selective membrane channel. *P. Natl. Acad. Sci. USA*, 100(24):13940–13945, 2003.
- [94] N. T. Nguyen, A. Saliminia, W. Liu, S. L. Chin, and R. Vallée. Optical breakdown versus filamentation in fused silica by use of femtosecond infrared laser pulses. *Opt. Lett.*, 28(17):1591–1593, Sep 2003.

- [95] J. M. Nite, J. D. Cyran, and A. T. Krummel. Active bragg angle compensation for shaping ultrafast mid-infrared pulses. *Opt. Express*, 20(21):23912–23920, Oct 2012.
- [96] M. Nobuyuki. Deterministic reshaping of single-photon spectra using cross-phase modulation. *Science Advances*, 2(3):e1501223, 2016.
- [97] T. Nubbemeyer, M. Kaumanns, M. Ueffing, M. Gorjan, A. Alismail, H. Fattahi, J. Brons, O. Pronin, H. G. Barros, Z. Major, T. Metzger, D. Sutter, and F. Krausz. 1 kw, 200 mj picosecond thin-disk laser system. *Opt. Lett.*, 42(7):1381–1384, Apr 2017.
- [98] K. Oda, J. Vierock, S. Oishi, S. Rodriguez-Rozada, R. Taniguchi, K. Yamashita, J. S. Wiegert, T. Nishizawa, P. Hegemann, and O. Nureki. Crystal structure of the red light-activated channelrhodopsin Chrimson. *Nat. Commun.*, 9(1):3949, 2018.
- [99] T. Oksenhendler and N. Forget. *Advances in Solid State Lasers: Development and Applications*, chapter 16. Pulse-Shaping Techniques Theory and Experimental Implementations for Femtosecond Pulses. IntechOpen, 2010.
- [100] J. S. Ostrander, A. L. Serrano, A. Ghosh, and M. T. Zanni. Spatially resolved two-dimensional infrared spectroscopy via wide-field microscopy. *ACS Photonics*, 3(7):1315–1323, 2016. PMID: 27517058.
- [101] S. Parker, S. Bose, and M. B. Plenio. Entanglement quantification and purification in continuous-variable systems. *Phys. Rev. A*, 61:032305, Feb 2000.
- [102] C. R. Phillips and M. M. Fejer. Efficiency and phase of optical parametric amplification in chirped quasi-phase-matched gratings. *Opt. Lett.*, 35(18):3093–3095, Sep 2010.
- [103] E. D. Pleasance, R. K. Cheetham, P. J. Stephens, D. J. McBride, S. J. Humphray, I. Greenman, C. D. and Varela, M.-L. Lin, G. R. Ordóñez, G. R. Bignell, K. Ye, J. Alipaz, M. J. Bauer, D. Beare, A. Butler, R. J. Carter, L. Chen, A. J. Cox, S. Edkins, P. I. Kokko-Gonzales, N. A. Gormley, R. J. Grocock, C. D. Haudenschild, M. M. Hims, T. James, M. Jia, Z. Kingsbury, C. Leroy, J. Marshall, A. Menzies, L. J. Mudie, Z. Ning, T. Royce, O. B. Schulz-Trieglaff, A. Spiridou, L. A. Stebbings, L. Szajkowski, J. Teague, D. Williamson, L. Chin, M. T. Ross, P. J. Campbell, D. R. Bentley, P. A. Futreal, and M. R. Stratton. The role of UV induced lesions in skin carcino-

genesis: an overview of oncogene and tumor suppressor gene modifications in xeroderma pigmentosum skin tumors. *Nature*, 463(7278):191–196, 2010. Biological Effects of Ultraviolet Radiation.

- [104] D. Polli, P. Altoé, O. Weingart, K. M. Spillane, C. Manzoni, D. Brida, G. Tomasello, G. Orlandi, P. Kukura, R. A. Mathies, M. Garavelli, and G. Cerullo. Conical intersection dynamics of the primary photoisomerization event in vision. *Nature*, 467:440–443, Sep 2010.
- [105] I. I. Rabi. Space quantization in a gyrating magnetic field. *Phys. Rev.*, 51:652–654, Apr 1937.
- [106] M. T. Rakher, L. Ma, M. Davanço, O. Slattery, X. Tang, and K. Srinivasan. Simultaneous wavelength translation and amplitude modulation of single photons from a quantum dot. *Phys. Rev. Lett.*, 107:083602, Aug 2011.
- [107] M. T. Rakher, L. Ma, O. Slattery, X. Tang, and K. Srinivasan. Quantum transduction of telecommunications-band single photons from a quantum dot by frequency upconversion. *Nat. Photonics*, 4:786–791, Nov 2010.
- [108] J. Rodenburg and A. Maiden. *Handbook of Microscopy*, chapter 17. Ptychography. Springer Nature, 2019.
- [109] S. Rodt, S. Reitzenstein, and T. Heindel. Deterministically fabricated solid-state quantum-light sources. *J. Phys.-Condens. Mat.*, 32(15):153003, Jan 2020.
- [110] I. N. Ross, P. Matousek, G. H. C. New, and K. Osvay. Analysis and optimization of optical parametric chirped pulse amplification. *J. Opt. Soc. Am. B*, 19(12):2945–2956, Dec 2002.
- [111] I. N. Ross, P. Matousek, M. Towrie, A. J. Langley, and J. L. Collier. The prospects for ultrashort pulse duration and ultrahigh intensity using optical parametric chirped pulse amplifiers. *Opt. Commun.*, 144(1):125–133, 1997.
- [112] P. Russbueltdt, D. Hoffmann, M. Höfer, J. Löhring, J. Luttmann, A. Meissner, J. Weitenberg, M. Traub, T. Sartorius, D. Esser, R. Wester, P. Loosen, and R. Poprawe. Innoslab amplifiers. *IEEE J. Sel. Top. Quantum Electron.*, 21(1):447–463, 2015.
- [113] P. Russbueltdt, T. Mans, G. Rotarius, J. Weitenberg, H.D. Hoffmann,

- and R. Poprawe. 400 W Yb:YAG Innoslab fs-amplifier. *Opt. Express*, 17(15):12230–12245, 2009.
- [114] P. Russbueldt, T. Mans, J. Weitenberg, H.D. Hoffmann, and R. Poprawe. Compact diode-pumped 1.1 kW Yb:YAG Innoslab femtosecond amplifier. *Opt. Lett.*, 35(24):4169–4171, 2010.
- [115] C. Schnedermann, V. Muders, D. Ehrenberg, R. Schlesinger, P. Kukura, and J. Heberle. Vibronic dynamics of the ultrafast all-trans to 13-cis photoisomerization of retinal in channelrhodopsin-1. *J. Am. Chem. Soc.*, 138(14):4757–4762, 2016. PMID: 26999496.
- [116] R. W. Schoenlein, L. A. Peteanu, R. A. Mathies, and C. V. Shank. The first step in vision: Femtosecond isomerization of rhodopsin. *Science*, 254(5030):412–415, 1991.
- [117] M. Schulz, R. Riedel, A. Willner, T. Mans, C. Schnitzler, P. Russbueldt, J. Dolkemeyer, E. Seise, T. Gottschall, S. Hädrich, et al. Yb: Yag innoslab amplifier: efficient high repetition rate subpicosecond pumping system for optical parametric chirped pulse amplification. *Opt. Lett.*, 36(13):2456–2458, 2011.
- [118] P. G. Schunemann. New nonlinear optical crystals for the mid-infrared. In *Advanced Solid State Lasers*, page AM2A.2. Optical Society of America, 2015.
- [119] A. J. Shields. *Semiconductor quantum light sources*, pages 221–229.
- [120] S.-H. Shim, D. B. Strasfeld, E. C. Fulmer, and M. T. Zanni. Femtosecond pulse shaping directly in the mid-ir using acousto-optic modulation. *Opt. Lett.*, 31(6):838–840, Mar 2006.
- [121] S.-H. Shim, D. B. Strasfeld, Y. L. Ling, and M. T. Zanni. Automated 2d ir spectroscopy using a mid-ir pulse shaper and application of this technology to the human islet amyloid polypeptide. *P. Natl. Acad. Sci. USA*, 104(36):14197–14202, 2007.
- [122] S.-H. Shim, D. B. Strasfeld, and M. T. Zanni. Generation and characterization of phase and amplitude shaped femtosecond mid-ir pulses. *Opt. Express*, 14(26):13120–13130, Dec 2006.
- [123] S.-H. Shim and M. T. Zanni. How to turn your pump–probe instrument

into a multidimensional spectrometer: 2D IR and Vis spectroscopies via pulse shaping. *Phys. Chem. Chem. Phys.*, 11:748–761, 2009.

- [124] B. W. Shore, M. V. Gromovyy, L. P. Yatsenko, and V. I. Romanenko. Simple mechanical analogs of rapid adiabatic passage in atomic physics. *American Journal of Physics*, 77(12):1183–1194, 2009.
- [125] A A Shukhin, D O Akatiev, I Z Latypov, A V Shkalikov, and A A Kalachev. Simulating single-photon sources based on backward-wave spontaneous parametric down-conversion in a periodically poled KTP waveguide. *J. Phys.-Conference Series*, 613:012015, may 2015.
- [126] A. Singh, Q. Li, S. Liu, Y. Yu, X. Lu, C. Schneider, S. Höfling, J. Lawall, V. Verma, R. Mirin, S. W. Nam, J. Liu, and K. Srinivasan. Quantum frequency conversion of a quantum dot single-photon source on a nanophotonic chip. *Optica*, 6(5):563–569, May 2019.
- [127] N. Somaschi, V. Giesz, L. De Santis, J. C. Loredó, M. P. Almeida, G. Hornecker, S. L. Portalupi, T. Grange, C. Antón, J. Demory, C. Gómez, I. Sagnes, N. D. Lanzillotti-Kimura, A. Lemaître, A. Auffeves, A. G. White, L. Lanco, and P. Senellart. Near-optimal single-photon sources in the solid state. *Nat. Photonics*, pages 340–345, May 2016.
- [128] T. M. Spinka and C. Haefner. High-average-power ultrafast lasers. *Optics and Photonics News*, 28(10):26–33, 2017.
- [129] T. Stensitzki, Y. Yang, V. Muders, R. Schlesinger, J. Heberle, and K. Heyne. Femtosecond infrared spectroscopy of channelrhodopsin-1 chromophore isomerization. *Struct. Dynam.*, 3(4):043208, 2016.
- [130] M. A. Steves, H. Zheng, and K. L. Knappenberger. Correlated spatially resolved two-dimensional electronic and linear absorption spectroscopy. *Opt. Lett.*, 44(8):2117–2120, Apr 2019.
- [131] H. Suchowski, B. D. Bruner, A. Ganany-Padowicz, I. Juwiler, A. Arie, and Y. Silberberg. Adiabatic frequency conversion of ultrafast pulses. *Appl. Phys. B*, 105(4):697–702, Jan 2011.
- [132] H. Suchowski, P. R. Krogen, S.-W. Huang, F. X. Kärtner, and J. Moses. Octave-spanning coherent mid-IR generation via adiabatic difference frequency conversion. *Opt. Express*, 21(23):28892–28901, Nov 2013.

- [133] H. Suchowski, D. Oron, A. Arie, and Y. Silberberg. Geometrical representation of sum frequency generation and adiabatic frequency conversion. *Phys. Rev. A*, 78:063821, Dec 2008.
- [134] H. Suchowski, G. Porat, and A. Arie. Adiabatic processes in frequency conversion. *Laser Photonics Rev.*, 8(3):333–367, 2014.
- [135] H. Suchowski, V. Prabhudesai, D. Oron, A. Arie, and Y. Silberberg. Robust adiabatic sum frequency conversion. *Opt. Express*, 17(15):12731–12740, Jul 2009.
- [136] H. Takesue. Erasing distinguishability using quantum frequency up-conversion. *Phys. Rev. Lett.*, 101:173901, Oct 2008.
- [137] G. Tamošauskas, G. Beresnevičius, D. Gadonas, and A. Dubietis. Transmittance and phase matching of BBO crystal in the 3–5  $\mu\text{m}$  range and its application for the characterization of mid-infrared laser pulses. *Opt. Mater. Express*, 8(6):1410–1418, Jun 2018.
- [138] R. Trebino. *Frequency-Resolved Optical Gating: The Measurement of Ultrashort Laser Pulses*. Kluwer Academic, New York, 2000.
- [139] R. Trebino, K. W. DeLong, D. N. Fittinghoff, J. N. Sweetser, M. A. Krumbügel, B. A. Richman, and D. J. Kane. Measuring ultrashort laser pulses in the time-frequency domain using frequency-resolved optical gating. *Rev. Sci. Instrum.*, 68(9):3277–3295, 1997.
- [140] N. Umemura, K. Miyata, and K. Kato. New data on the optical properties of  $\text{BiB}_3\text{O}_6$ . *Opt. Mater.*, 30(4):532–534, 2007.
- [141] D. Urmann, C. Lorenz, S. M. Linker, M. Braun, J. Wachtveitl, and C. Bammann. Photochemical properties of the red-shifted channelrhodopsin Chrimson. *Photochem. and Photobiol.*, 93(3):782–795, 2017.
- [142] N. V. Vitanov, T. Halfmann, B. W. Shore, and K. Bergmann. Laser-induced population transfer by adiabatic passage techniques. *Annual Review of Physical Chemistry*, 52(1):763–809, 2001. PMID: 11326080.
- [143] G. Wade. *Guided-Wave Acousto-Optics Interactions, Devices, and Applications*, chapter 2. Bulk-Wave Acousto-Optic Bragg Diffraction. Springer-Verlag Berlin Heidelberg, 1990.

- [144] D. Waldburger, C. G. E. Alfieri, S. M. Link, S. Meinecke, L. C. Jaurigue, K. Lüdge, and U. Keller. Multipulse instabilities of a femtosecond sesam-modelocked vecsel. *Opt. Express*, 26(17):21872–21886, Aug 2018.
- [145] J. H. Weber, B. Kambs, J. Kettler, S. Kern, J. Maisch, H. Vural, M. Jetter, S. L. Portalupi, C. Becher, and P. Michler. Two-photon interference in the telecom C-band after frequency conversion of photons from remote quantum emitters. *Nat. Nanotechnol.*, 14:23–26, Jan 2019.
- [146] M. M. Wefers and K. A. Nelson. Space-time profiles of shaped ultrafast optical waveforms. *IEEE J. Quantum Elect.*, 32(1):161–172, 1996.
- [147] A. Weiner. *Ultrafast Optics*, chapter 8. Manipulation of Ultrashort Pulses. John Wiley & Sons, 2009.
- [148] A. M. Weiner. Femtosecond optical pulse shaping and processing. *Prog. Quant. Electron.*, 19(3):161–237, 1995.
- [149] A. M. Weiner. Femtosecond pulse shaping using spatial light modulators. *Rev. Sci. Instrum.*, 71(5):1929–1960, 2000.
- [150] Z. Wu, H. Jiang, L. Luo, H. Guo, H. Yang, and Q. Gong. Multiple foci and a long filament observed with focused femtosecond pulse propagation in fused silica. *Opt. Lett.*, 27(6):448–450, Mar 2002.
- [151] H. Yu, C. Yuan, R. Zhang, Z. Zhang, H. Li, Y. Wang, G. Deng, L. You, H. Song, Z. Wang, G.-C. Guo, and Q. Zhou. Spectrally multiplexed heralded single photon source at telecom-band, 2021.
- [152] S. Zaske, A. Lenhard, C. A. Keßler, J. Kettler, C. Hepp, C. Arend, R. Albrecht, W.-M. Schulz, M. Jetter, P. Michler, and C. Becher. Visible-to-telecom quantum frequency conversion of light from a single quantum emitter. *Phys. Rev. Lett.*, 109:147404, Oct 2012.
- [153] D. E. Zelmon, D. L. Small, and D. Jundt. Infrared corrected Sellmeier coefficients for congruently grown lithium niobate and 5 mol. % magnesium oxide-doped niobate. *J. Opt. Soc. Am. B*, 14(12):3319–3322, Dec 1997.
- [154] C. Zener and R. H. Fowler. Non-adiabatic crossing of energy levels. *Proceedings of the Royal Society of London. Series A, Containing Papers of a Mathematical and Physical Character*, 137(833):696–702, 1932.

- [155] M. N. Zervas and C. A. Codemard. High power fiber lasers: A review. *IEEE Journal of Selected Topics in Quantum Electronics*, 20(5):219–241, 2014.
- [156] A. H. Zewail. Femtochemistry: Atomic-scale dynamics of the chemical bond. *J. Phys. Chem. A*, 104(24):5660–5694, 2000.
- [157] J. Zheng and H. Zacharia. Non-collinear optical parametric chirped-pulse amplifier for few-cycle pulses. *Appl. Phys. B*, 97(4):765, Oct 2009.
- [158] K. Zielnicki, K. Garay-Palmett, D. Cruz-Delgado, H. Cruz-Ramirez, M. F. O’Boyle, B. Fang, V. O. Lorenz, A. B. U’Ren, and P. G. Kwiat. Joint spectral characterization of photon-pair sources. *J. of Mod. Optic.*, 65(10):1141–1160, 2018.